

DEPARTAMENTO DE ASTROFÍSICA

Universidad de La Laguna

*Kinematics, morphology and star formation in
evolving galaxies*

Memoria que presenta
D. Artemi Camps Fariña
para optar al grado de
Doctor por la Universidad de La Laguna.

Dirigida por:
Dr. John E. Beckman
Dr. Joan Font Serra



INSTITUTO DE ASTROFÍSICA DE CANARIAS
junio de 2017

Este documento incorpora firma electrónica, y es copia auténtica de un documento electrónico archivado por la ULL según la Ley 39/2015.
Su autenticidad puede ser contrastada en la siguiente dirección <https://sede.ull.es/validacion/>

Identificador del documento: 973636

Código de verificación: QpwS3TwF

Fecha: 30/06/2017 14:40:15

Firmado por: ARTEMI CAMPS FARIÑA
UNIVERSIDAD DE LA LAGUNA

30/06/2017 15:07:38

JOHN E. BECKMAN
UNIVERSIDAD DE LA LAGUNA

JOAN FONT SERRA
UNIVERSIDAD DE LA LAGUNA

30/06/2017 15:10:02

ERNESTO PEREDA DE PABLO
UNIVERSIDAD DE LA LAGUNA

06/07/2017 13:51:28

Examination date: April, 2017
Thesis supervisors:
Dr. John E. Beckman
Dr. Joan Font Serra
© Artemi Camps Fariña 2017

Este documento incorpora firma electrónica, y es copia auténtica de un documento electrónico archivado por la ULL según la Ley 39/2015.
Su autenticidad puede ser contrastada en la siguiente dirección <https://sede.ull.es/validacion/>

Identificador del documento: 973636	Código de verificación: QpwS3TwF
Firmado por: ARTEMI CAMPS FARIÑA UNIVERSIDAD DE LA LAGUNA	Fecha: 30/06/2017 14:40:15
JOHN E. BECKMAN UNIVERSIDAD DE LA LAGUNA	30/06/2017 15:07:38
JOAN FONT SERRA UNIVERSIDAD DE LA LAGUNA	30/06/2017 15:10:02
ERNESTO PEREDA DE PABLO UNIVERSIDAD DE LA LAGUNA	06/07/2017 13:51:28

*At twilight's end,
the shadow's crossed,
a new world birthed,
the elder lost.*

*Yet on the morn
we wake to find
that mem'ry left
so far behind.*

*To deafened ears
we ask, unseen,
Which is life,
and which the dream?*

Aaron Diaz, Dresden Codak

Este documento incorpora firma electrónica, y es copia auténtica de un documento electrónico archivado por la ULL según la Ley 39/2015.
Su autenticidad puede ser contrastada en la siguiente dirección <https://sede.ull.es/validacion/>

Identificador del documento: 973636

Código de verificación: QpwS3TwF

Firmado por: ARTEMI CAMPS FARIÑA
UNIVERSIDAD DE LA LAGUNA

Fecha: 30/06/2017 14:40:15

JOHN E. BECKMAN
UNIVERSIDAD DE LA LAGUNA

30/06/2017 15:07:38

JOAN FONT SERRA
UNIVERSIDAD DE LA LAGUNA

30/06/2017 15:10:02

ERNESTO PEREDA DE PABLO
UNIVERSIDAD DE LA LAGUNA

06/07/2017 13:51:28

Este documento incorpora firma electrónica, y es copia auténtica de un documento electrónico archivado por la ULL según la Ley 39/2015.
Su autenticidad puede ser contrastada en la siguiente dirección <https://sede.ull.es/validacion/>

Identificador del documento: 973636

Código de verificación: QpwS3TwF

Firmado por: ARTEMI CAMPS FARIÑA
UNIVERSIDAD DE LA LAGUNA

Fecha: 30/06/2017 14:40:15

JOHN E. BECKMAN
UNIVERSIDAD DE LA LAGUNA

30/06/2017 15:07:38

JOAN FONT SERRA
UNIVERSIDAD DE LA LAGUNA

30/06/2017 15:10:02

ERNESTO PEREDA DE PABLO
UNIVERSIDAD DE LA LAGUNA

06/07/2017 13:51:28

Acknowledgements

There is a saying in the English language that states that 'It takes a village to raise a child'. Clearly whoever said it first had never tried to obtain a Ph.D. because a child can turn out better or worse even if it is raised by only one person, but this thesis definitely would not exist without the help and support of an enormous number of people.

First and foremost I need to thank my supervisors John and Joan, whose wisdom, guidance and patience were essential for me to develop as a scientist. I especially want to thank them for the open mind and acceptance they showed whenever I came to their offices with a strange idea to look into even if it delayed more orthodox work, which allowed me freedom to explore whatever concerns I had with my research.

Another big mention goes to my Ph.D. brothers, Javi and Alex, without whom this process would have been much more unbearable. Thank you for all the support and help you provided, which was essential to complete this thesis. I will always remember our sleepless yet rainy nights in the WHT control room, just watching the seeing monitor (or weird videos) and performing "Bricomanía" on GH α FaS to improve the signal (This one is for you too, Joan!).

Other than these there I am thankful to everyone at the IAC, which showed me a perfect environment for research where whenever I have some doubt about anything I can just look up who knows about it and knock on their door to ask about it. There are too many people to mention, but all of you made IAC feel like an "Astrophysics home".

On a more personal level I also want to thank my friends here for all the fun and crazy conversations and in general for their great support, especially to Riccardo, Masca, Irene, Benny, Fede, Isa, Sebas, Rosa, Pablo, Claudio, Edo, Dani, Ernest, Marcos, Lucía, Klaus, Jorge, Paulo, Víctor, Mireia, Marja, Bartek, María, Andrés, Sara, Ana is, Flavia, Sara, Clara, Patri, Morate, Aguado, Alejandro, Martín, Sandra, Sergio, Felipe, Cristina, David, Nacho, Parda, Marina, Rui, Ferra, Lumbreiras (Presidente!), Alex, Mike, Paco, Fred, Pedro, Alfred, Stefano, Melania, Marina, Laura, Andrea, Begoña, Carina, Nacho, Gonzalo, Inés Massimiliano, Patrizia, Simone, Rebeca, Denis, Paul, Isma, Alejandra, Efsan, Rafa, Javi, Pedro, Jorge, Nikolay, Lee, Manolo, Félix, Rael, Pablo, Kilian, Ana and many more that I am probably missing right now, please don't be offended, it is difficult not to miss someone for these 5 years!

Also a big hug all my chilango friends at the ICN in México, who made me feel like I was at home when I worked with them and who I have no doubt will do so again in a few months.

To my aikidoka friends: *Domo arigatou de gozaimasu!*, your friendship is the

Este documento incorpora firma electrónica, y es copia auténtica de un documento electrónico archivado por la ULL según la Ley 39/2015.
Su autenticidad puede ser contrastada en la siguiente dirección <https://sede.ull.es/validacion/>

Identificador del documento: 973636 Código de verificación: QpwS3TwF

Firmado por: ARTEMI CAMPS FARIÑA UNIVERSIDAD DE LA LAGUNA	Fecha: 30/06/2017 14:40:15
JOHN E. BECKMAN UNIVERSIDAD DE LA LAGUNA	30/06/2017 15:07:38
JOAN FONT SERRA UNIVERSIDAD DE LA LAGUNA	30/06/2017 15:10:02
ERNESTO PEREDA DE PABLO UNIVERSIDAD DE LA LAGUNA	06/07/2017 13:51:28

best thing I take with me from the dojo (yeah, even better than the hakama ;)). Thanks for all the fun times to my senseis Carmen, Ricardo and Antonio and all my senpais and kouhais and friends: Samia, Guille, Josu, Elena, Bel, Lui-san, Don Fer, Carlos, Aye, Javi, Raúl, Míriam, David, Edi, Enrique, Grace, Sarai, Sofía, Ángel, Ivan, Jorge, Peñate, Fran, Emilio, Kenji, Janine, Sebas, Sergio, Agus, Dani, Sergio, Juan and many more.

A very special thank you to what is basically my extended family: Adri, Ari, Claudia, Javi, Jur, Maria, Marta, Mireia, Sai. There are no words for everything that you do, you are my strength and support. I will always miss you wherever I go.

Also a big shout-out to the TTT: Jordi, Dul, Genís, Anna, Albert, Lluís, Eve, Ignasi, Joan, Pepe, Laia, Josep, Laura, Bru, Marionna, Valentí, Xander and all the Ramons in the world. Also to Ricard, Òscar, Ruben, Sergio, Francesc, Anna, Ricard, Climent, Dani, Carla, Joan, Omar, Lluís, Albert, Ester, Rosa, Anna, Roc and many many more. You make me feel okay with my craziness and showed me some of the best times I've had.

Lastly, but certainly not least, I want to thank my family, who have helped me in this journey since before I was even born. Their unending and unconditional support and help for all my life have made me who I am today and I owe everything to you (even you, Yaiza ;p).

Per aspera ad astra

Este documento incorpora firma electrónica, y es copia auténtica de un documento electrónico archivado por la ULL según la Ley 39/2015.
Su autenticidad puede ser contrastada en la siguiente dirección <https://sede.ull.es/validacion/>

Identificador del documento: 973636

Código de verificación: QpwS3TwF

Fecha: 30/06/2017 14:40:15

Firmado por: ARTEMI CAMPS FARIÑA
UNIVERSIDAD DE LA LAGUNA

JOHN E. BECKMAN
UNIVERSIDAD DE LA LAGUNA

JOAN FONT SERRA
UNIVERSIDAD DE LA LAGUNA

ERNESTO PEREDA DE PABLO
UNIVERSIDAD DE LA LAGUNA

30/06/2017 15:07:38

30/06/2017 15:10:02

06/07/2017 13:51:28

Resumen

La evolución de las galaxias es un proceso complejo con gran cantidad de factores internos y externos que le influyen de maneras que no se pueden discernir de forma inmediata y que interactúan entre ellos de muchas formas. Uno de los principales causantes de evolución galáctica es la retroalimentación cinética de estrellas masivas o AGN que es capaz de modular la formación estelar, amontándola o reprimiéndola según las circunstancias.

Esta retroalimentación cinética se manifiesta principalmente en forma de burbujas de gas en expansión, que son la consecuencia de los vientos supersónicos o explosiones de supernova barriendo el gas alrededor de la fuente y formando una cáscara en expansión impulsada por el choque. Nuestro objetivo es detectar y caracterizar estas burbujas tal y como se observan en galaxias cercanas, utilizando datos de nuestro instrumento GH α FaS, un espectrómetro Fabry-Pérot (FP) capaz de medir el perfil de la línea de H α con alta resolución espacial (limitada por seeing) ypectral (\sim 6-8 km/s), con un gran campo de visión de 3.4 arcmin x 3.4 arcmin que nos permite analizar la cinemática de galaxias cercanas en gran detalle.

La presencia de expansión en un lugar se puede detectar por la presencia de lo que llamamos la característica de expansión: un par de picos secundarios que se encuentran uno a cada lado del pico principal de la emisión y que tienen una separación en velocidad similar respecto a éste. Hemos desarrollado un método capaz de detectar automáticamente la presencia de componentes múltiples en un perfil de línea espectral que hemos usado para escribir un programa, BUBBLY, que detecta y ajusta todas las componentes de línea espectral sobre toda la galaxia y las ajusta. Después del ajuste BUBBLY detecta la presencia de la característica de expansión y produce un mapa de expansión mostrando la separación en velocidad de las componentes secundarias respecto al pico principal. Con este mapa podemos detectar la presencia de burbujas y obtener sus propiedades.

Hemos aplicado BUBBLY a tres galaxias donde encontramos resultados interesantes en términos de la presencia de burbujas en expansión.

En M33, una galaxia cercana, observamos un campo del brazo sur de la galaxia que contiene varias regiones HII y en una de ellas detectamos tres burbujas distintas aparentemente concéntricas. Utilizamos observaciones adicionales de espectro de rendija de las líneas de emisión H α , [NII] y [SII], lo que nos permitió establecer que las burbujas fueron creadas por explosiones de supernova. Al calcular las masas de las cáscaras encontramos que incluso usando aproximaciones que imponen un límite inferior duro a la masa ésta era demasiado alta considerando que las explosiones ocurrieron en un intervalo corto de

Este documento incorpora firma electrónica, y es copia auténtica de un documento electrónico archivado por la ULL según la Ley 39/2015.
Su autenticidad puede ser contrastada en la siguiente dirección <https://sede.ull.es/validacion/>

Identificador del documento: 973636 Código de verificación: QpwS3TwF

Firmado por: ARTEMI CAMPS FARIÑA UNIVERSIDAD DE LA LAGUNA	Fecha: 30/06/2017 14:40:15
JOHN E. BECKMAN UNIVERSIDAD DE LA LAGUNA	30/06/2017 15:07:38
JOAN FONT SERRA UNIVERSIDAD DE LA LAGUNA	30/06/2017 15:10:02
ERNESTO PEREDA DE PABLO UNIVERSIDAD DE LA LAGUNA	06/07/2017 13:51:28

tiempo y después de la primera apenas debería quedar gas. Propusimos que la existencia de grumos moleculares dentro de la región HII explicaría la masa ausente. Este escenario también explica otra inconsistencia acerca de las bajas energías cinéticas para remanentes de supernova de estas edades.

Las Antenas son un par de galaxias en interacción fuerte que actualmente sufren un gran brote de formación estelar. Aplicamos BUBBLY a un cubo de GH α FaS y detectamos la presencia de 17 superburbujas asociadas a la mayoría de las regiones HII más brillantes del objeto. Encontramos burbujas de gran tamaño, entre 150 - 500 pársecos en radio, con energías entre decenas y centenares de explosiones de supernova. Aparte de las burbujas resueltas también detectamos detecciones extendidas sobre la mayoría del área de la galaxia que asociamos a expansión no resuelta espacialmente de regiones HII más pequeñas por el hecho de que tienen velocidades de expansión similares y con bajos valores en vez de la distribución aleatoria que esperaríamos del ruido. Utilizando varias aproximaciones estimamos la energía cinética contenida en la expansión no resuelta y vimos que esta a la par con la de las regiones HII gigantes con burbujas resueltas.

En último lugar analizamos un cubo Fabry-Pérot de otro par de galaxias en interacción, Arp 70, que obtuvimos de un repositorio público de datos FP. En la galaxia más grande del par encontramos dos tipos diferentes de emanaciones de gas, una en el centro de la galaxia y la otra asociada a una región HII gigante localizada en el brazo. La emanación del centro era especialmente prominente, el flujo de las componentes secundarias era parecido al del pico principal. Utilizamos un espectro de fibra de SDSS para determinar que el centro de la galaxia contiene un AGN que es el origen de la emanación. También confirmamos la detección de la emanación en el espectro de SDSS en las líneas de emisión H α y [NII]. Con los datos FP estimamos la forma de la emanación que está compuesta de dos conos de gas en expansión, uno acercándose a nosotros y el otro alejándose, y usamos esta información para determinar sus parámetros físicos, encontrando energías del orden de 10^{57} erg y masas del orden de $10^8 M_{\odot}$. En la región HII gigante encontramos una burbuja en expansión igualmente gigantesca con un diámetro de 5 kpc, la mayor que hayamos encontrado y posiblemente la mayor superburbuja detectada asociada a una región HII. La burbuja tiene una energía del orden de 10^{54} erg y una masa de unos $4 \cdot 10^7 M_{\odot}$. Ambas emanaciones se encuentran bastante cercanas comparadas con sus tamaños, por lo que es posible que el brote de formación estelar de la región HII fuera provocado por el AGN, aunque también es posible que ambas fueran provocadas por la interacción con la otra galaxia del par.

Este documento incorpora firma electrónica, y es copia auténtica de un documento electrónico archivado por la ULL según la Ley 39/2015.
Su autenticidad puede ser contrastada en la siguiente dirección <https://sede.ull.es/validacion/>

Identificador del documento: 973636 Código de verificación: QpwS3TwF

Firmado por: ARTEMI CAMPS FARIÑA UNIVERSIDAD DE LA LAGUNA	Fecha: 30/06/2017 14:40:15
JOHN E. BECKMAN UNIVERSIDAD DE LA LAGUNA	30/06/2017 15:07:38
JOAN FONT SERRA UNIVERSIDAD DE LA LAGUNA	30/06/2017 15:10:02
ERNESTO PEREDA DE PABLO UNIVERSIDAD DE LA LAGUNA	06/07/2017 13:51:28

Summary

Galaxy evolution is a complex process with many internal and external factors that influence it in ways that are not immediate to discern and that can interact with each other in many ways. One of the main drivers of galaxy evolution is kinetic feedback by massive stars or AGN which is capable of modulating the star formation, either enhancing or quenching it depending on the circumstances.

This kinetic feedback manifests mostly in the form of expanding gas bubbles, which are the result of supersonic winds or supernova explosions sweeping the gas surrounding the source into an expanding shell driven by the shock. Our aim is to detect and characterise these bubbles as they appear in nearby galaxies, using data from our instrument GH α FaS, a Fabry-Pérot (FP) spectrometer which is capable of measuring the H α line profile at a high spatial (seeing-limited) and spectral (\sim 6-8 km/s) resolution, with a large field of view of 3.4 arcmin \times 3.4 arcmin which allows us to analyse the kinematics of a nearby galaxy in great detail.

The presence of expansion in an area can be detected from the presence of what we call an expansion signature: a pair of secondary peaks found on each side of the main peak of the emission and with a similar velocity separation from the main peak. We have developed a method capable of detecting automatically the presence of multiple components in a spectral line profile which we used to write a program, BUBBLY, which detects and fits all spectral line components over the entire galaxy and fits them. After the fit BUBBLY detects the presence of the expansion signature and produces an expansion map showing the velocity separation of the secondary components with respect to the main peak. With this map we can detect the presence of bubbles and obtain their properties.

We applied BUBBLY to three galaxies where we found interesting results regarding the presence of expanding bubbles.

In M33, a nearby galaxy, we observed a field on the southern arm containing a few HII regions and on one of these we detected three distinct bubbles, which appeared to be concentric. We used complementary long-slit observations of the H α , [SII] and [NII] emission lines which allowed us to determine that the bubbles were created by supernova explosions. Upon calculating the masses for the swept-up shells we found that, even using approximations which imposed hard lower limits on the mass, it was too high considering that the explosions occurred close in time and after the first explosion there should be very little gas left over. We proposed that surviving molecular clumps inside the HII region would account for the missing mass. This scenario also explained another apparent inconsistency regarding the low kinetic energy that the supernova

Este documento incorpora firma electrónica, y es copia auténtica de un documento electrónico archivado por la ULL según la Ley 39/2015.
Su autenticidad puede ser contrastada en la siguiente dirección <https://sede.ull.es/validacion/>

Identificador del documento: 973636 Código de verificación: QpwS3TwF

Firmado por: ARTEMI CAMPS FARIÑA UNIVERSIDAD DE LA LAGUNA	Fecha: 30/06/2017 14:40:15
JOHN E. BECKMAN UNIVERSIDAD DE LA LAGUNA	30/06/2017 15:07:38
JOAN FONT SERRA UNIVERSIDAD DE LA LAGUNA	30/06/2017 15:10:02
ERNESTO PEREDA DE PABLO UNIVERSIDAD DE LA LAGUNA	06/07/2017 13:51:28

remnants had for their age.

The Antennae galaxies are a strongly interacting pair of galaxies currently undergoing a massive burst of star formation. We applied bubbly to a GH α FaS data cube and detected 17 distinct superbubbles associated with most of the brightest HII regions in the object. We found generally large bubbles of sizes 150 - 500 parsec in radius, with energies between tens and hundreds of supernova explosions. Apart from the distinct superbubbles we also had extended detections over most of the galaxy which we ascribed to unresolved expansion on smaller HII regions due to the fact that they have similar, low, expansion velocities instead of the random values expected if they originated from noise. Using several approximations we estimated the kinetic energy contained within this unresolved expansion and found it to be on par with that of the resolved, giant, HII regions.

Finally, we analysed a Fabry-Pérot cube of the interacting pair of galaxies Arp 70 which was obtained from a public repository of FP data. On the larger galaxy we found two different types of outflows, one in the centre and the other associated with a giant HII region in the arm region. The central outflow was especially prominent, with the flux of the secondary peaks being similar to that of the main peak. We used an archive fibre spectrum from SDSS to determine that the centre of the galaxy housed an AGN which is the origin of the outflow. We also confirmed the detection of the outflow in the SDSS spectrum in H α and [NII]. Using the FP cube we estimated the shape of the outflow which comprises two cones of expanding material, one approaching and the other receding from us, and used this to estimate the physical properties of the outflow, finding energies of order 10^{57} erg and masses of order $10^8 M_\odot$. On the giant HII region we found a similarly gigantic expanding superbubble with a diameter of 5 kpc, the largest we have ever detected and possibly the largest such detected superbubble associated with an HII region. The bubble has an energy of order 10^{54} erg and a mass of about $4 \cdot 10^7 M_\odot$. Both outflows are relatively close compared to their sizes so it is possible that the burst of star formation on the HII region was triggered by the AGN, though it is also possible that both were independently triggered by the interaction with the other galaxy in the pair.

Este documento incorpora firma electrónica, y es copia auténtica de un documento electrónico archivado por la ULL según la Ley 39/2015.
Su autenticidad puede ser contrastada en la siguiente dirección <https://sede.ull.es/validacion/>

Identificador del documento: 973636

Código de verificación: QpwS3TwF

Fecha: 30/06/2017 14:40:15

Firmado por: ARTEMI CAMPS FARIÑA
 UNIVERSIDAD DE LA LAGUNA

JOHN E. BECKMAN
 UNIVERSIDAD DE LA LAGUNA

JOAN FONT SERRA
 UNIVERSIDAD DE LA LAGUNA

ERNESTO PEREDA DE PABLO
 UNIVERSIDAD DE LA LAGUNA

30/06/2017 15:07:38

30/06/2017 15:10:02

06/07/2017 13:51:28

Contents

1	Introduction	1
1.1	Galaxy evolution	1
1.1.1	Regulation of the star formation	2
1.1.2	Cold gas accretion	3
1.1.3	Metal dissemination	4
1.1.4	Galaxy simulations	5
1.1.5	Cusp-core problem	6
1.2	Feedback processes	7
1.2.1	Massive star winds	7
1.2.2	Supernovae	10
1.2.3	AGN	11
1.3	Background in expanding bubbles	13
1.3.1	Observations	14
1.3.2	Hydrodynamic simulations	15
1.4	GH α FaS	16
1.4.1	Data reduction	18
1.5	Outline of this thesis	18
2	Development of the method	21
2.1	Introduction	21
2.1.1	Expansion signature	21
2.1.2	Instrument suitability	22
2.2	Multi-peaked emission analysis	24
2.2.1	The second derivative method	25
2.2.2	Implementation	27
2.2.3	Input parameters	30
2.3	Application to expanding structures	33
2.3.1	Finding the expanding structures	34

2.3.2	Bubble properties	38
2.3.3	Approximations	40
2.4	Discussion	42
3	Improvement on noise determination	45
3.1	Introduction	45
3.2	Validity of the theoretical noise value	47
3.3	Estimation using the reduced data	50
3.3.1	Use total flux of the peak	50
3.3.2	Continuum dispersion	51
3.3.3	Smoothed spectrum subtraction	51
3.3.4	Local smoothed spectrum subtraction	53
3.3.5	Spline fitting	53
3.3.6	Spatial smoothing subtraction	55
3.4	Noise estimation using simulated data and mock observations	55
3.4.1	Mock observation	55
3.4.2	Noise statistics	58
4	Three supernova shells around an M33 star cluster	63
4.1	Introduction	63
4.2	Observations	64
4.3	Expansion maps	64
4.4	Properties of the bubbles	66
4.4.1	Archival properties of the cluster	67
4.4.2	Identification as supernova remnants	70
4.4.3	Physical properties	72
4.5	Discussion	73
5	Superbubbles in the Antennae galaxies	77
5.1	Introduction	77
5.2	Observations	78
5.3	Expansion map	79
5.4	Physical properties of the superbubbles	80
5.4.1	Extended detections	84
5.5	Hydrodynamic simulation	85
5.5.1	Modelling setup	86
5.5.2	Results of the modelling exercise	87
5.6	Degree of shock-induced ionization	91
5.7	Comparison with HST	92
5.8	Summary and conclusions	93

Este documento incorpora firma electrónica, y es copia auténtica de un documento electrónico archivado por la ULL según la Ley 39/2015.
Su autenticidad puede ser contrastada en la siguiente dirección <https://sede.ull.es/validacion/>

Identificador del documento: 973636 Código de verificación: QpwS3TwF

Firmado por: ARTEMI CAMPS FARIÑA UNIVERSIDAD DE LA LAGUNA	Fecha: 30/06/2017 14:40:15
JOHN E. BECKMAN UNIVERSIDAD DE LA LAGUNA	30/06/2017 15:07:38
JOAN FONT SERRA UNIVERSIDAD DE LA LAGUNA	30/06/2017 15:10:02
ERNESTO PEREDA DE PABLO UNIVERSIDAD DE LA LAGUNA	06/07/2017 13:51:28

6	Arp 70: An interacting galaxy with extreme outflows	97
6.1	Introduction	97
6.2	Data	98
6.2.1	Reduction	98
6.3	Results	100
6.3.1	Outflow detection	100
6.3.2	Physical properties	107
6.3.3	Superbubble associated with the HII region	110
6.4	Summary and conclusions	114
7	Conclusions	117
7.1	Future work	121
	Bibliography	123

Este documento incorpora firma electrónica, y es copia auténtica de un documento electrónico archivado por la ULL según la Ley 39/2015.
Su autenticidad puede ser contrastada en la siguiente dirección <https://sede.ull.es/validacion/>

Identificador del documento: 973636 Código de verificación: QpwS3TwF

Firmado por: ARTEMI CAMPS FARIÑA UNIVERSIDAD DE LA LAGUNA	Fecha: 30/06/2017 14:40:15
JOHN E. BECKMAN UNIVERSIDAD DE LA LAGUNA	30/06/2017 15:07:38
JOAN FONT SERRA UNIVERSIDAD DE LA LAGUNA	30/06/2017 15:10:02
ERNESTO PEREDA DE PABLO UNIVERSIDAD DE LA LAGUNA	06/07/2017 13:51:28

Este documento incorpora firma electrónica, y es copia auténtica de un documento electrónico archivado por la ULL según la Ley 39/2015.
Su autenticidad puede ser contrastada en la siguiente dirección <https://sede.ull.es/validacion/>

Identificador del documento: 973636

Código de verificación: QpwS3TwF

Firmado por: ARTEMI CAMPS FARIÑA
UNIVERSIDAD DE LA LAGUNA

Fecha: 30/06/2017 14:40:15

JOHN E. BECKMAN
UNIVERSIDAD DE LA LAGUNA

30/06/2017 15:07:38

JOAN FONT SERRA
UNIVERSIDAD DE LA LAGUNA

30/06/2017 15:10:02

ERNESTO PEREDA DE PABLO
UNIVERSIDAD DE LA LAGUNA

06/07/2017 13:51:28

List of Figures

1.1 Diagram of the structure of a wind bubble, R_1 is the reverse shock radius, R_C is the contact discontinuity between the wind and swept-up material, and R_2 is the outer shock. Figure taken from Weaver et al. (1977).	9
1.2 Scheme of the unified model that explains the diversity in AGN emission as a result of observer orientation. (Image credit: NASA/Fermi)	12
1.3 Schematic of a Fabry-Perot interferometer.	17
1.4 The resulting (summed) data cube for a galaxy before (A) and after (B) derotation performed by software. The derotation enlarges the FOV in order to preserve all detected flux. Image taken from Blasco-Herrera (2012).	19
2.1 Schematic representation of how an expanding shell around an HII region produces the expansion signature. As HII regions are typically optically thin, we receive emission from the entire line of sight. The bulk of the HII region produces most of the flux, with the approaching and receding parts of the shell offset from it on account of Doppler redshift caused by the expansion velocity.	23
2.2 Illustration of the projection effect in the detected expansion velocity, colors show velocity, with dark red as the real expansion velocity, highest, and indigo as zero.	24

- 2.3 Graph illustrating the effectiveness of the second derivative method to separate Gaussian components. The points correspond to the zeros of the second derivative. Note that the centre of any Gaussian lies between two zeros of the second derivative, a positive to negative zero and a negative to positive zero. This holds true regardless of the direction in which you sweep the profile to search for these zeros and is used to find and determine the initial parameters for each Gaussian component.

2.4 Example of expansion detection in an HII region of the Antennae (see Fig 2.5). The individual components (green, red and blue) are plotted along with the profile (black) and the fit result (crosses). The brightest, main peak corresponds to the emission from the bulk of the HII region, and the two smaller, symmetrically placed peaks on each side correspond to the approaching and receding parts of the superbubble along the line of sight in that particular spatial point. Further peaks can be observed on the profile, but they are not taken into consideration here as they are not symmetric in velocity about the central peak, which they would be in the case of expansion. They represent a complexity of kinematic structure which is clearly present, but which we are, for the present, not pursuing in detail.

2.5 Comparison between the $\text{H}\alpha$ narrow band image (left) of the Antennae galaxies and the corresponding expansion map (right). The circles represent the estimated bubble radii and the white line signals the position for the $\text{H}\alpha$ profile shown in Fig. 2.4. The scale is velocity separation (in absolute values) with respect to the main peak produced by the bulk of the HII region, obtained by taking the average separation of the approaching and receding peaks.

2.6 Detail of a superbubble detected in the brightest HII region in the Antennae galaxies. The scale is velocity with respect to the emission from the bulk of the HII region and the white circle represents the estimated superbubble radius. As expected from an expanding structure, we can see the highest velocity at the centre, falling to lower values towards the edge. The spatial coherence and effect of projection on the observed velocity can be well seen in this example.

Este documento incorpora firma electrónica, y es copia auténtica de un documento electrónico archivado por la ULL según la Ley 39/2015.
Su autenticidad puede ser contrastada en la siguiente dirección <https://sede.ull.es/validacion/>

Identificador del documento: 973636

Código de verificación: QpwS3TwF

Fecha: 30/06/2017 14:40:15

Firmado por: ARTEMI CAMPS FARIÑA
UNIVERSIDAD DE LA LAGUNA

JOHN E. BECKMAN
UNIVERSIDAD DE LA LAGUNA

JOAN FONT SERRA
UNIVERSIDAD DE LA LAGUNA

ERNESTO PEREDA DE PABLO
UNIVERSIDAD DE LA LAGUNA

30/06/2017 15:10:02

06/07/2017 13:51:28

2.7 Profile observed in the Antennae galaxies where two pairs of symmetrically spaced secondary peaks are detected, implying the possible presence of two superbubbles in one region. An alternative possibility is that it could be a projection effect with two HII regions overlapping on the line of sight which may indicate more complex kinematics. As in Fig. 2.4 we show separated peaks only for detected components that are symmetrical to the main peak.	38
2.8 Results of two hydrodynamic simulations from Zaninetti (2004) showing the effects of a density gradient associated with a galaxy disc. The figures show the shape and size of consecutive snapshots in the bubble evolution as dotted lines.	41
3.1 Map showing the continuum overestimation performed by COMPUTEVERYTHING for the Antennae galaxies, obtained by measuring the continuum on the processed cube. The fact that the values are negative means that it was indeed overestimated, and it is also apparent that it correlates with the region brightness.	46
3.2 Expansion map resulting from using BUBBLY on the derotated cube before applying the reduction pipeline and imposing S:N \geq 1.	47
3.3 Emission profile for a spaxel in UGC 3995, where the digression from Poisson statistics can be appreciated. The profile shows an emission peak with a maximum value below 1 count and noisy fluctuations of order \sim 0.1 counts.	48
3.4 These two snapshots show the effect of the derotation software on the detections. On the left we show a region of an observed frame with sparse detections, and on the right the same region after the derotation has been performed. The detections on the right are no longer point-like, showing an extended structure.	49
3.5 Expansion maps obtained by two different methods to estimate noise. a) uses Poisson statistics for the entire flux of a peak instead of each element, while b) estimates the noise from the standard deviation of the continuum.	52
3.6 Expansion maps obtained by two different methods to estimate noise based on subtracting a smoothed spectrum from the original. a) obtains a single standard deviation of the remnant, while b) calculates a vector of standard deviations using the adjacent values only.	54

Este documento incorpora firma electrónica, y es copia auténtica de un documento electrónico archivado por la ULL según la Ley 39/2015.
Su autenticidad puede ser contrastada en la siguiente dirección <https://sede.ull.es/validacion/>

Identificador del documento: 973636 Código de verificación: QpwS3TwF

Firmado por: ARTEMI CAMPS FARIÑA UNIVERSIDAD DE LA LAGUNA	Fecha: 30/06/2017 14:40:15
JOHN E. BECKMAN UNIVERSIDAD DE LA LAGUNA	30/06/2017 15:07:38
JOAN FONT SERRA UNIVERSIDAD DE LA LAGUNA	30/06/2017 15:10:02
ERNESTO PEREDA DE PABLO UNIVERSIDAD DE LA LAGUNA	06/07/2017 13:51:28

3.7 Expansion maps obtained by two different methods to estimate noise. a) fits a spline to the spectral profile to obtain the noise, b) performs a spatial smoothing instead and subtracts it from the cube to obtain the noise.	56
3.8 Relative intensity plot for the derotated cube. We show the ratio between the intensity measured in the derotated cube and the model cube with respect to the measured intensity. The coloured lines correspond to the different sigma values, blue for 1σ (68%), green for 2σ (95%) and red for 3σ (99%). The width between the low and high lines defines the associated relative noise for each intensity value.	59
3.9 Relative intensity plot for the fully reduced cube. We show the ratio between the intensity measured in the derotated cube and the model cube with respect to the measured intensity. The coloured lines correspond to the different sigma values, blue for 1σ (68%), green for 2σ (95%) and red for 3σ (99%). The width between the low and high lines defines the associated relative noise for each intensity value.	60
3.10 Relative intensity plot for the derotated cube after applying Gaussian smoothing in the spatial direction. We show the ratio between the intensity measured in the derotated cube and the model cube with respect to the measured intensity. The coloured lines correspond to the different sigma values, blue for 1σ (68%), green for 2σ (95%) and red for 3σ (99%). The width between the low and high lines defines the associated relative noise for each intensity value.	61
4.1 Example of a spaxel from the GH α FaS data cube which shows three pairs of symmetrically placed secondary peaks, indicating expansion. The detection and fitting was performed automatically using BUBBLY.	65
4.2 Expansion maps of the three detected bubbles, which show the detected expansion velocity in each pixel, all in the same velocity scale. Overlaid are contours of the region's H α emission, it can be seen that the bubbles are roughly concentric with each other and the region	66

Este documento incorpora firma electrónica, y es copia auténtica de un documento electrónico archivado por la ULL según la Ley 39/2015.
Su autenticidad puede ser contrastada en la siguiente dirección <https://sede.ull.es/validacion/>

Identificador del documento: 973636

Código de verificación: QpwS3TwF

Fecha: 30/06/2017 14:40:15

Firmado por: ARTEMI CAMPS FARIÑA
 UNIVERSIDAD DE LA LAGUNA

JOHN E. BECKMAN
 UNIVERSIDAD DE LA LAGUNA

JOAN FONT SERRA
 UNIVERSIDAD DE LA LAGUNA

ERNESTO PEREDA DE PABLO
 UNIVERSIDAD DE LA LAGUNA

30/06/2017 15:07:38

30/06/2017 15:10:02

06/07/2017 13:51:28

- 4.3 Comparison between the two methods for determining the electron density. The black line represents the Osterbrock (1989) line ratio diagnostic to obtain the density from a given $[\text{SII}]_{6716}/[\text{SII}]_{6731}$ ratio. The blue lines are the values of the ratio for our bubbles, with the uncertainty represented as blue-coloured areas. In the same fashion but in red, we show the densities obtained using the $\text{H}\alpha$ flux, with the corresponding errors represented as red-coloured areas. For ease of comparison, we show a zoom-in on the intersection of each bubble individually, with the uncertainties represented as patterns. It is apparent that the values for density and the ratios cross at a point compatible with the line diagnostic for each case.

4.4 Diagnostic diagram used to distinguish between supernova remnants (SNR), HII regions (HII) and planetary nebulae (PNe) based on the relation between the SII to $\text{H}\alpha$ and NII to $\text{H}\alpha$ line ratios. We plot the remnants with their identifier numbers as well as the HII region.

5.1 On the right we show the expansion map for the Antennae galaxies, colour coded in velocity of expansion, that is, the mean separation in velocity of the secondary components. On the left is a map of $\text{H}\alpha$ intensity for comparison. The circles represent the superbubble detections in both maps for ease of comparison, with their radius coinciding with the estimated bubble radius. The superbubbles clearly appear around most of the brightest regions. The presence of an extended, widely disseminated low expansion velocity component can also be appreciated (see text for a discussion on its possible origins).

5.2 Result of the simulation at age 4.0 Myr, the figure represents an XZ slice of the density, showing a distorted shape caused by the density gradient in the disc. The bubble is elongated in the Z axis, following the direction of decrease in density. The density in the shell is also not constant, being much higher for the part expanding into the disc. The linear color scale gives the number density in units of cm^{-3}

5.3 Comparison between mock observations of the simulation bubble and the expansion map for this bubble. We show two close time-frames to show the evolution of the bubble appearance in time.

Este documento incorpora firma electrónica, y es copia auténtica de un documento electrónico archivado por la ULL según la Ley 39/2015.
Su autenticidad puede ser contrastada en la siguiente dirección <https://sede.ull.es/validacion/>

Su autenticidad puede ser contrastada en la siguiente dirección <https://sede.ull.es/validacion/>

Identificador del documento: 973636

Código de verificación: QpwS3TwF

Firmado por: ARTEMI CAMPS FARIÑA
UNIVERSIDAD DE LA LAGUNA

Fecha: 30/06/2017 14:40:15

JOHN E. BECKMAN
UNIVERSIDAD DE LA LAGUNA

30/06/2017 15:07:38

JOAN FONT SERRA
UNIVERSIDAD DE LA LAGUNA

30/06/2017 15:10:02

ERNESTO PEREDA DE PABLO
UNIVERSIDAD DE LA LAGUNA

06/07/2017 13:51:28

5.4 Identification diagrams used to distinguish between supernova remnants, HII regions and planetary nebulae. We present measurements of shell (triangles) and main peak (circle) ratios for bubbles 1 and 3, as well as the overlap region. All the shells are clearly placed within the limits of the HII region area, meaning that at this stage they are primarily ionized by radiation, rather than supernova shocks. It is interesting to note, though, that they all fall closer to the supernova remnant area than their corresponding HII region emission.	92
5.5 Comparison between our detections in the expansion map and the high resolution H α images taken by Hubble. The two top panels show clear agreement between the detections, with visible shells matching the expansion map. Panels c-f show other superbubbles with less clear HST detections, although filamentary structures characteristic of winds and supernovae working the ISM can be seen. The two bottom panels show structure missed by BUBBLY, on the left a clear shell seen in HST is not clear enough to warrant detection in the expansion map, while the right panel shows small HII regions which have some high velocity expansion detected at the centres but not enough spatial coverage to be accepted as proper detections.	94
6.1 SDSS spectrum in the 550 - 750 nm (black) with the fitted stellar model overlaid (red).	100
6.2 Spectrum of the central region of Arp 70b from the CIGALE data cube, showing an extreme version of the expansion signature.101	
6.3 Diagram illustrating the effect of jumping an order on the position at which a peak appears on the spectrum of a Fabry-Pérot instrument. The dashed red and blue peaks are the true emission peaks that lie out of our spectral range, while the solid lines are the observed ones. The box indicates the spectral window of our instrument, spanning one <i>Free Spectral Range</i> (FSR). The effect of jumping an order is that the peak appears on the other end of the spectrum, shifted one FSR from its actual position. This property allows us to determine the true position of the peak.102	
6.4 SDSS spectrum for H α , [NII] and [SII], showing the additional components detected for each, we see expanding components detected in H α and [NII] ₆₅₈₄ , as well as an additional component between the peaks of the [SII] doublet.	103

Este documento incorpora firma electrónica, y es copia auténtica de un documento electrónico archivado por la ULL según la Ley 39/2015.
Su autenticidad puede ser contrastada en la siguiente dirección <https://sede.ull.es/validacion/>

Identificador del documento: 973636

Código de verificación: QpwS3TwF

Fecha: 30/06/2017 14:40:15

Firmado por: ARTEMI CAMPS FARÍÑA
 UNIVERSIDAD DE LA LAGUNA

JOHN E. BECKMAN
 UNIVERSIDAD DE LA LAGUNA

JOAN FONT SERRA
 UNIVERSIDAD DE LA LAGUNA

ERNESTO PEREDA DE PABLO
 UNIVERSIDAD DE LA LAGUNA

30/06/2017 15:07:38

30/06/2017 15:10:02

06/07/2017 13:51:28

6.5 SDSS spectrum for the [OIII] and H β lines. We can see that [OIII] is detected, albeit weak, but H β is not. This spectrum has not been continuum model subtracted.	104
6.6 Figure showing the position of our object in a BPT diagram, clearly showing the it corresponds to an AGN. The H β line has not been detected, so on account of [OIII] actually being detected we imposed an lower limit to the [OIII]/H β ratio of 1, which corresponds to zero in the logarithmic scale of the figure.	106
6.7 Figure showing the spatial distribution of the spectral emission from the CIGALE cube by plotting the individual spectra for each point at its spatial position.	108
6.8 Figure showing the estimated cone shapes of the approaching and receding cones. The left cone corresponds to the receding part of the outflow and the right one the approaching part. This identification might seem at odds with Figure 6.7, where the outflow peaks suggest the opposite distribution of approaching and receding outflows, but they are actually switched as a result of the FSR jump described in the text.	109
6.9 H α images of Arp 70b, on the left the zero moment of the CIGALE cube, obtained by summing over all the channels. On the right the continuum subtracted version of this image, where the emission comes only from the H α line itself. This image shows an extremely bright HII region next to the centre in one of the arms.	112
6.10 On the left we show the expansion map where we detect the superbubble, with a red circle indicating the estimated size of the bubble and black contours showing the H α band flux. The contours correspond to the image without continuum subtraction so that both the region and the centre of the galaxy can be distinguished. On the right we show a line profile of a pixel with detected expansion in the centre of the bubble, with the detected components in green (main peak), red and blue. In grey crosses we plot the resulting fitted profile.	112

Este documento incorpora firma electrónica, y es copia auténtica de un documento electrónico archivado por la ULL según la Ley 39/2015.
Su autenticidad puede ser contrastada en la siguiente dirección <https://sede.ull.es/validacion/>

Identificador del documento: 973636

Código de verificación: QpwS3TwF

Fecha: 30/06/2017 14:40:15

Firmado por: ARTEMI CAMPS FARÍÑA
 UNIVERSIDAD DE LA LAGUNA

JOHN E. BECKMAN
 UNIVERSIDAD DE LA LAGUNA

JOAN FONT SERRA
 UNIVERSIDAD DE LA LAGUNA

ERNESTO PEREDA DE PABLO
 UNIVERSIDAD DE LA LAGUNA

30/06/2017 15:07:38

30/06/2017 15:10:02

06/07/2017 13:51:28

Este documento incorpora firma electrónica, y es copia auténtica de un documento electrónico archivado por la ULL según la Ley 39/2015.
Su autenticidad puede ser contrastada en la siguiente dirección <https://sede.ull.es/validacion/>

Identificador del documento: 973636

Código de verificación: QpwS3TwF

Firmado por: ARTEMI CAMPS FARIÑA
UNIVERSIDAD DE LA LAGUNA

Fecha: 30/06/2017 14:40:15

JOHN E. BECKMAN
UNIVERSIDAD DE LA LAGUNA

30/06/2017 15:07:38

JOAN FONT SERRA
UNIVERSIDAD DE LA LAGUNA

30/06/2017 15:10:02

ERNESTO PEREDA DE PABLO
UNIVERSIDAD DE LA LAGUNA

06/07/2017 13:51:28

List of Tables

4.1	Physical properties of the bubbles	69
5.1	Table with the physical parameters of the superbubbles detected in the Antennae galaxies.	82
5.2	Results of the simulation	90
6.1	Emission lines from the SDSS spectrum	105
6.2	Physical properties of the outflow depending on inclination with respect to the observer.	111
6.3	Physical properties of the superbubble associated with the giant HII region	113

xxiii

Este documento incorpora firma electrónica, y es copia auténtica de un documento electrónico archivado por la ULL según la Ley 39/2015.
Su autenticidad puede ser contrastada en la siguiente dirección <https://sede.ull.es/validacion/>

Identificador del documento: 973636 Código de verificación: QpwS3TwF

Firmado por: ARTEMI CAMPS FARIÑA UNIVERSIDAD DE LA LAGUNA	Fecha: 30/06/2017 14:40:15
JOHN E. BECKMAN UNIVERSIDAD DE LA LAGUNA	30/06/2017 15:07:38
JOAN FONT SERRA UNIVERSIDAD DE LA LAGUNA	30/06/2017 15:10:02
ERNESTO PEREDA DE PABLO UNIVERSIDAD DE LA LAGUNA	06/07/2017 13:51:28

Este documento incorpora firma electrónica, y es copia auténtica de un documento electrónico archivado por la ULL según la Ley 39/2015.
Su autenticidad puede ser contrastada en la siguiente dirección <https://sede.ull.es/validacion/>

Identificador del documento: 973636

Código de verificación: QpwS3TwF

Firmado por: ARTEMI CAMPS FARIÑA
UNIVERSIDAD DE LA LAGUNA

Fecha: 30/06/2017 14:40:15

JOHN E. BECKMAN
UNIVERSIDAD DE LA LAGUNA

30/06/2017 15:07:38

JOAN FONT SERRA
UNIVERSIDAD DE LA LAGUNA

30/06/2017 15:10:02

ERNESTO PEREDA DE PABLO
UNIVERSIDAD DE LA LAGUNA

06/07/2017 13:51:28

1

Introduction

1.1 Galaxy evolution

The current vision of a Universe in which the Milky Way is but one among a large number of galaxies is relatively modern, only confirmed by Hubble in 1926 via observations of Cepheid variables in Andromeda. Prior to this, such objects were called 'nebulae' and thought to be part of the Milky Way. Hubble also used these observations to produce the first classification scheme for galaxies, thus setting the first stone for the field of extragalactic astronomy.

There are currently still many unanswered questions regarding the formation and evolution of galaxies, the current scenario for galaxy formation is hierarchical growth: Smaller structures are formed first and the current galaxies form as a result of mergers between them (White & Rees (1978); Fall & Efstathiou (1980)). However, we still don't know why there is a relation between mass and age, such that the more massive galaxies formed their stars earlier (MacArthur et al. (2004)) or why we only detect 2% of the baryons predicted by the CMB fluctuations, the so called 'missing baryons' problem (Persic & Salucci (1992); Fukugita et al. (1998)). Numerical simulations are also unable to properly reproduce the loss of angular momentum necessary to obtain realistic disc sizes (Navarro & Benz (1991)) or reproduce the number of observed satellite galaxies (Moore et al. (1999); Klypin et al. (1999)). These are some of the current problems in the field, but one of the most important is regarding the role of feedback in shaping the properties of the galaxy. Feedback processes are thought to have a great impact in the formation phase (e.g Dekel & Silk (1986)), controlling the star formation efficiency and enriching the IGM, via stellar and AGN feedback. Feedback also continues to be important

throughout the lifetime of the galaxy, here we present some of the most relevant processes in galaxy evolution in which feedback plays an essential role.

1.1.1 Regulation of the star formation

The energy and momentum injected by massive stars into the ISM influences its properties and shape, but one of the most important effects it can have is destabilizing surrounding cold molecular clouds, thus causing their collapse and triggering another burst of star formation (Elmegreen & Lada (1977)). This star formation burst will in turn produce massive stars which can trigger further clouds. In this manner star formation can be self-propagating through the disc via stellar feedback (McCray & Kafatos (1987); Palous et al. (1994)). This mechanism was proposed by Mueller & Arnett (1976) and expanded and formalised by Gerola & Seiden (1978) as the origin of spiral arms in late type galaxies, as Self Propagating Star Formation (SPSF) and Stochastic Self Propagating Star Formation (SSPSF) respectively. In this manner, the propagating star formation within a disc with differential rotation would produce the observed spiral arms, and since the loci of star formation are not fixed the winding problem can be avoided. This ran counter to the density wave theory (Lin & Shu (1964)) which considered the arms to be resonances of the rotation producing stationary density waves.

On a local level, stellar feedback also has importance in regulating the star formation within the stellar association and parent cloud (Tenorio-Tagle et al. (2006)). The efficiency of star formation in molecular clouds is estimated to be $\leq 10\%$ (Franco et al. (1994)), meaning that most of the cloud is not transformed into stars. This happens as a result of the winds and radiation of massive stars formed within the cloud disrupting it. Supernovae are less relevant owing to the delay in time, during which the other two processes are continuously doing work on the cloud.

This generally stops further star formation, though in large associations it is possible to detect young protostars embedded in older HII regions (Hester et al. (1996); Snider et al. (2009); Bik et al. (2010); Choudhury et al. (2010)), which suggests that surviving clouds have been triggered into collapse by feedback from massive stars, such as a recent supernova explosion.

In this manner, massive stellar feedback can trigger and propagate, but also quench star formation in galaxies.

Este documento incorpora firma electrónica, y es copia auténtica de un documento electrónico archivado por la ULL según la Ley 39/2015.
Su autenticidad puede ser contrastada en la siguiente dirección <https://sede.ull.es/validacion/>

Identificador del documento: 973636

Código de verificación: QpwS3TwF

Fecha: 30/06/2017 14:40:15

Firmado por: ARTEMI CAMPS FARIÑA
UNIVERSIDAD DE LA LAGUNA

JOHN E. BECKMAN
UNIVERSIDAD DE LA LAGUNA

JOAN FONT SERRA
UNIVERSIDAD DE LA LAGUNA

ERNESTO PEREDA DE PABLO
UNIVERSIDAD DE LA LAGUNA

30/06/2017 15:07:38

30/06/2017 15:10:02

06/07/2017 13:51:28

1.1.2 Cold gas accretion

In order for star formation to occur the presence of cold gas is required. It is found almost exclusively in disc galaxies, which are also the ones with ongoing star formation. However, the quantities of gas present in galaxies fail to account for sustained star formation throughout the galaxies' lifetime. Analysis of the stellar population in the solar neighbourhood has shown that star formation rate has been near constant in time (Twarog (1980); Binney et al. (2000); Casuso & Beckman (2001)). Analysis of local galaxies shows that the measured SFR would deplete the available gas on quite short timescales of a few Gigayears, requiring that either they are in a rapid depletion epoch or there is a replenishing mechanism (Kennicutt (1983); Sancisi et al. (2008)). The former assumption is ruled out by observations of damped Lyman alpha systems, which show that the quantities of neutral gas stay mostly constant even up to high z (Storrie-Lombardi et al. (1996); Zwaan et al. (2005); Lah et al. (2007); Jorgenson et al. (2009)).

The accretion of extragalactic pristine gas would also explain the discrepancy between closed-box metallicity evolution models and metallicity observations of the solar neighbourhood (Tinsley (1981); Chiappini et al. (2001); Matteucci (2003); Casuso & Beckman (2004)). See next subsection for more details.

Feedback from supernova explosions has been proposed as the origin for a mechanism that extracts gas from the medium surrounding the galaxy. Cosmology has long since predicted that galaxies should be surrounded by a hot, virialized corona of gas (White & Rees (1978); Fukugita & Peebles (2006)). Standard cooling of this corona has been previously proposed as the origin of the cold gas accretion, but calculations and hydrodynamical simulations show that it is too stable for spontaneous infall to account for it (Binney et al. (2009); Joung et al. (2012)), and also if the corona naturally cooled on its own then early-type galaxies should also show presence of cold accreted gas.

Frernali & Binney (2008) proposes that the effect of gas plumes launched into the corona by supernova explosions can cool the coronal gas and trigger the infall. This would make star formation in galaxies self-sustained in the sense that it procures the gas needed to continue as an effect of its presence.

The mechanism consists of accelerated cooling via the local increase in metallicity from the supernova remnant and the ablation effect of the coronal gas as the cloud travels through it. The mixing of the cold gas from the cloud and the corona decreases the latter's cooling time to values shorter than the cloud's flight time (Marinacci et al. (2010)). In Marasco et al. (2012) they compared the kinematics of HI clouds in the Milky Way (Kalberla et al. (2005))

Este documento incorpora firma electrónica, y es copia auténtica de un documento electrónico archivado por la ULL según la Ley 39/2015.
Su autenticidad puede ser contrastada en la siguiente dirección <https://sede.ull.es/validacion/>

Identificador del documento: 973636 Código de verificación: QpwS3TwF

Firmado por: ARTEMI CAMPS FARIÑA UNIVERSIDAD DE LA LAGUNA	Fecha: 30/06/2017 14:40:15
JOHN E. BECKMAN UNIVERSIDAD DE LA LAGUNA	30/06/2017 15:07:38
JOAN FONT SERRA UNIVERSIDAD DE LA LAGUNA	30/06/2017 15:10:02
ERNESTO PEREDA DE PABLO UNIVERSIDAD DE LA LAGUNA	06/07/2017 13:51:28

with their model. The interaction of clouds with the corona that is described in the model produces a modification of their trajectories, which fits well with the HI data.

1.1.3 Metal dissemination

The primordial nucleosynthesis that produced the first atoms was only capable of generating light elements, the vast majority of which was hydrogen, with some helium and a very small fraction of lithium. All other elements, known in an astrophysical context as "metals", have originated in stellar nucleosynthesis. Elements heavier than iron can form only in massive stars during the core-collapse of a supernova explosion. Merging neutron stars are also capable of forming heavy elements, though core-collapse is generally considered the dominant process.

The enrichment of the ISM by these metals is of critical importance to understanding the properties of stars and galaxies, so there have been many efforts to understand how they enrich the primordial gas.

Traditionally, the study of the chemical evolution of galaxies has adopted two main approximations: the instantaneous mixing approximation (IMA) and the instantaneous recycling approximation (IRA) (Talbot & Arnett (1971)). The former assumes that at any point the gas is well-mixed, thus considering the mixing time-scales negligible, while the latter assumes that stars more massive than $1 M_{\odot}$ explode as soon as they are born while those below $1 M_{\odot}$ do not die at all. This comprises the *simple model*, seminal references are Schmidt (1963); Searle & Sargent (1972); Tinsley (1974); Pagel & Patchett (1975) (see Audouze & Tinsley (1976) for a comprehensive review).

The simple model has been quite successful at predicting the general distribution of metallicities in the solar neighbourhood, but in recent years there have been efforts to relax the two approximations in order to fit the observations better.

These approximations do not take into account the effects of galactic winds originated by massive stars on the dissemination of the metals. Spitoni et al. (2009) studied the effect on the delay of the dissemination caused by the up-wards transport of the metals by the winds, which fall onto the disc at a later time. They find that this delay has little effect on the distribution of α -elements but delays the distribution of SNe-originated elements.

Another question is whether the galaxies can be considered closed box systems in regards to their evolution, meaning that there is no exchange of material with outside sources. This approximation is generally relaxed to include some form of pristine gas accretion into the disc, a phenomenon which may well

Este documento incorpora firma electrónica, y es copia auténtica de un documento electrónico archivado por la ULL según la Ley 39/2015.
Su autenticidad puede ser contrastada en la siguiente dirección <https://sede.ull.es/validacion/>

Identificador del documento: 973636 Código de verificación: QpwS3TwF

Firmado por: ARTEMI CAMPS FARIÑA UNIVERSIDAD DE LA LAGUNA	Fecha: 30/06/2017 14:40:15
JOHN E. BECKMAN UNIVERSIDAD DE LA LAGUNA	30/06/2017 15:07:38
JOAN FONT SERRA UNIVERSIDAD DE LA LAGUNA	30/06/2017 15:10:02
ERNESTO PEREDA DE PABLO UNIVERSIDAD DE LA LAGUNA	06/07/2017 13:51:28

be caused by outflows from the galaxy into the halo (see previous section). Galactic winds can also remove metals from the galaxy altogether, enriching the intergalactic medium (IGM) instead. This process is much more prominent in dwarf galaxies owing to their lower gravitational potential which makes the breakout of the gas easier, preventing the ejected metals from falling back into the disc (Heckman et al. (2000); Ferrara & Tolstoy (2000); Kirby et al. (2011); Yin et al. (2011)). In Tremonti et al. (2004) they use data from ~ 53.000 galaxies from SDSS to derive their mass-metallicity relation and find that the effective yield of metals requires that this mechanism is effective in higher galaxy masses than previously thought and very relevant to the chemical evolution of these objects. A later study by Torres-Papaqui et al. (2012) reproduces these effects and suggests that the efficiency of starburst-driven winds does not actually decrease with galaxy mass as would be expected.

1.1.4 Galaxy simulations

Galaxy formation and evolution models have made great progress in recent years, which has spurred the need for their verification. Numerical simulations have become an important tool for analysing the predictions and consequences of each model, as well as to compare the results with observed galaxies.

This is currently a field of rapid developments as the computing power of supercomputers increases and more detailed mechanics can be included in the simulated model. The processes that regulate the formation and evolution of galaxies occur on very different spatial scales, meaning that we need to evaluate the model on both large and small scale simultaneously. This introduces a strict requirement for spatial resolution, which is the main limiting factor in cosmological simulations. For 3D simulations, the number of elements increases cubically, so a 2 times improvement in resolution requires 8 times the number of individual elements and, therefore, computing time.

There are two main methods to develop numerical simulations, Smoothed-Particle Hydrodynamics (SPH) follows discrete particles representing the mass distribution of the galaxy, effectively becoming an N-body problem, using Lagrangian equations for fluids (Lucy (1977); Gingold & Monaghan (1977)). On the other hand we have Adaptive Mesh Refinement (AMR), where instead of following the particles the volume is divided into static cells (Berger & Colella (1989)). This grid has different levels of refinement depending on the distribution of matter. In this manner, denser regions and those that have an uneven distribution require higher resolution, while smooth, sparse regions can be modelled with lower resolutions. The refinement of the grid is determined at each step to follow the evolution of the system.

Este documento incorpora firma electrónica, y es copia auténtica de un documento electrónico archivado por la ULL según la Ley 39/2015.
Su autenticidad puede ser contrastada en la siguiente dirección <https://sede.ull.es/validacion/>

Identificador del documento: 973636

Código de verificación: QpwS3TwF

Fecha: 30/06/2017 14:40:15

Firmado por: ARTEMI CAMPS FARIÑA
 UNIVERSIDAD DE LA LAGUNA

JOHN E. BECKMAN
 UNIVERSIDAD DE LA LAGUNA

JOAN FONT SERRA
 UNIVERSIDAD DE LA LAGUNA

ERNESTO PEREDA DE PABLO
 UNIVERSIDAD DE LA LAGUNA

30/06/2017 15:07:38

30/06/2017 15:10:02

06/07/2017 13:51:28

Even with these tools, the current standards in resolution for cosmological simulations are unable to follow correctly the effect of massive star feedback, which on galactic scales is due mostly to supernova explosions. The greatest problem in simulating the effect of supernovae is that radiative cooling is overestimated, resulting in the immediate dissipation of the energy with little effect on the dynamics of the surrounding ISM (Katz (1992)).

This problem has been patched in a number of ways with ad-hoc assumptions. One of them is to directly transform part of the energy of the supernova and winds into kinetic energy of the ISM (Navarro & White (1993); Mihos & Hernquist (1994)), thus preventing its dissipation via radiative cooling. The fraction of energy that is imparted as radially outgoing momentum is dependent on the parameters of the simulation.

Another approach is to simply suppress the radiative cooling of the particles that are receiving the feedback energy, effectively preventing its immediate dissipation (Gerritsen & Icke (1997); Thacker & Couchman (2000)). The particles are considered adiabatic for about 30 Myr; this approximation is justified by the assumption that individual supernova remnants will combine into a larger hot bubble which will prolong the adiabatic phase.

Lastly, another method is to introduce a subgrid model which stores the information on the hot, unresolved multiphase medium (Yepes et al. (1997); Springel & Hernquist (2003)), which then interacts with the simulation. This model has the advantage that it does not introduce artificial physics to prevent overcooling, but the star-forming regions become closed systems, and some further modelling is required to introduce galactic winds.

1.1.5 Cusp-core problem

The Cold Dark Matter model (CDM) has had remarkable success in reproducing the properties of galaxies, mainly in terms of dynamics and kinematics. One of the main discrepancies that remain unsolved is the cusp-core problem, which consists of a discrepancy in the dark matter distribution in the centres of the galaxies. The rotation curves derived from observations reveal that the dark matter density profile towards the centre is nearly constant, thus forming a 'core'. Cosmological simulations based on the CDM scenario, however, result in a dark matter density profile with a steep power-law distribution, forming a 'cusp'-like shape (Dubinski & Carlberg (1991); Navarro et al. (1996b)).

One of the proposed solutions to this problem is that feedback from supernova explosions can 'smooth' the dark matter distribution in the centre of the galaxy. Navarro et al. (1996a) showed, using N-body simulations, that a strong outflow of baryons, forming a galactic superwind, is capable of flattening the

Este documento incorpora firma electrónica, y es copia auténtica de un documento electrónico archivado por la ULL según la Ley 39/2015.
Su autenticidad puede ser contrastada en la siguiente dirección <https://sede.ull.es/validacion/>

Identificador del documento: 973636 Código de verificación: QpwS3TwF

Firmado por: ARTEMI CAMPS FARIÑA UNIVERSIDAD DE LA LAGUNA	Fecha: 30/06/2017 14:40:15
JOHN E. BECKMAN UNIVERSIDAD DE LA LAGUNA	30/06/2017 15:07:38
JOAN FONT SERRA UNIVERSIDAD DE LA LAGUNA	30/06/2017 15:10:02
ERNESTO PEREDA DE PABLO UNIVERSIDAD DE LA LAGUNA	06/07/2017 13:51:28

dark matter profile. The mechanism is evaluated for dwarf galaxies, as more massive galaxies have potential wells that are too deep to effectively remove the gas. The strength of the outflow also poses an obstacle for this mechanism, as it requires a very violent star-forming episode capable of removing a large fraction of the baryonic mass of the galaxy and expelling it into the halo. Gnedin & Zhao (2002) performed calculations which show that with plausible cosmological and galaxy parameters the effect of the stellar feedback described by Navarro et al. (1996a) is actually insufficient to transfer the necessary energy to the dark matter particles.

An alternative approach to the idea of stellar feedback affecting the dark matter distribution is shown by Pontzen & Governato (2012), who instead propose that the long-term effect of recurrent star-formation bursts near the centre of the galaxy is capable of flattening the cusp. This removes the necessity of extreme outflows and allows more reasonable parameters.

The effect consists of an energy transfer into the dark matter particles' orbits through oscillations in the gravitational potential, which are taken to originate in successive bursts of star formation that produce expanding bubbles through supernova feedback. The process of gas blowout by feedback is therefore understood as an oscillation of the mass distribution by taking long time-scales relative to the age of an HII region. The changes in the trajectories effectively smooth the density profile, as shown in numerical simulations in their paper.

1.2 Feedback processes

Feedback processes are those that inject energy and momentum into the medium as a result of internal phenomena of the host galaxy, that is, those that originate inside it. External processes are also capable of dramatically affecting the galaxy and occur mostly as a result of interactions with the galaxy's environment. Mergers and fly-bys with other galaxies are the most violent of these processes, but other examples include ram-pressure stripping of gas or strangulation, which affect the star-forming capabilities of galaxies.

In this thesis we study the internal processes that produce expanding structures, which generally occur as a result of intense star formation or an active black hole.

1.2.1 Massive star winds

All stars emit winds, that is, a spherical outflow of particles at high velocity. For most stars this wind is relatively weak and only affects a small region around the

Este documento incorpora firma electrónica, y es copia auténtica de un documento electrónico archivado por la ULL según la Ley 39/2015.
Su autenticidad puede ser contrastada en la siguiente dirección <https://sede.ull.es/validacion/>

Identificador del documento: 973636 Código de verificación: QpwS3TwF

Firmado por: ARTEMI CAMPS FARIÑA UNIVERSIDAD DE LA LAGUNA	Fecha: 30/06/2017 14:40:15
JOHN E. BECKMAN UNIVERSIDAD DE LA LAGUNA	30/06/2017 15:07:38
JOAN FONT SERRA UNIVERSIDAD DE LA LAGUNA	30/06/2017 15:10:02
ERNESTO PEREDA DE PABLO UNIVERSIDAD DE LA LAGUNA	06/07/2017 13:51:28

star. Massive O and B stars, however, display much more prominent winds, both in terms of the mass-loss rate and the kinetic energy of the expelled particles.

These stars are capable of carving large cavities around them by sweeping the surrounding ISM with the stellar wind. They are also very massive and therefore short-lived, so they are preferentially found in young clusters formed in a recent burst of star formation.

The basic model for the evolution of expanding bubbles driven by stellar winds was done by Dyson & de Vries (1972), assuming constant input and a homogeneous medium. The resulting structure consists of an inner zone of freely expanding wind and a shocked wind zone, separated by a reverse shock (see Fig. 1.1). The outer zone is bounded by the expanding shell, which is created by the outer shock and separates the shocked wind zone from the ambient ISM. This model was improved by Castor et al. (1975); Weaver et al. (1977), going into further detail on the interaction with the ISM and the consequences.

The evolution of a wind-swept bubble with time t is given by:

$$R \propto t^{3/5} \quad (1.1)$$

which already allows us to obtain the age of the bubble using the current size and expansion velocity:

$$v = \dot{R} = A \frac{3}{5} t^{-2/5} \Rightarrow t = \frac{3}{5} \frac{R}{v} \quad (1.2)$$

A represents the constant parameters of the relation, from Weaver et al. (1977):

$$R = \left(\frac{250}{308\pi} \right)^{1/5} L_w^{1/5} \rho_0^{-1/5} t^{3/5} \quad (1.3)$$

where L_w is the mechanical luminosity of the stellar wind and ρ_0 is the density of the ambient gas.

The wind of a single star produces a small bubble relative to the spatial scales required to affect the structure of the galaxy, but a massive cluster containing many massive stars can combine the mechanical power they produce to create a cluster wind that has far-reaching effects. In extreme cases, such as the nuclear starbursts of M82 and NGC 253 (Lehnert et al. (1999); Strickland et al. (2002)), the winds can create a galactic outflow removing vast quantities of material from the galaxy. Chevalier & Clegg (1985) developed a model for the galactic superwind of M82 by deriving an equivalent input wind from the estimated energy and momentum that is injected into the ISM by the starburst. Cantó et al. (2000) studied the case for more moderate cases of super

Este documento incorpora firma electrónica, y es copia auténtica de un documento electrónico archivado por la ULL según la Ley 39/2015.
Su autenticidad puede ser contrastada en la siguiente dirección <https://sede.ull.es/validacion/>

Identificador del documento: 973636

Código de verificación: QpwS3TwF

Fecha: 30/06/2017 14:40:15

Firmado por: ARTEMI CAMPS FARIÑA
UNIVERSIDAD DE LA LAGUNA

JOHN E. BECKMAN
UNIVERSIDAD DE LA LAGUNA

JOAN FONT SERRA
UNIVERSIDAD DE LA LAGUNA

ERNESTO PEREDA DE PABLO
UNIVERSIDAD DE LA LAGUNA

30/06/2017 15:07:38

30/06/2017 15:10:02

06/07/2017 13:51:28

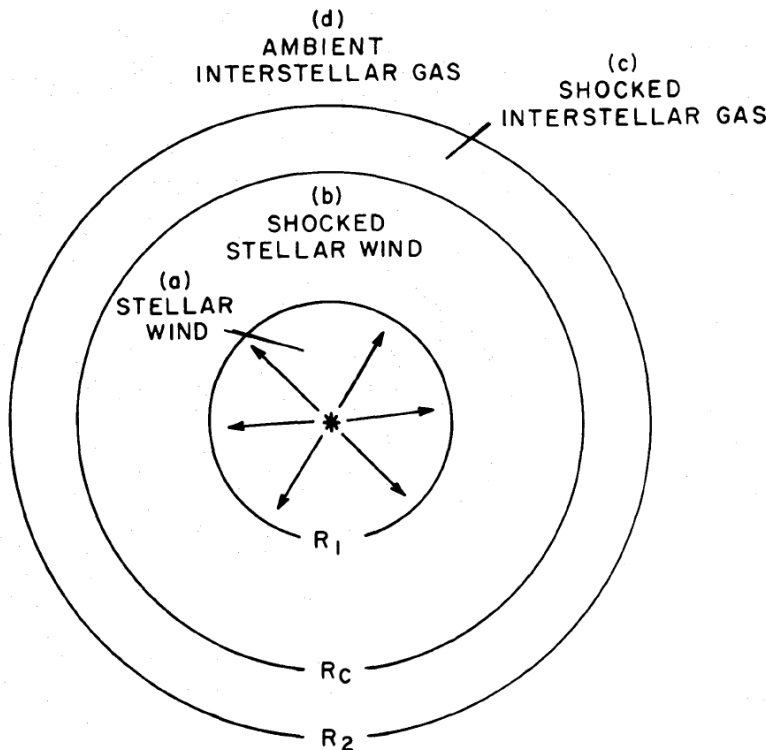


Figure 1.1: Diagram of the structure of a wind bubble, R_1 is the reverse shock radius, R_C is the contact discontinuity between the wind and swept-up material, and R_2 is the outer shock. Figure taken from Weaver et al. (1977).

star clusters (SSC), developing a model to reproduce the properties of an observed cluster with about 100 massive stars. They also perform hydrodynamic simulations of a cluster with 30 stars and compare it with the model, finding very good agreement between the model and the result of the simulations. Stevens & Hartwell (2003) also developed a model for SSC based on the work of Chevalier & Clegg (1985), considering individual stars with wind-blown bubbles that merge to produce the cluster wind, and use it to compare the results from theory and observation on the X-ray properties of such objects.

Este documento incorpora firma electrónica, y es copia auténtica de un documento electrónico archivado por la ULL según la Ley 39/2015.
Su autenticidad puede ser contrastada en la siguiente dirección <https://sede.ull.es/validacion/>

Identificador del documento: 973636

Código de verificación: QpwS3TwF

Firmado por: ARTEMI CAMPS FARIÑA
UNIVERSIDAD DE LA LAGUNA

Fecha: 30/06/2017 14:40:15

JOHN E. BECKMAN
UNIVERSIDAD DE LA LAGUNA

30/06/2017 15:07:38

JOAN FONT SERRA
UNIVERSIDAD DE LA LAGUNA

30/06/2017 15:10:02

ERNESTO PEREDA DE PABLO
UNIVERSIDAD DE LA LAGUNA

06/07/2017 13:51:28

1.2.2 Supernovae

Supernovae represent one of the most violent and energetic processes in the Universe, generally eclipsed only by active black holes. A single supernova is capable of ejecting material from the disc into the galactic halo depending on the circumstances (Chevalier (1974)).

Contrary to the steady input of stellar winds, a supernova explosion consists of a single instantaneous injection of a very large quantity of energy, which then expands as a result of the extremely increased temperature and pressure, which produces an expanding shock. Like the wind-blown bubbles, the accelerated supernova remnant will sweep the ambient gas into an expanding shell.

The kinetic energy injected in a supernova explosion is fairly uniform, at about 10^{51} erg, and the accelerated remnant typically has a mass of about 1-10 solar masses. Consequently, the initial velocity is of the order of 10^3 to 10^4 km/s.

The evolution of a supernova remnant can be divided into three phases: free expansion, adiabatic, and finally radiative or 'snowplough' phase.

The free expansion phase occurs at the beginning, while the initial ejected mass dominates over the swept-up mass. In this phase the ambient medium presents negligible resistance to the expansion of the remnant, and thus the remnant expands as in a vacuum with constant velocity, following:

$$R_{free} \propto t \quad (1.4)$$

This phase ends when the swept-up mass is no longer negligible, which is generally taken to be when the swept-up mass equals that of the initial ejecta. The radius at which the transition occurs is:

$$R_{tr} = \left(\frac{3M_{in}}{4\pi\rho_0} \right)^{1/3} \quad (1.5)$$

After this the remnant expands adiabatically, that is, with negligible energy-loss due to the high velocity of the expanding shock, which means the gas is cooled due only to the expansion. This phase is also called the Sedov-Taylor phase, after the discoverers of the adiabatic self-similar blast-wave solution (Sedov (1959); Taylor (1950)).

In this phase the remnant evolves as:

$$R_{ST} \propto t^{2/5} \quad (1.6)$$

The adiabatic expansion continues until the remnant cools to a critical temperature of 10^6 K behind the shock front. At this point the ionized atoms

Este documento incorpora firma electrónica, y es copia auténtica de un documento electrónico archivado por la ULL según la Ley 39/2015.
Su autenticidad puede ser contrastada en la siguiente dirección <https://sede.ull.es/validacion/>

Identificador del documento: 973636

Código de verificación: QpwS3TwF

Fecha: 30/06/2017 14:40:15

Firmado por: ARTEMI CAMPS FARIÑA
UNIVERSIDAD DE LA LAGUNA

JOHN E. BECKMAN
UNIVERSIDAD DE LA LAGUNA

JOAN FONT SERRA
UNIVERSIDAD DE LA LAGUNA

ERNESTO PEREDA DE PABLO
UNIVERSIDAD DE LA LAGUNA

30/06/2017 15:07:38

30/06/2017 15:10:02

06/07/2017 13:51:28

start to capture free electrons, which allows them to radiate energy via the much more efficient bound-bound and bound-free transitions. The spike in the rate of energy-loss effectively stops the adiabatic evolution, and the remnant transitions from an energy-conserving to a momentum-conserving state.

The third phase is called the radiative or 'snowplough' phase, the former referring to the fact that it cools and slows down due to radiation and the latter because it conserves momentum. This phase was developed theoretically by Cox (1972), and evolves as:

$$R_{rad} \propto t^{2/7} \quad (1.7)$$

As we can see, due to the radiative losses the remnant slows down faster. This is the final phase of the remnant, which will continue to slow down until the expansion velocity is the same as the speed of sound of the ambient gas, at which point the remnant will disperse into the ISM.

1.2.3 AGN

It is widely accepted, albeit not universally, that every massive galaxy hosts a supermassive black hole (SMBH) in its centre, which is key to understanding the properties and evolution of the galaxy (see Kormendy & Ho (2013) for a review). While most of these black holes have entered a quiescent state, there are many examples of galaxies which continue to feed gas to their central SMBH. The acceleration that the gas suffers as it falls into the SMBH produces extreme heating which in turn gives rise to strong radio and X-ray emission, as well as producing narrow jets of collimated matter that is expelled at relativistic velocities.

While AGN appear in galaxies with a variety of properties, these have been brought together in what is called the 'unified model' (Holt et al. (1992); Antonucci (1993); Urry & Padovani (1995)), in which the black hole and its accretion disc are surrounded by a torus of obscuring material. Because of this, the observed properties of the AGN will depend on its orientation relative to the observer. If seen edge-on the torus will obscure most emission, while at some inclination emission from the excited accreting matter will be detected, and if at nearly 90° angle, the relativistic jet will be detected head-on, which is typically known as a blazar. See Fig. 1.2 for a schematic view of the model.

The extreme energies produced by the AGN have a profound impact in the surrounding ISM, and even strongly affect the intergalactic medium (IGM). The highly localized nature of the object limits the effects on the larger scale of the galaxy, but relations between the mass of the SMBH and the bulge have

Este documento incorpora firma electrónica, y es copia auténtica de un documento electrónico archivado por la ULL según la Ley 39/2015.
Su autenticidad puede ser contrastada en la siguiente dirección <https://sede.ull.es/validacion/>

Identificador del documento: 973636 Código de verificación: QpwS3TwF

Firmado por: ARTEMI CAMPS FARIÑA UNIVERSIDAD DE LA LAGUNA	Fecha: 30/06/2017 14:40:15
JOHN E. BECKMAN UNIVERSIDAD DE LA LAGUNA	30/06/2017 15:07:38
JOAN FONT SERRA UNIVERSIDAD DE LA LAGUNA	30/06/2017 15:10:02
ERNESTO PEREDA DE PABLO UNIVERSIDAD DE LA LAGUNA	06/07/2017 13:51:28

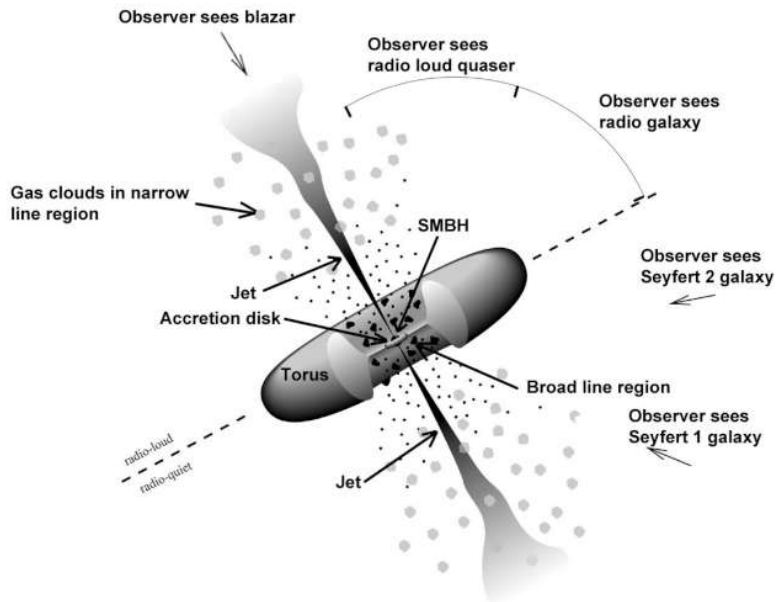


Figure 1.2: Scheme of the unified model that explains the diversity in AGN emission as a result of observer orientation. (Image credit: NASA/Fermi)

been observed which have been linked to feedback from AGN (see Kormendy & Ho (2013)).

The mechanisms associated with this type of feedback consist of AGN-powered winds and outflows, which can be powered by the radiation pressure emitted by the accretion disc or the relativistic jets. See Fabian (2012) for a comprehensive review of the observational evidence of these processes.

AGN feedback is also a strong regulator of star formation in the centre of the galaxy, with an ongoing debate about whether it enhances or quenches star formation. The argument behind enhancement is that the outflow could compress cold clouds triggering a star formation burst, which Silk (2005) proposes as the driver behind ultraluminous starbursts. However, the outflow also removes gas from its surroundings, which would clear out the available fuel for star formation (Hopkins & Elvis (2010); Zubovas & King (2012)). We therefore have two competing mechanisms with opposite effects and it is not currently

Este documento incorpora firma electrónica, y es copia auténtica de un documento electrónico archivado por la ULL según la Ley 39/2015.
Su autenticidad puede ser contrastada en la siguiente dirección <https://sede.ull.es/validacion/>

Identificador del documento: 973636

Código de verificación: QpwS3TwF

Firmado por: ARTEMI CAMPS FARIÑA
UNIVERSIDAD DE LA LAGUNA

Fecha: 30/06/2017 14:40:15

JOHN E. BECKMAN
UNIVERSIDAD DE LA LAGUNA

30/06/2017 15:07:38

JOAN FONT SERRA
UNIVERSIDAD DE LA LAGUNA

30/06/2017 15:10:02

ERNESTO PEREDA DE PABLO
UNIVERSIDAD DE LA LAGUNA

06/07/2017 13:51:28

clear which dominates the effects of AGN feedback. Zubovas & Bourne (2017) perform numerical simulations in an idealised setup to study these effects, finding that in general the AGN will quench star formation while active but after it switches off star formation will be enhanced. These mechanisms depend on the power of the AGN, with a critical value that regulates the behaviour. Above this value the gas starts to be removed too quickly and below it the compression of the clouds becomes inefficient.

1.3 Background in expanding bubbles

Given the importance of detecting the effects of feedback, this topic has been a subject of attention in the field for a long time. The variety of the astrophysical processes which give rise to expanding structures, as well as the complexity that arises from the interplay between the different ISM phases and the shocks has also kept this a relevant astrophysical problem for a long time.

Expanding bubbles are relatively hard to detect, they are diffuse objects that surround a source of energy which is generally much brighter than the shocked gas shell itself. The exception to this is found in X-ray emission; a very hot bubble (typically from a supernova) can be the primary X-ray source in the region. Another staple for shell detection is HI cavities, these are generally older objects where ionizing sources are gone, leaving only a zone of the ISM which has been cleared out of gas.

To detect an expanding bubble we need sufficient spatial and/or spectral resolution to separate its emission from the rest of the source. In terms of spatial resolution we need to resolve the edge of the shell, which shows up as a result of projection effects and is of the scale of the shell width. This requirement effectively limits what can be detected from ground observatories, as even a 10 pc width shell, which typically corresponds to a bubble of radius 100-500 pc can be resolved only up to a distance of 2 Mpc (assuming typical 1" seeing), limiting observations of this type to very large bubbles in local galaxies.

The requirements for spectral resolution are less demanding: to detect the presence of an expanding feature within an emission region we need to resolve the additional components of the emission profile that arise as a consequence of Doppler shift from the different line-of-sight velocity that the expanding shell exhibits.

A spectral resolution of 25 km/s is generally enough to detect typical separations of about 50-150 km/s, though in extreme cases such as large outflows from AGN, which typically are separated \sim 1000 km/s, less resolution would be necessary. The value of 25 km/s translates to a resolving power of $R=12000$, which is high but not prohibitive in terms of ground-based instrumentation.

Este documento incorpora firma electrónica, y es copia auténtica de un documento electrónico archivado por la ULL según la Ley 39/2015.
Su autenticidad puede ser contrastada en la siguiente dirección <https://sede.ull.es/validacion/>

Identificador del documento: 973636 Código de verificación: QpwS3TwF

Firmado por: ARTEMI CAMPS FARIÑA UNIVERSIDAD DE LA LAGUNA	Fecha: 30/06/2017 14:40:15
JOHN E. BECKMAN UNIVERSIDAD DE LA LAGUNA	30/06/2017 15:07:38
JOAN FONT SERRA UNIVERSIDAD DE LA LAGUNA	30/06/2017 15:10:02
ERNESTO PEREDA DE PABLO UNIVERSIDAD DE LA LAGUNA	06/07/2017 13:51:28

Another advantage of detecting with spectral emission is that distance does not affect the diagnostic in the same manner as with spatial resolution.

Imaging and spectral detections have complementary drawbacks, using images to detect the projected shape misses the kinetic information which is essential to obtain the energy of the bubble, while a spectrum cannot be used to obtain the size of the bubble. Because of this, long-slit spectrum observations, which preserve spatial information to some extent are one of the traditionally successful methods to detect these objects.

1.3.1 Observations

Detections of bubbles are ubiquitous on all scales studied by astronomy, starting from the solar neighbourhood, with the so called Local Bubble which encompasses the Sun and some of the nearest stars. It was detected as an underdensity in the area, subsequently finding clouds that are thought to make up a wall of the bubble (e.g. Cox & Reynolds (1987); Genova et al. (1990)).

Nearby examples of expanding bubbles are often supernova remnants or planetary nebulae. The most iconic close supernova remnant is the Crab Nebula, which originates from a supernova explosion seen from Earth in the year 1054 (Lampland (1921); Mayall (1939)). It is one of the most studied objects in the sky and remains a valuable laboratory to probe the evolution of supernova remnants, especially in regards to the central pulsar, which creates its own small bubble within the remnant (Kennel & Coroniti (1984)). Other notable remnants are Tycho, associated with a supernova seen in 1572 (Hanbury Brown & Hazard (1952)) and Kepler, associated with the supernova of 1604 (Baade (1943)). These originate from type Ia supernovae, while the Crab Nebula was created by a type II supernova.

Supernova remnants are produced by massive stars or interacting pairs, so planetary nebula, which are created by lower mass stars, are more common. These are produced at the end of a low or intermediate mass star ($0.8\text{--}8 M_{\odot}$), and consist of the external layers of gas of the star which are expelled when it collapses into a white dwarf at the end of its lifetime. The first planetary nebula to be discovered was the Dumbbell nebula by Charles Messier in 1764. Other notable examples are the Ring Nebula, which owes its name to the almost perfect ring-like shape, or the Cat's Eye Nebula, the first to be observed spectroscopically in 1864 by William Huggins. Also, the Helix Nebula is one of the nearest such objects and the first where dense knots of condensed material were found (Zanstra (1955)).

There are also many detections of expanding bubbles beyond our galaxy, but as an effect of the increased distance these objects tend to be

Este documento incorpora firma electrónica, y es copia auténtica de un documento electrónico archivado por la ULL según la Ley 39/2015.
Su autenticidad puede ser contrastada en la siguiente dirección <https://sede.ull.es/validacion/>

Identificador del documento: 973636 Código de verificación: QpwS3TwF

Firmado por: ARTEMI CAMPS FARIÑA UNIVERSIDAD DE LA LAGUNA	Fecha: 30/06/2017 14:40:15
JOHN E. BECKMAN UNIVERSIDAD DE LA LAGUNA	30/06/2017 15:07:38
JOAN FONT SERRA UNIVERSIDAD DE LA LAGUNA	30/06/2017 15:10:02
ERNESTO PEREDA DE PABLO UNIVERSIDAD DE LA LAGUNA	06/07/2017 13:51:28

larger and more energetic. Radio observations in HI have revealed bubbles in large nearby galaxies such as M31 (Brinks & Bajaja (1986)) and M33 (Deul & den Hartog (1990)), but also in dwarfs such as Holmberg II (Puche et al. (1992)) or IC 10 (Wilcots & Miller (1998)), as well as in the Magellanic clouds (LMC: Kim et al. (1999), SMC: Staveley-Smith et al. (1997)).

Expanding shells have also been detected via the ionized gas with H α observations, which trace younger objects still interacting with the originating cluster. The Magellanic clouds are an ideal target for these observations with many relevant observations such as :Meaburn (1980, 1984); Rosado (1986); Le Coarer et al. (1993); Chu & Kennicutt (1994)), and more recently Ambrocio-Cruz et al. (2016); Reyes-Iturbide et al. (2014) for the LMC. A sample of bubbles and superbubbles was also found in the nearby irregular galaxy IC 1613 (Valdez-Gutiérrez et al. (2001)).

On a larger scale we find galactic winds due to bursts of star formation, M82 being the iconic example of such a nuclear superwind (Bland & Tully (1988)). Another notable example is NGC 3079 (Veilleux et al. (1994)), with a well formed cauldron-shaped shell of expanding material located in the centre.

AGN are also expected to create galactic winds, exhibiting higher expansion velocities than those originated by star formation. Tremonti et al. (2007) managed to detect remnants of galactic outflows at high velocity associated with AGN activity in 4 galaxies out of a sample of 10.

1.3.2 Hydrodynamic simulations

Numerical simulations are one of the most important tools that an astrophysicist has available, they enable us to test the detailed consequences of proposed models, and are relevant on all physical scales, from the structure of stars to the cosmic web.

The expansion of bubbles created by supersonic shocks has been solved analytically, but this considers only the ideal case of a homogeneous medium disturbed by either steady or instantaneous isotropic energy injection. In real cases the structure of the ISM tends to be inhomogeneous, with a large variety in the phases of the gas involved. Within an HII region molecular, atomic, and ionized gas can coexist, as well as varying quantities of dust and metals.

Because of this, the finer details of models relating to stellar feedback need to be validated by numerical simulations. In section 1.1.4 we described the main types of algorithms used in astrophysics, Smoothed Particle Hydrodynamics (SPH) and grid-based methods with Adaptive Mesh Refinement (AMR).

SPH-based codes are especially successful in conservation of energy and momentum, which makes it appropriate to gravity-dominated problems such

Este documento incorpora firma electrónica, y es copia auténtica de un documento electrónico archivado por la ULL según la Ley 39/2015.
Su autenticidad puede ser contrastada en la siguiente dirección <https://sede.ull.es/validacion/>

Identificador del documento: 973636 Código de verificación: QpwS3TwF

Firmado por: ARTEMÍ CAMPS FARIÑA UNIVERSIDAD DE LA LAGUNA	Fecha: 30/06/2017 14:40:15
JOHN E. BECKMAN UNIVERSIDAD DE LA LAGUNA	30/06/2017 15:07:38
JOAN FONT SERRA UNIVERSIDAD DE LA LAGUNA	30/06/2017 15:10:02
ERNESTO PEREDA DE PABLO UNIVERSIDAD DE LA LAGUNA	06/07/2017 13:51:28

as cosmological simulations. When it comes to fluid discontinuities, however, grid-based methods tend to perform better than SPH which, coupled with the fact that gravity is generally not dominant in these simulations, makes grid-based methods better for simulating bubbles. Tasker et al. (2008) performed tests on popular codes of both types to see how well they resolve a number of template hydrodynamic problems. They find that AMR refinement allows for a better reproduction of processes with regions of rapidly changing density, while SPH performs better at problems with large density contrasts between different areas and large volumes of empty space.

Because of this, AMR algorithms are especially suited to simulating expanding shells. One of the first examples can be found in Mac Low et al. (1989), where they use ZEUS, a 2D Eulerian code without grid refinement (Norman & Winkler (1986)), to study the blowout of a superbubble from the galactic disc. The first AMR simulation was done by Klein et al. (1994), where it was used to understand the interaction between a shock wave and an embedded cloud, finding that in strong shocks the evolution depends only on the ratio of cloud to intercloud densities. A review of the characteristics of current state of grid-based numerical simulations in astrophysics can be found in Teyssier (2015).

1.4 GH α FaS

Most of the data presented in this thesis was taken with the integral field spectrometer Galaxy H α Fabry-Perot System (GH α FaS) (Hernandez et al. (2008); Fathi et al. (2008)) located at the Nasmyth focus of the 4.2m William Herschel Telescope (WHT) at the Observatorio Roque de los Muchachos (ORM, La Palma) as a visitor instrument. It produces a 3.4x3.4 arcmin data cube with seeing-limited angular resolution (pixel size 0.2 arcsec) and a spectrum at each point on the object, with 48 channels spanning a spectral range which depends on the central wavelength of the emission but is usually $\sim 350 - 400$ km/s, yielding a velocity resolution of $\sim 7-8$ km/s.

A Fabry-Perot interferometer performs 3D spectroscopy by taking consecutive images with a very narrow spectral window at fixed intervals, effectively scanning the spectrum for the entire field. The spectral "steps" can be made very small, so we can achieve very high spectral and spatial resolution, the latter limited only by atmospheric conditions. On the other hand, the spectral range is very small, usually limiting the study to a single spectral line and the narrow bandpass requires quite long observations. The scanning nature of the acquisition can be a problem for nights with variation in weather conditions, as the wavelengths are not measured simultaneously. This is usually mitigated

Este documento incorpora firma electrónica, y es copia auténtica de un documento electrónico archivado por la ULL según la Ley 39/2015.
Su autenticidad puede ser contrastada en la siguiente dirección <https://sede.ull.es/validacion/>

Identificador del documento: 973636 Código de verificación: QpwS3TwF

Firmado por: ARTEMI CAMPS FARIÑA UNIVERSIDAD DE LA LAGUNA	Fecha: 30/06/2017 14:40:15
JOHN E. BECKMAN UNIVERSIDAD DE LA LAGUNA	30/06/2017 15:07:38
JOAN FONT SERRA UNIVERSIDAD DE LA LAGUNA	30/06/2017 15:10:02
ERNESTO PEREDA DE PABLO UNIVERSIDAD DE LA LAGUNA	06/07/2017 13:51:28

by dividing the observation into several cycles of the range, to get uniform conditions for all channels.

The rapid response of the IPCS detector on GHaFaS enables us to minimize these variations by providing a complete spectral scan in only a few minutes, while the large angular throughput implies a major reduction in exposure time for observing extended sources. The IPCS detector, having zero readout noise, is exceptionally suited to observe faint extended objects.

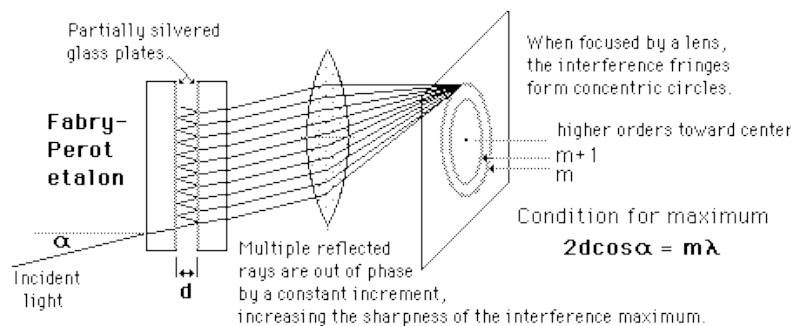


Figure 1.3: Schematic of a Fabry-Perot interferometer.

Figure 1.3 shows the schematic of a Fabry-Perot interferometer, in which the collimated light that enters the instrument passes through semi-reflective glass plates that produce an interferometric pattern of concentric rings as each wavelength exits the plates at a different angle.

The equation for the interference is:

$$2d \cos\alpha = m\lambda \quad (1.8)$$

where d is the distance between the plates, α is the incident angle of the light and m is the interference order. As d varies, so does the radius of each ring, so we can use it to scan the wavelength range over the entire image, i.e. so that every pixel "sees" all the wavelengths in the range. The interference is periodic over the range so as we change the distance we eventually jump to another order $m \pm 1$ and the pattern repeats. For this reason we adjust the parameters so we scan only one order.

The instrument has an intrinsic circular field of view of 4.8' in diameter, but the Nasmyth focus of the telescope limits it to 3.4'x3.4'. The characteristics of the etalon allow us to sample up to 64 channels, though most observations have been taken with 48 channels.

Este documento incorpora firma electrónica, y es copia auténtica de un documento electrónico archivado por la ULL según la Ley 39/2015.
Su autenticidad puede ser contrastada en la siguiente dirección <https://sede.ull.es/validacion/>

Identificador del documento: 973636

Código de verificación: QpwS3TwF

Fecha: 30/06/2017 14:40:15

Firmado por: ARTEMI CAMPS FARIÑA
UNIVERSIDAD DE LA LAGUNA

JOHN E. BECKMAN
UNIVERSIDAD DE LA LAGUNA

JOAN FONT SERRA
UNIVERSIDAD DE LA LAGUNA

ERNESTO PEREDA DE PABLO
UNIVERSIDAD DE LA LAGUNA

30/06/2017 15:07:38

30/06/2017 15:10:02

06/07/2017 13:51:28

The detector is an IPCS (Image Photon Counting System) comprising a CCD with a photomultiplier tube. This system makes the detected signal of a single photon to be 10^6 times above the readout noise of the CCD, effectively meaning there is none for our observations. The cathode of the photomultiplier is refrigerated by a PELTIER cooling device to -30°C , and therefore has negligible thermal noise. These characteristics make a flat field correction unnecessary for our observations, and allow us to divide the observation into many readings as explained above without compromising the signal-to-noise ratio.

1.4.1 Data reduction

Despite being situated at the Nasmyth focus of the WHT (necessary for the stability of the optical components), GH α FaS does not make use of the provided field derotator, as this would reduce the field of view to $2.5' \times 2.5'$ and it has a throughput of only 75%. Using it would limit the utility of our observations, so we choose to take the observations without it and perform the derotation later by software.

Since each individual acquisition is very short on time (a few seconds) we can take them as not affected by field rotation, so that it affects significantly only the resulting cube constructed by summing all of them.

The derotation is performed using the *twirl* IDL routines developed by Javier Blasco Herrera (described in Blasco-Herrera et al. (2010)). It searches for maxima in the individual images and correlates them to match the rotation shift between them. Ideally stars are used, as they remain visible and very bright through all channels, but bright HII regions can also be used. In order to improve detection images close in time of acquisition can be stacked assuming no significant rotation between their exposures. An example is shown in Figure 1.4.

Velocity calibration, phase correction, sky removal and adaptive binning of the cube can be performed using the COMPUTEEVERYTHING procedure described in Daigle et al. (2006), which is the standard procedure to use these data.

1.5 Outline of this thesis

In this thesis we have studied stellar feedback using the bubbles and super-bubbles that it produces, which was accomplished by first developing a novel method to detect the presence of these bubbles and then applying it to integral field spectroscopy data.

Este documento incorpora firma electrónica, y es copia auténtica de un documento electrónico archivado por la ULL según la Ley 39/2015.
Su autenticidad puede ser contrastada en la siguiente dirección <https://sede.ull.es/validacion/>

Identificador del documento: 973636 Código de verificación: QpwS3TwF

Firmado por: ARTEMI CAMPS FARIÑA UNIVERSIDAD DE LA LAGUNA	Fecha: 30/06/2017 14:40:15
JOHN E. BECKMAN UNIVERSIDAD DE LA LAGUNA	30/06/2017 15:07:38
JOAN FONT SERRA UNIVERSIDAD DE LA LAGUNA	30/06/2017 15:10:02
ERNESTO PEREDA DE PABLO UNIVERSIDAD DE LA LAGUNA	06/07/2017 13:51:28

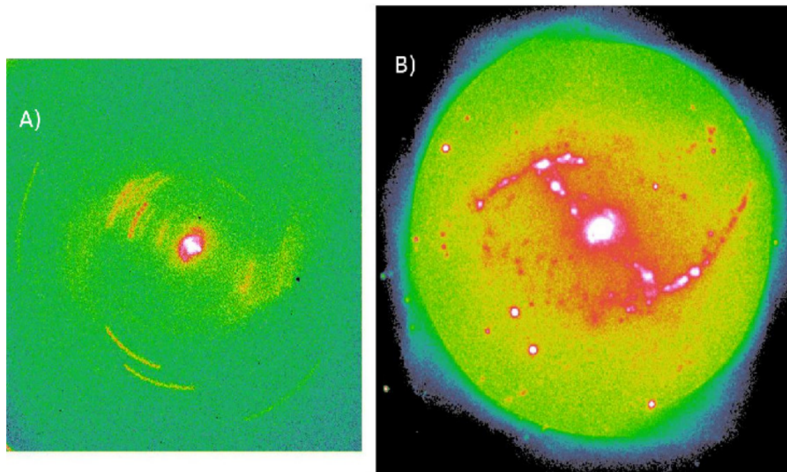


Figure 1.4: The resulting (summed) data cube for a galaxy before (A) and after (B) derotation performed by software. The derotation enlarges the FOV in order to preserve all detected flux. Image taken from Blasco-Herrera (2012).

In Chapter 2 we explain how our method for detecting bubbles works. It uses the mathematical properties of Gaussian functions to detect the presence of multi-peaked emission, which is characteristic of an expanding system, and then fits the profile to obtain the parameters of the peaks. We then use this information to detect the presence of bubbles in the galaxy and obtain their physical properties.

In Chapter 3 we focus on the determination of the uncertainties used to discriminate actual multi-peaked emission from noise, which is extremely important for the method to work. We overview the different methods pursued and present the final result obtained from doing a detailed simulation of the observation and reduction process.

Chapter 4 presents a detection of three nested shells associated with an HII region in the southern arm of M33, which are identified as supernova remnants. This result is remarkable not only because of the presence of three concurrent expanding shells, but also because their masses allow us to infer the existence of remnant molecular gas from the parent cloud of the stellar cluster.

In Chapter 5 we study the Antennae galaxies, an interacting pair of galaxies with a powerful current starburst. We detected 17 superbubbles associated with

Firmado por: ARTEMI CAMPS FARIÑA UNIVERSIDAD DE LA LAGUNA	Fecha: 30/06/2017 14:40:15
JOHN E. BECKMAN UNIVERSIDAD DE LA LAGUNA	30/06/2017 15:07:38
JOAN FONT SERRA UNIVERSIDAD DE LA LAGUNA	30/06/2017 15:10:02
ERNESTO PEREDA DE PABLO UNIVERSIDAD DE LA LAGUNA	06/07/2017 13:51:28

most of the bright HII regions in the galaxy, obtaining their physical properties. We also estimated the kinetic energy contained in the smaller, unresolved, HII regions finding that it is comparable to that of the resolved superbubbles. We also performed hydrodynamic simulations of one of the superbubbles, which allowed us to investigate the how much the approximations we use affect the measured physical parameters.

In Chapter 6 we study Arp 70, another pair of interacting galaxies. On the larger galaxy we detect two especially powerful outflows, one at the centre and the other associated with a giant HII region. We determined the central outflow to be a jet originating in an AGN and estimated its physical properties and kinetic energy, obtaining values of order 10^{57} erg. In the HII region we detected an extremely large superbubble with a diameter of about 5 kpc and an energy of several thousand supernova explosions.

Finally, in Chapter 7 we summarise the main findings of this thesis and discuss future work.

Este documento incorpora firma electrónica, y es copia auténtica de un documento electrónico archivado por la ULL según la Ley 39/2015.
Su autenticidad puede ser contrastada en la siguiente dirección <https://sede.ull.es/validacion/>

Identificador del documento: 973636

Código de verificación: QpwS3TwF

Fecha: 30/06/2017 14:40:15

Firmado por: ARTEMI CAMPS FARIÑA
UNIVERSIDAD DE LA LAGUNA

JOHN E. BECKMAN
UNIVERSIDAD DE LA LAGUNA

JOAN FONT SERRA
UNIVERSIDAD DE LA LAGUNA

ERNESTO PEREDA DE PABLO
UNIVERSIDAD DE LA LAGUNA

30/06/2017 15:07:38

30/06/2017 15:10:02

06/07/2017 13:51:28

2

Development of the method

2.1 Introduction

The study of multi-component emission lines is a topic of major interest as they are produced by many systems in astrophysics. It has long been known that the spectrum of an AGN has two components to its emission, characterised by a narrow and a broad peak each associated with two parts of the system each having very different kinematics (Antonucci (1993)). The presence of an underlying broad supersonic component, which we now know corresponds to unresolved kinematic components, is also characteristic of bright HII regions (Arsenault & Roy (1986); Chu & Kennicutt (1994); Yang et al. (1996)). In this case the observed emission peak may in fact be a combination of the main peak and two unresolved peaks associated with an expanding shell. Multiple peaks also appear in CO observations when independent clouds overlap in the line of sight (Blitz & Stark (1986); Stutzki & Guesten (1990)), and outflows of gas have been observed in ionized and molecular gas (Heckman et al. (1990); Lada (1985); Bally & Lada (1983); Bland & Tully (1988)). It is apparent that the study of these multiple components of an emission line, related to different kinematic phenomena, is relevant to a wide range of astrophysical problems.

2.1.1 Expansion signature

A static HII region shows a simple emission profile consisting of a Gaussian-shaped emission peak broadened by thermal effects. Winds and supernovae from massive stars can produce supersonic shock-waves which coalesce into a thin shell of overdense material expanding away from the centre of the HII region. The ionized gas in these regions is typically optically thin, which means

Firmado por: ARTEMI CAMPS FARIÑA UNIVERSIDAD DE LA LAGUNA	Fecha: 30/06/2017 14:40:15
JOHN E. BECKMAN UNIVERSIDAD DE LA LAGUNA	30/06/2017 15:07:38
JOAN FONT SERRA UNIVERSIDAD DE LA LAGUNA	30/06/2017 15:10:02
ERNESTO PEREDA DE PABLO UNIVERSIDAD DE LA LAGUNA	06/07/2017 13:51:28

that we receive emission from the entirety of the volume it occupies. This is essential to detect expanding structures, as we are simultaneously receiving light from the shell and the HII region.

Objects which move respect to the observer have their spectrum shifted in wavelength per the Doppler effect, which effectively separates the emission originating from the approaching and receding parts of the shell and from the bulk of the HII region.

In Figure 2.1 we show a schematic illustrating the effect, which is most prominent when looking through the centre of the expanding bubble. The wavelength shift depends on projected velocity in the line of sight so looking away from the centre we will detect lower wavelength shifts corresponding to lower projected velocities. Figure 2.2 shows this effect, and was obtained by projecting the velocity field of an expanding surface of perfectly spherical shape.

2.1.2 Instrument suitability

The capability to detect the expansion signatures is heavily dependent on the resolution that can be achieved with the observations, both spatial and spectral, in relation to the typical velocities of the target phenomena. In the case of bubbles or superbubbles the velocities are generally in the range 30-150 km/s (Chu & Kennicutt (1994); Yang et al. (1996); Martin (1996)) for ionized gas and 5-50 km/s for atomic gas (Kamphuis et al. (1991); Chakraborti & Ray (2011); McClure-Griffiths et al. (2002)), requiring very good velocity resolution in both cases. Because of this it is clear that high resolution instruments which take spectra in two dimension, such as Fabry-Perot detectors or aperture synthesis radio telescopes such as VLA and ALMA are ideal in supplying inputs for the kind of multi-peaked profile analysis presented here.

Other methods capable of performing analysis of kinematic components, such as echelle spectrometers can take advantage of the algorithms described here, but those reach their true usefulness with two spatial dimensions, as the number of spatial elements to be analysed grows geometrically. Instruments with one spatial dimension, while also useful for these studies, do not allow a full characterization of the bubble, only along a line usually cutting through the centre of the region. Stepped longslit or long multislit spectra, without cross-dispersion, and fed by fibre bundles produce similar 3-D line profiles to the Fabry-Perot described here, with the advantage of a much wider spectral range. However the instruments available have fields which, at biggest cover an area an order of magnitude smaller than a Fabry-Perot. For this reason when profiling a single emission line the latter is normally used.

An excellent example of the use of echelles in this context can be found in

Este documento incorpora firma electrónica, y es copia auténtica de un documento electrónico archivado por la ULL según la Ley 39/2015.
Su autenticidad puede ser contrastada en la siguiente dirección <https://sede.ull.es/validacion/>

Identificador del documento: 973636

Código de verificación: QpwS3TwF

Fecha: 30/06/2017 14:40:15

Firmado por: ARTEMI CAMPS FARIÑA
 UNIVERSIDAD DE LA LAGUNA

JOHN E. BECKMAN
 UNIVERSIDAD DE LA LAGUNA

JOAN FONT SERRA
 UNIVERSIDAD DE LA LAGUNA

ERNESTO PEREDA DE PABLO
 UNIVERSIDAD DE LA LAGUNA

30/06/2017 15:07:38

30/06/2017 15:10:02

06/07/2017 13:51:28

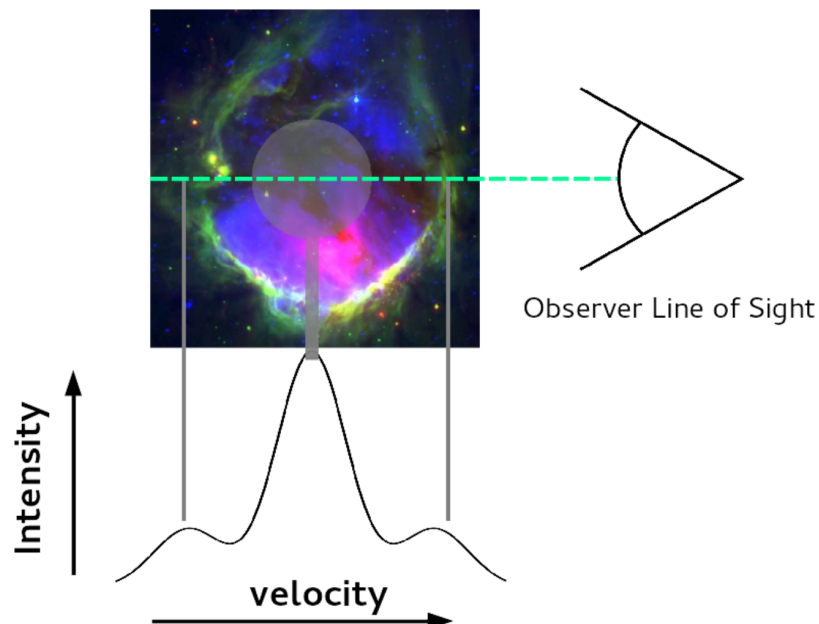


Figure 2.1: Schematic representation of how an expanding shell around an HII region produces the expansion signature. As HII regions are typically optically thin, we receive emission from the entire line of sight. The bulk of the HII region produces most of the flux, with the approaching and receding parts of the shell offset from it on account of Doppler redshift caused by the expansion velocity.

Este documento incorpora firma electrónica, y es copia auténtica de un documento electrónico archivado por la ULL según la Ley 39/2015.
Su autenticidad puede ser contrastada en la siguiente dirección <https://sede.ull.es/validacion/>

Identificador del documento: 973636

Código de verificación: QpwS3TwF

Firmado por: ARTEMI CAMPS FARIÑA
UNIVERSIDAD DE LA LAGUNA

Fecha: 30/06/2017 14:40:15

JOHN E. BECKMAN
UNIVERSIDAD DE LA LAGUNA

30/06/2017 15:07:38

JOAN FONT SERRA
UNIVERSIDAD DE LA LAGUNA

30/06/2017 15:10:02

ERNESTO PEREDA DE PABLO
UNIVERSIDAD DE LA LAGUNA

06/07/2017 13:51:28

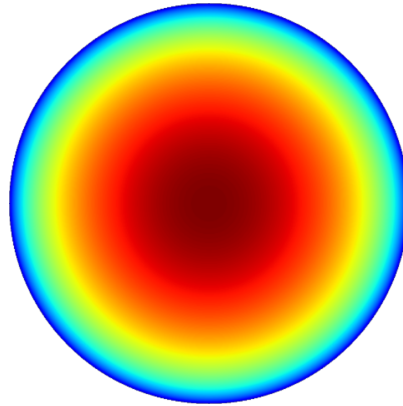


Figure 2.2: Illustration of the projection effect in the detected expansion velocity, colors show velocity, with dark red as the real expansion velocity, highest, and indigo as zero.

Meaburn's article on 30 Doradus (Meaburn (1984))

GH α FaS produces a 3.4x3.4 arcmin data cube with seeing-limited angular resolution (spaxel size ~ 0.2 arcsec) and a spectrum at each point on the object, with 48 channels covering a spectral range which depends on the central wavelength of the emission but is usually ~ 400 km/s, yielding a velocity resolution of ~ 8 km/s for H α . An important feature of GH α FaS system is the IPCS (Image Photon Counting System) detector, which includes a CCD and a photon intensifier. The main advantage this provides, which under many circumstances more than counter balances the lower quantum efficiency, is that it has zero readout noise, an important property when studying extended features of galaxies with low surface brightness which is especially useful when considering very faint secondary peaks. The high kinematic and spatial resolution of this instrument, as well as the sensitivity to faint emission make it ideal for the purposes of this thesis.

2.2 Multi-peaked emission analysis

We aim to detect the presence of multiple components in the emission line profile for each spatial position in the data cube, so we need a way to automatically estimate and fit the components for it to be practical. Otherwise we would have to oversee and interact with a very large number of points (for GH α FaS, with

Este documento incorpora firma electrónica, y es copia auténtica de un documento electrónico archivado por la ULL según la Ley 39/2015.
Su autenticidad puede ser contrastada en la siguiente dirección <https://sede.ull.es/validacion/>

Identificador del documento: 973636 Código de verificación: QpwS3TwF

Firmado por: ARTEMI CAMPS FARIÑA UNIVERSIDAD DE LA LAGUNA	Fecha: 30/06/2017 14:40:15
JOHN E. BECKMAN UNIVERSIDAD DE LA LAGUNA	30/06/2017 15:07:38
JOAN FONT SERRA UNIVERSIDAD DE LA LAGUNA	30/06/2017 15:10:02
ERNESTO PEREDA DE PABLO UNIVERSIDAD DE LA LAGUNA	06/07/2017 13:51:28

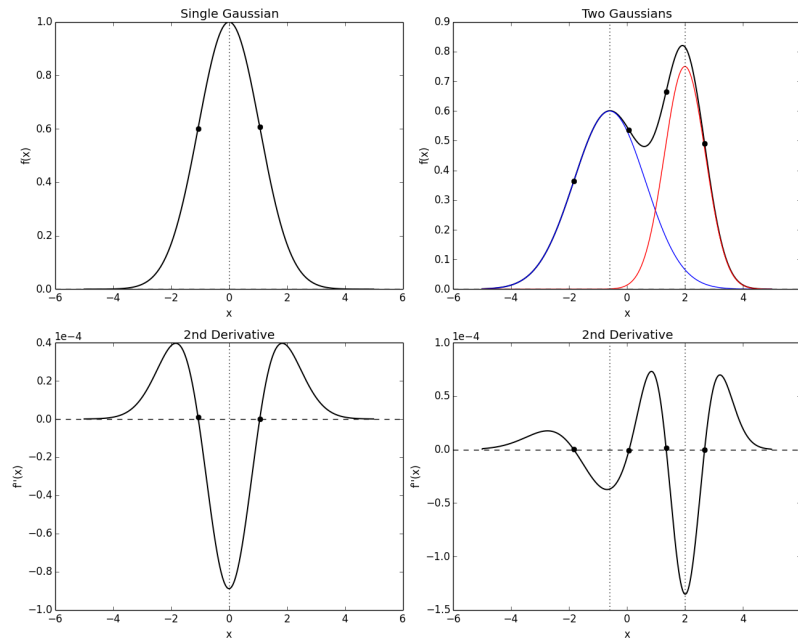


Figure 2.3: Graph illustrating the effectiveness of the second derivative method to separate Gaussian components. The points correspond to the zeros of the second derivative. Note that the centre of any Gaussian lies between two zeros of the second derivative, a positive to negative zero and a negative to positive zero. This holds true regardless of the direction in which you sweep the profile to search for these zeros and is used to find and determine the initial parameters for each Gaussian component.

a 1024x1024 field it is over a million spaxels), which is impractical. To this end we have developed algorithms included in BUBBLY capable of performing this work automatically which yield reliable and precise results.

2.2.1 The second derivative method

In order to obtain the number of Gaussians for each profile and good estimates of their parameters, which is necessary to avoid local minima when fitting, we take advantage of the properties of the second derivative of Gaussians, following Goshtasby & O'Neill (1994).

A single Gaussian, or a normal distribution, $f(x)$, is defined by:

Este documento incorpora firma electrónica, y es copia auténtica de un documento electrónico archivado por la ULL según la Ley 39/2015.
Su autenticidad puede ser contrastada en la siguiente dirección <https://sede.ull.es/validacion/>

Identificador del documento: 973636

Código de verificación: QpwS3TwF

Fecha: 30/06/2017 14:40:15

Firmado por: ARTEMI CAMPS FARIÑA
UNIVERSIDAD DE LA LAGUNA

JOHN E. BECKMAN
UNIVERSIDAD DE LA LAGUNA

JOAN FONT SERRA
UNIVERSIDAD DE LA LAGUNA

ERNESTO PEREDA DE PABLO
UNIVERSIDAD DE LA LAGUNA

30/06/2017 15:07:38

30/06/2017 15:10:02

06/07/2017 13:51:28

$$f(x) = \frac{1}{\sqrt{2\pi}\sigma} e^{-\frac{(x-\mu)^2}{2\sigma^2}} \quad (2.1)$$

where μ and σ are the mean and the standard deviation of the distribution respectively. The second derivative, $f''(x)$, is:

$$f''(x) = \frac{1}{\sqrt{2\pi}\sigma^5} e^{-\frac{(x-\mu)^2}{2\sigma^2}} (\mu^2 - \sigma^2 + x^2 - 2\mu x) \quad (2.2)$$

The second derivative will take the value zero at $x_1 = \mu - \sigma$, and $x_2 = \mu + \sigma$, so, we can estimate the mean and the standard deviation as:

$$\mu = \frac{x_1 + x_2}{2} \quad (2.3)$$

$$\sigma = \frac{x_2 - x_1}{2} \quad (2.4)$$

This can be generalized to a function comprising N Gaussians:

$$f(x) = \sum_{i=1}^{i=N} \frac{1}{\sqrt{2\pi}\sigma_i} e^{-\frac{(x-\mu_i)^2}{2\sigma_i^2}} \quad (2.5)$$

where μ_i and σ_i are the mean and standard deviation of the i-th Gaussian. The second derivative of eq. 2.5 is:

$$f''(x) = \sum_{i=1}^{i=N} \frac{1}{\sqrt{2\pi}\sigma_i^5} e^{-\frac{(x-\mu_i)^2}{2\sigma_i^2}} (\mu_i^2 - \sigma_i^2 + x^2 - 2\mu_i x) \quad (2.6)$$

In order to obtain an initial value of the means and the standard deviations of the Gaussians, and to estimate the ranges of their possible values, we assume that, for any components, i, j , of the sum of Gaussians of comparable standard deviations, $\sigma_i \sim \sigma_j$, their exponential terms in equation 2.6 satisfy:

$$\frac{1}{\sqrt{2\pi}\sigma_j} e^{-\frac{(x-\mu_j)^2}{2\sigma_j^2}} >> \frac{1}{\sqrt{2\pi}\sigma_i} e^{-\frac{(x-\mu_i)^2}{2\sigma_i^2}} \quad (2.7)$$

for $i \neq j$ and for values of x close to μ_j and far enough from μ_i . This implies, but only as an initial approximation from which to start the process, that the Gaussians do not overlap, i.e. that they do not contribute significantly to each other's profile. Then:

$$\mu_i \simeq \frac{x_{i,1} + x_{i,2}}{2} \quad (2.8)$$

Este documento incorpora firma electrónica, y es copia auténtica de un documento electrónico archivado por la ULL según la Ley 39/2015.
Su autenticidad puede ser contrastada en la siguiente dirección <https://sede.ull.es/validacion/>

Identificador del documento: 973636 Código de verificación: QpwS3TwF

Firmado por: ARTEMI CAMPS FARIÑA UNIVERSIDAD DE LA LAGUNA	Fecha: 30/06/2017 14:40:15
JOHN E. BECKMAN UNIVERSIDAD DE LA LAGUNA	30/06/2017 15:07:38
JOAN FONT SERRA UNIVERSIDAD DE LA LAGUNA	30/06/2017 15:10:02
ERNESTO PEREDA DE PABLO UNIVERSIDAD DE LA LAGUNA	06/07/2017 13:51:28

$$\sigma_i \simeq \frac{x_{i,2} - x_{i,1}}{2} \quad (2.9)$$

where $x_{i,1}$ and $x_{i,2}$ are the pair of zeros associated with the i th Gaussian component. This approximation clearly works better as the Gaussians are better resolved, but we want to be able to reach the limit of our spectral resolution, so we use them to estimate initial values and possible ranges used in the subsequent fit.

The limits for the mean are the values for the zeros themselves, $x_{i,1}$ and $x_{i,2}$, preventing each component from overlapping completely with the rest:

$$\mu_i^{\text{final}} \in [x_{i,1}, x_{i,2}] \quad (2.10)$$

We can also set limits to the standard deviations, but we implement them differently depending on whether the approximate value is greater than one spectral (or velocity) resolution element, δ . If it is greater we let it vary between half and double the estimated value, while if it is lower we use the resolution instead:

$$\sigma_i^{\text{final}} \in \begin{cases} \left[\frac{\sigma_i}{2}, 2\sigma_i \right] & \text{if } \sigma_i > \delta \\ \left[\frac{\delta}{2}, 2\delta \right] & \text{if } \sigma_i < \delta \end{cases} \quad (2.11)$$

For the intensity we take the initial value as the intensity of the profile at the estimated mean and limit it to between zero intensity and 1.5 times the estimated value.

At this point we have a complete set of detected components of the profile with their respective estimated intensity, offset velocity and standard deviation, which we can feed to the fitting algorithms to obtain the final results.

2.2.2 Implementation

The second derivative method described above yields the number of Gaussians and a reasonable estimation of their properties, which allows us to perform an automated robust iteration of the process on each spatial point of the cube. BUBBLY performs the entire detecting and fitting process separately for each spatial element, here is a rundown of the steps:

- Check if the spatial element is within the mask for significant emission
- Center the line profile by switching spectral elements
- Detect zeros of the 2nd derivative:

Este documento incorpora firma electrónica, y es copia auténtica de un documento electrónico archivado por la ULL según la Ley 39/2015.
Su autenticidad puede ser contrastada en la siguiente dirección <https://sede.ull.es/validacion/>

Identificador del documento: 973636 Código de verificación: QpwS3TwF

Firmado por: ARTEMI CAMPS FARIÑA UNIVERSIDAD DE LA LAGUNA	Fecha: 30/06/2017 14:40:15
JOHN E. BECKMAN UNIVERSIDAD DE LA LAGUNA	30/06/2017 15:07:38
JOAN FONT SERRA UNIVERSIDAD DE LA LAGUNA	30/06/2017 15:10:02
ERNESTO PEREDA DE PABLO UNIVERSIDAD DE LA LAGUNA	06/07/2017 13:51:28

- Find all instances of a sign change in the 2nd derivative of the profile, corresponding to zeros.
- For the first zero in a pair, check that the value goes from positive to negative (otherwise we are detecting the second zero of a Gaussian out of range) and save it.
- Upon finding a corresponding negative to positive zero, check that the flux is above SNR threshold
- Save zero if it is above the threshold, remove it and the previous zero otherwise.
- Estimate parameters and limits for each pair of zeros.
 - Set maximum flux within zeros as estimated peak intensity I_0 , limits as $[I_{low} = 0, I_{high} = 1.5I_0]$.
 - Set mean of the zeros' velocity as the central velocity v_0 , limits as each zero's velocity.
 - Set half the difference of the zeros' velocity as the velocity dispersion σ_0 , limits as $[\sigma_{low} = 0.5\sigma_0, \sigma_{high} = 2.0\sigma_0]$.
- Perform the Gaussian fitting.
- Do a second pass for better sensitivity:
 - Find brightest peak of the fit and subtract it from the profile.
 - Redo the zero detection process.
 - Check that the residual of the brightest peak was not detected, otherwise remove it. Add the parameters of the main peak from the previous fit.
 - Force minimum intensity of the brightest peak as $0.8 \cdot I_0$ to ensure it remains the dominant peak.
 - Perform the Gaussian fitting
- Save fitted parameters in multiple peak maps for posterior bubble detection.

Before looping this process over all the points we need to do some processing of the cube. BUBBLY requires a mask of significant emission to select the points to be analysed, which can be provided externally or calculated by the dedicated algorithm within its functions. This algorithm combines two masks to select

Este documento incorpora firma electrónica, y es copia auténtica de un documento electrónico archivado por la ULL según la Ley 39/2015.
Su autenticidad puede ser contrastada en la siguiente dirección <https://sede.ull.es/validacion/>

Identificador del documento: 973636 Código de verificación: QpwS3TwF

Firmado por: ARTEMI CAMPS FARIÑA UNIVERSIDAD DE LA LAGUNA	Fecha: 30/06/2017 14:40:15
JOHN E. BECKMAN UNIVERSIDAD DE LA LAGUNA	30/06/2017 15:07:38
JOAN FONT SERRA UNIVERSIDAD DE LA LAGUNA	30/06/2017 15:10:02
ERNESTO PEREDA DE PABLO UNIVERSIDAD DE LA LAGUNA	06/07/2017 13:51:28

the points with relevant emission, on one hand it selects points with emission line like spectrums, by demanding a minimum ratio between the emission on and off-peak. This is done by cutting the profile into two halves, one consisting of the spectral elements closest to the maxima in the profile and the rest in the other. This also ensures that stars are masked out even if they are bright. The other mask demands that the maximum intensity in the profile is above a certain threshold factor of the standard deviation of the spectrum in the faintest points, selected by the percentile.

The code assumes that the cube is continuum subtracted, otherwise the masking algorithm can do it. Given that the code is expected to be used on very narrow spectral ranges comprising one emission line, on which the continuum is effectively flat, so we simply subtract the lowest point of the spectrum.

Before performing the peak detection, we take advantage of the properties of Fabry-Pérot to centre the emission line. This is done by cutting one end of the profile and attaching it to the other side, so that the maximum of the emission is at the central channel.

This can only be done because Fabry-Pérot are cyclical in nature, that is, upon reaching the end of the spectral range the emission jumps one order and appears at the other end. This is why a narrow band filter is necessary, so that only H α emission arrives at the instrument. By centring the profile we ensure that the expansion signature can be properly detected. Otherwise, for the areas of the galaxy which are strongly blue or red shifted in velocity we would lose the spectral range to one side of the main peak, preventing the detection. Naturally, this introduces an ambiguity on the velocity of the secondary peaks, as they could originate on another order for which the narrowband filter still covers its wavelength range. Our analysis assumes the minimum velocity separation possible for the detections, in case that they were from other orders we would need to add the entire spectral range of ~ 400 km/s to the separation, resulting in expansion velocities of upwards of 450 km/s, which are very rare in the cases we are studying.

A real line profile will have noise which, given its fluctuations, will produce a large number of zeros of the second derivative of the profile. There is also the possibility of an out of range peak extending partially into the range, producing an unpaired zero that would throw off the determination of all the components. To account for this we select the valid pair of zeros by imposing a condition that the in first zero the second derivative goes from positive to negative and vice-versa for the second which is characteristic of a true peak (see Fig. 2.3). We also weed out all pairs between which the profile does not reach an intensity above a threshold signal to noise ratio (SNR).

Once we have the final choice of zero pairs we estimate the initial values and

Este documento incorpora firma electrónica, y es copia auténtica de un documento electrónico archivado por la ULL según la Ley 39/2015. Su autenticidad puede ser contrastada en la siguiente dirección https://sede.ull.es/validacion/		
--	--	--

Identificador del documento: 973636	Código de verificación: QpwS3TwF
-------------------------------------	----------------------------------

Firmado por: ARTEMI CAMPS FARIÑA UNIVERSIDAD DE LA LAGUNA	Fecha: 30/06/2017 14:40:15
--	----------------------------

JOHN E. BECKMAN UNIVERSIDAD DE LA LAGUNA	30/06/2017 15:07:38
---	---------------------

JOAN FONT SERRA UNIVERSIDAD DE LA LAGUNA	30/06/2017 15:10:02
---	---------------------

ERNESTO PEREDA DE PABLO UNIVERSIDAD DE LA LAGUNA	06/07/2017 13:51:28
---	---------------------

ranges as explained in the previous section and feed them to the algorithm for multiple Gaussian fitting. Our algorithm has been constructed using modified versions of functions specifically developed to fit Gaussians created by Adam Ginsburg for his *gaussfitter* Python program. This program is a wrapper with multiple options (such as upper and lower limits to the parameters) to the *MPFIT* module for Levenberg-Marquardt least squares fitting¹.

After the first fit, we proceed to subtract the brightest peak, typically associated with the bulk of the HII region, and re-do the detection process. We do this for two reasons: On one hand, it significantly improves the sensitivity to secondary components with low velocity offsets. Low brightness peaks overlapping with the main peak can be missed when performing the zero detection, while clearly appearing after the subtraction. Another reason is for the opposite effect, the SNR criterion for accepting a pair of zeros for fitting is affected by the presence of the main peak. In other words, a low brightness peak originating from noise could pass the SNR check by "riding" on the main peak emission, even if it is a very low addition of flux with respect to it. Upon subtracting the main peak it cannot produce this effect, and thus all secondary peaks are properly detected.

As a result we obtain multi-component line emission surface brightness, velocity and velocity dispersion maps. Since the process is done individually on each spatial point the number of detected components will vary over the field.

We performed extensive tests during implementation to ensure that the method returns the correct parameters for the profiles, finding that the parameter estimation works very well which ensures that the fit will converge easily.

2.2.3 Input parameters

BUBBLY was conceived to run without requiring the user to go into its bowels to obtain the desired results. To achieve this, the parameter file has a total of 39 parameters which can be modified to alter the inner workings of the program as needed. The basic parameters to be set are the file name and minimum SNR of the secondary components, for FP-like data calibrated in velocity this is enough to get correct results. The other parameters allow us to modify the behaviour of **BUBBLY** in a number of ways, here is a short description of their effects and their default parameters if any:

¹Both *gaussfitter* and *MPFIT* python packages can be found at <http://code.google.com/p/agpy/>

Este documento incorpora firma electrónica, y es copia auténtica de un documento electrónico archivado por la ULL según la Ley 39/2015.
Su autenticidad puede ser contrastada en la siguiente dirección <https://sede.ull.es/validacion/>

Identificador del documento: 973636 Código de verificación: QpwS3TwF

Firmado por: ARTEMI CAMPS FARIÑA UNIVERSIDAD DE LA LAGUNA	Fecha: 30/06/2017 14:40:15
JOHN E. BECKMAN UNIVERSIDAD DE LA LAGUNA	30/06/2017 15:07:38
JOAN FONT SERRA UNIVERSIDAD DE LA LAGUNA	30/06/2017 15:10:02
ERNESTO PEREDA DE PABLO UNIVERSIDAD DE LA LAGUNA	06/07/2017 13:51:28

- General processing:

- [RERUN (0)] Perform only bubble detection: When set to 1 the program skips the peak detection and fitting part, requires that component maps have previously been obtained.
- [MONO_MAP (0), MONO_NAME] The program calculates a zero moment map from the cube for calculations, setting the first option to one and the file name makes the program use the external file.
- [CENTERING (1)] Allows the user to disable profile line centring, useful when not using FP data.
- [SMOOTH (0), XY_KERNEL (2), SPEC_KERNEL (0)] In-built gaussian smoothing is available prior to the analysis, the spatial and spectral directions can be smoothed at different levels, with 0 meaning no smoothing in that dimension.

- Cube data type

- [Z_TYPE (0)] Informs the program as to the units of the spectral dimension between velocity (0), wavelength (1) and frequency (2).
- [VEL_SCALE (1)] The program assumes units for velocity in km/s, if the cube is in other units it can be corrected with this parameter.
- [FREQ_SCALE (1.0e9)] When it performs the conversion the program assumes Hz as the unit, other units need a correction with this parameter.
- [LAMBDA_SCALE (1.0e9)] The same as above but for wavelength, assuming Angstroms as the base unit.
- [LAMBDA_R (6562.78)] The rest wavelength of the emission, allows use of frequency or wavelength Z-unit cubes which do not observe H α .

- Output files

- [COMP_OUT (0)] When set to 1, outputs the component maps containing all detected components of the profile. These maps are required when using the [RERUN] option.
- [MAIN_OUT (1)] When set to 1, outputs the moment maps of the main peak of the emission (intensity, velocity, dispersion).
- [INT_TYPE (0)] Controls whether the flux maps for the detected bubbles are output in absolute units (1) or relative to the main peak (0).

Este documento incorpora firma electrónica, y es copia auténtica de un documento electrónico archivado por la ULL según la Ley 39/2015.
Su autenticidad puede ser contrastada en la siguiente dirección <https://sede.ull.es/validacion/>

Identificador del documento: 973636

Código de verificación: QpwS3TwF

Fecha: 30/06/2017 14:40:15

Firmado por: ARTEMI CAMPS FARIÑA
 UNIVERSIDAD DE LA LAGUNA

JOHN E. BECKMAN
 UNIVERSIDAD DE LA LAGUNA

JOAN FONT SERRA
 UNIVERSIDAD DE LA LAGUNA

ERNESTO PEREDA DE PABLO
 UNIVERSIDAD DE LA LAGUNA

30/06/2017 15:07:38

30/06/2017 15:10:02

06/07/2017 13:51:28

- [CALIB_A (1), CALIB_B (0), CALIB_C (1)] Calibration parameters for the flux, allow for an arbitrary unit conversion of the parameters used to calculate the flux. The output flux is calculated as follows: $F = \sqrt{\pi}(A \cdot I + B) \cdot (C \cdot \sigma)$.
- [PROF_OUT (0)] Controls whether the spectra with detected expansion are output as png plots of the fit. This is set off (0) by default as it takes a long time to produce and write to disc the files.
- [PROF_VUNIT (km/s), PROF_IUNIT (arb.un.)] Labels for the axes of the plots.

- Noise and masking

- [NOISE_DET (1)] Controls whether the program uses the internal noise and masking algorithm or the user provides the mask and noise cube.
- [FLUX_RATIO (1.5)] Parameter for producing the mask, ratio between on and off-peak emission. Higher values make the algorithm stricter to accept a point as having valid emission.
- [NOISE_PERC (0.005)] Parameter for producing the mask, percentile of points most similar to noise (flat emission profile) to be used to compute a general noise value.
- [MAX_TO_NOISE (20)] Parameter for producing the mask, minimum ratio of maximum intensity to the noise value.
- [CONT_COR (1)] Controls whether the continuum is subtracted.
- [CONT_OUT (1)] Controls whether the measured continuum is output to a file.

- Bubble detection

- [MAIN_EXT (0), MAIN_NAME] When the first is set to 1, the program uses a user-provided file ([MAIN_EXT]) for the central velocity instead of choosing an emission peak as the central value. Useful for cases where we expect the emission of the shell to dominate, such as HI observations.
- [BUB_V_SIGMA (2)] Maximum deviation in the velocity offset towards the central velocity that two peaks are allowed to have to be considered an expansion signature. The number is a factor of the velocity resolution.

Este documento incorpora firma electrónica, y es copia auténtica de un documento electrónico archivado por la ULL según la Ley 39/2015.
Su autenticidad puede ser contrastada en la siguiente dirección <https://sede.ull.es/validacion/>

Identificador del documento: 973636 Código de verificación: QpwS3TwF

Firmado por: ARTEMI CAMPS FARIÑA UNIVERSIDAD DE LA LAGUNA	Fecha: 30/06/2017 14:40:15
JOHN E. BECKMAN UNIVERSIDAD DE LA LAGUNA	30/06/2017 15:07:38
JOAN FONT SERRA UNIVERSIDAD DE LA LAGUNA	30/06/2017 15:10:02
ERNESTO PEREDA DE PABLO UNIVERSIDAD DE LA LAGUNA	06/07/2017 13:51:28

- [BUB_USE_I (0)] When set to 1, the program demands that the intensity of two peaks be similar to a degree to accept them as an expansion signature
- [BUB_LR (0.5)] Maximum difference in intensity between two peaks to be accepted as an expansion signature, as a factor of $(I_1 - I_2) / (I_1 + I_2)$.
- [BUB_USE_D (0)] When set to 1, the program demands that the dispersion of two peaks be similar to a degree to accept them as an expansion signature
- [BUB_D_R (0.5)] Maximum difference in dispersion between two peaks to be accepted as an expansion signature, as a factor of $(D_1 - D_2) / (D_1 + D_2)$.

2.3 Application to expanding structures

We can easily apply the results from the multi-peak fit to search for expanding structures. The kinematics along the line of sight for an expanding shell around an HII region present three peaks, one in the middle produced by the bulk of the region, one for the gas approaching us because of the expansion, and a corresponding peak receding from us emitted by the far side of the shell. Because of this we define the expansion signature that we will seek in the profiles as a bright main emission peak, coming from the bulk of an HII region, and two secondary peaks placed symmetrically, one at each side of the main peak.

The inhomogeneity of the ISM, the effect of the density profile of the gas decreasing perpendicularly to the disc and instrumental error will generally cause these two velocities to differ slightly from perfect symmetry, so we allow a maximum deviation from symmetry with respect to the central peak of twice the spectral resolution of our instrument, $2\delta v \sim 16 \text{ km/s}$. Tests were performed comparing the results obtained using different allowed deviations. Initially we used a deviance of δv , the instrumental error for these measurements, but we found that the $2\delta v$ maps contained the same features as the δv maps, i.e. no additional macroscopic features, and the structures detected for each feature appeared more complete. Further tests using $3\delta v$ did not yield more coherent structures but did introduce false signatures, so the $2\delta v$ window was used throughout this work.

Once it has the multiple component maps BUBBLY determines the main peak of the line profile for each spatial point, using flux as the criterion, and then checks the other detected peaks to find a pair that satisfies the conditions imposed. It then creates a map containing the mean separation between these

Este documento incorpora firma electrónica, y es copia auténtica de un documento electrónico archivado por la ULL según la Ley 39/2015.
Su autenticidad puede ser contrastada en la siguiente dirección <https://sede.ull.es/validacion/>

Identificador del documento: 973636 Código de verificación: QpwS3TwF

Firmado por: ARTEMI CAMPS FARIÑA UNIVERSIDAD DE LA LAGUNA	Fecha: 30/06/2017 14:40:15
JOHN E. BECKMAN UNIVERSIDAD DE LA LAGUNA	30/06/2017 15:07:38
JOAN FONT SERRA UNIVERSIDAD DE LA LAGUNA	30/06/2017 15:10:02
ERNESTO PEREDA DE PABLO UNIVERSIDAD DE LA LAGUNA	06/07/2017 13:51:28

peaks (the expansion velocity at that point) and another map with their mean intensity. For this work we generally use instead the relative intensity with respect to the total intensity in order to use fluxes obtained from narrow band images: $I_b = 0.5 * (I_1/I + I_2/I)$, where I_b is the intensity of the bubble, I_1 and I_2 are the secondary peaks' intensity and I the intensity of the main peak. This is done because we trust the photometric calibration of a narrow band image better than calibrating the flux of the instrument. BUBBLY offers the option of imposing additional conditions on the secondary peaks to accept them as an expansion signature, namely having similar intensities and velocity dispersions for the symmetric pairs.

Another result of the overall mapping process is a velocity map of the main peak, which gives the overall kinematics of the galaxy. This map is an alternative to the usual method for obtaining a kinematic map in H α which uses the moments method. The latter calculates the moments of the line profile to find the central "characteristic" velocity, while our algorithm takes the velocity of the brightest peak of each profile. In general our algorithm gives a more reliable result, because if there are secondary emission peaks these will weight the moments method and give a distorted value for the velocity of the spaxel concerned. However in kinematically complex environments, where there may be a number of peaks with comparable intensities, one can obtain artificial jumps in the velocity map using our algorithm, because it selects the brightest of these peaks, regardless of whether this represents the overall underlying velocity, while the moments method finds an average, and smooths the differences.

2.3.1 Finding the expanding structures

After processing the data cube with BUBBLY the main products we obtain are the expansion velocity map, the intensity map and velocity, the intensity and dispersion maps for the main peak. The first two are the relevant ones for the study of superbubbles, as they are what we will use to detect and characterise them. In Fig. 2.5 we show the expansion map of the Antennae galaxies and its corresponding H α narrow band image as an example of the products of our method. It can be seen in the image that the centres of the superbubbles detected coincide well with the centres of the brightest HII regions.

We detect the superbubbles by inspecting the expansion map to find regions with coherent patterns in the expansion velocity that correspond to the expected radial distribution of observed expansion velocity characteristic of superbubbles. These arise from the fact that the velocities we measure are the components directed along the line of sight due to the Doppler effect, so a spherically expanding shell will show projection effects on the expansion map.

Este documento incorpora firma electrónica, y es copia auténtica de un documento electrónico archivado por la ULL según la Ley 39/2015.
Su autenticidad puede ser contrastada en la siguiente dirección <https://sede.ull.es/validacion/>

Identificador del documento: 973636 Código de verificación: QpwS3TwF

Firmado por: ARTEMI CAMPS FARIÑA UNIVERSIDAD DE LA LAGUNA	Fecha: 30/06/2017 14:40:15
JOHN E. BECKMAN UNIVERSIDAD DE LA LAGUNA	30/06/2017 15:07:38
JOAN FONT SERRA UNIVERSIDAD DE LA LAGUNA	30/06/2017 15:10:02
ERNESTO PEREDA DE PABLO UNIVERSIDAD DE LA LAGUNA	06/07/2017 13:51:28

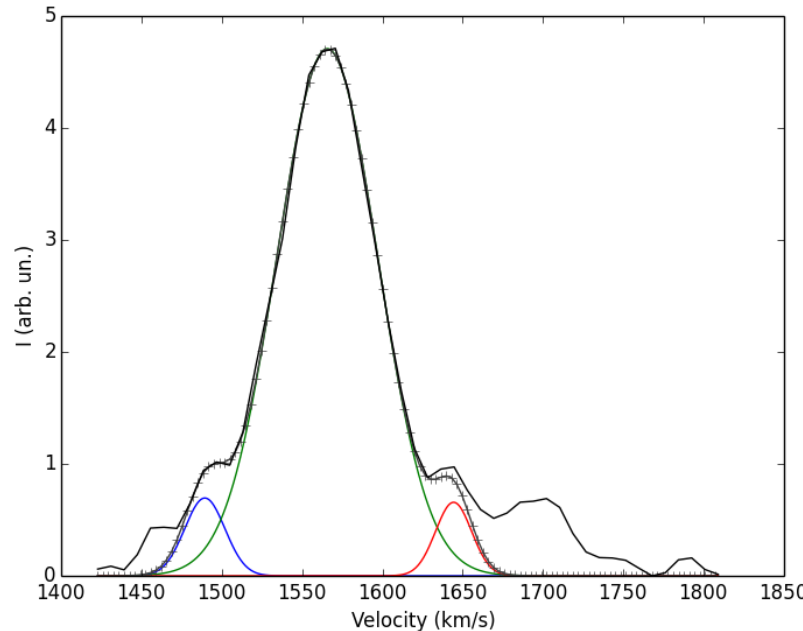


Figure 2.4: Example of expansion detection in an HII region of the Antennae (see Fig 2.5). The individual components (green, red and blue) are plotted along with the profile (black) and the fit result (crosses). The brightest, main peak corresponds to the emission from the bulk of the HII region, and the two smaller, symmetrically placed peaks on each side correspond to the approaching and receding parts of the superbubble along the line of sight in that particular spatial point. Further peaks can be observed on the profile, but they are not taken into consideration here as they are not symmetric in velocity about the central peak, which they would be in the case of expansion. They represent a complexity of kinematic structure which is clearly present, but which we are, for the present, not pursuing in detail.

Este documento incorpora firma electrónica, y es copia auténtica de un documento electrónico archivado por la ULL según la Ley 39/2015.
Su autenticidad puede ser contrastada en la siguiente dirección <https://sede.ull.es/validacion/>

Identificador del documento: 973636

Código de verificación: QpwS3TwF

Firmado por: ARTEMI CAMPS FARIÑA
UNIVERSIDAD DE LA LAGUNA

Fecha: 30/06/2017 14:40:15

JOHN E. BECKMAN
UNIVERSIDAD DE LA LAGUNA

30/06/2017 15:07:38

JOAN FONT SERRA
UNIVERSIDAD DE LA LAGUNA

30/06/2017 15:10:02

ERNESTO PEREDA DE PABLO
UNIVERSIDAD DE LA LAGUNA

06/07/2017 13:51:28

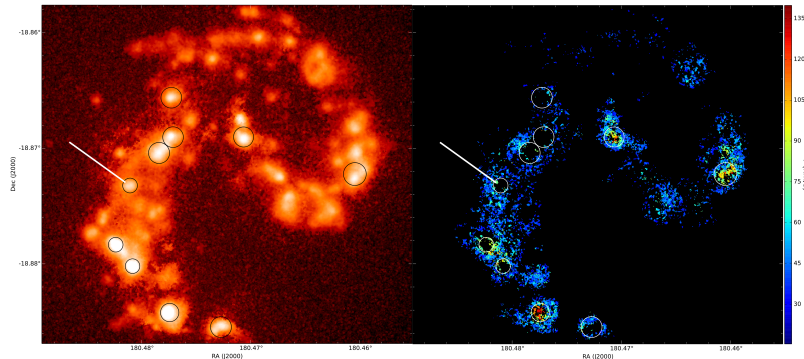


Figure 2.5: Comparison between the H α narrow band image (left) of the Antennae galaxies and the corresponding expansion map (right). The circles represent the estimated bubble radii and the white line signals the position for the H α profile shown in Fig. 2.4. The scale is velocity separation (in absolute values) with respect to the main peak produced by the bulk of the HII region, obtained by taking the average separation of the approaching and receding peaks.

Therefore, observed expansion velocity will be highest at the centre of the bubble where the velocity vector aligns with the line of sight, decreasing radially until it is zero at the edge, so we look for radially decreasing circular patterns in the map.

A particularly clear case of a detected superbubble from the Antennae is shown in Fig. 2.6 with the estimated bubble size and position shown by a white circle.

Multiple expanding features

In some cases around the brightest HII regions, profiles exhibiting multiple pairs of symmetrically separated peaks can be observed (Fig. 2.7). These additional features follow the same general shape as the main detected superbubbles, forming rings around the HII regions, but they are not as common and the analysis and determination of their properties is more difficult.

However, they represent a very interesting possibility as their presence may imply multiple bursts of star formation in the same regions or perhaps a system of more local bubbles inside the large region and its associated superbubble. Another possibility to explain the presence of multiple expansion signatures in a spaxel would be that we are detecting kinematics which are considerably

Este documento incorpora firma electrónica, y es copia auténtica de un documento electrónico archivado por la ULL según la Ley 39/2015.
Su autenticidad puede ser contrastada en la siguiente dirección <https://sede.ull.es/validacion/>

Identificador del documento: 973636

Código de verificación: QpwS3TwF

Fecha: 30/06/2017 14:40:15

Firmado por: ARTEMI CAMPS FARIÑA
UNIVERSIDAD DE LA LAGUNA

JOHN E. BECKMAN
UNIVERSIDAD DE LA LAGUNA

JOAN FONT SERRA
UNIVERSIDAD DE LA LAGUNA

ERNESTO PEREDA DE PABLO
UNIVERSIDAD DE LA LAGUNA

30/06/2017 15:07:38

30/06/2017 15:10:02

06/07/2017 13:51:28

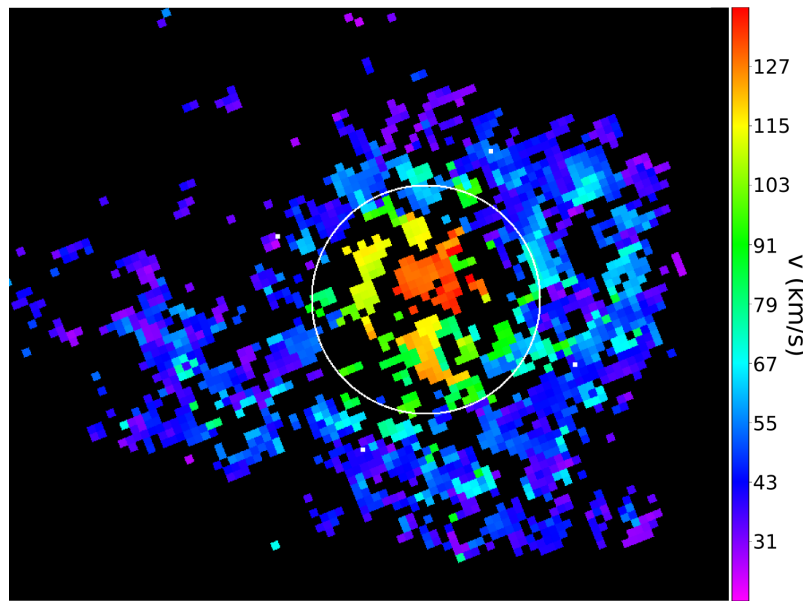


Figure 2.6: Detail of a superbubble detected in the brightest HII region in the Antennae galaxies. The scale is velocity with respect to the emission from the bulk of the HII region and the white circle represents the estimated superbubble radius. As expected from an expanding structure, we can see the highest velocity at the centre, falling to lower values towards the edge. The spatial coherence and effect of projection on the observed velocity can be well seen in this example.

Este documento incorpora firma electrónica, y es copia auténtica de un documento electrónico archivado por la ULL según la Ley 39/2015.
Su autenticidad puede ser contrastada en la siguiente dirección <https://sede.ull.es/validacion/>

Identificador del documento: 973636

Código de verificación: QpwS3TwF

Firmado por: ARTEMI CAMPS FARIÑA
UNIVERSIDAD DE LA LAGUNA

Fecha: 30/06/2017 14:40:15

JOHN E. BECKMAN
UNIVERSIDAD DE LA LAGUNA

30/06/2017 15:07:38

JOAN FONT SERRA
UNIVERSIDAD DE LA LAGUNA

30/06/2017 15:10:02

ERNESTO PEREDA DE PABLO
UNIVERSIDAD DE LA LAGUNA

06/07/2017 13:51:28

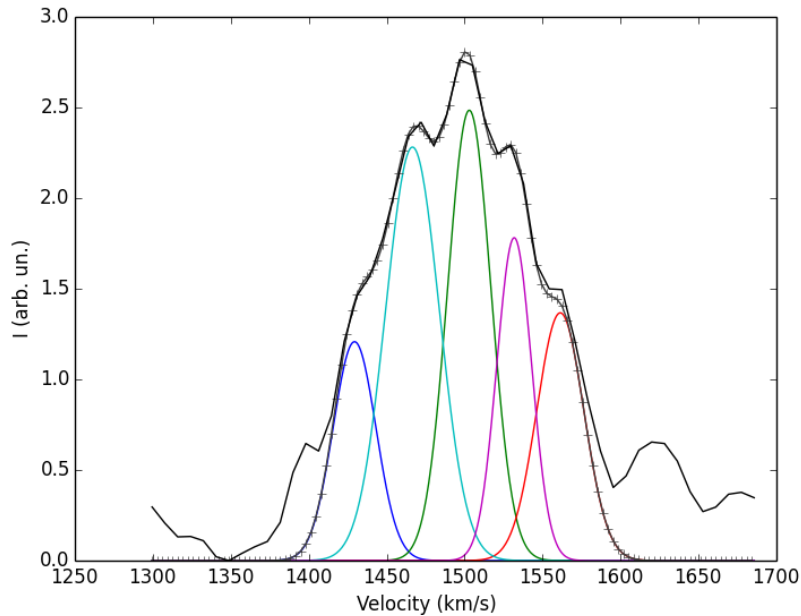


Figure 2.7: Profile observed in the Antennae galaxies where two pairs of symmetrically spaced secondary peaks are detected, implying the possible presence of two superbubbles in one region. An alternative possibility is that it could be a projection effect with two HII regions overlapping on the line of sight which may indicate more complex kinematics. As in Fig. 2.4 we show separated peaks only for detected components that are symmetrical to the main peak.

more complex than that of an assumed superbubble.

In Chapter 4 we show an interesting example of a detection of multiple resolved shells and its implications for the evolution of the HII region.

2.3.2 Bubble properties

The amount of information about a bubble or shell that we can extract is critical for our method to be truly useful. We have four primary quantities from which we may derive the physical parameters of a particular bubble: the radius, the HII region luminosity, the shell to region luminosity ratio, and the expansion velocity of the shell. We can calculate the bubble luminosity, density, mass, kinetic energy and age. The basic equation we use is the luminosity of a

Este documento incorpora firma electrónica, y es copia auténtica de un documento electrónico archivado por la ULL según la Ley 39/2015.
Su autenticidad puede ser contrastada en la siguiente dirección <https://sede.ull.es/validacion/>

Identificador del documento: 973636

Código de verificación: QpwS3TwF

Firmado por: ARTEMI CAMPS FARIÑA
UNIVERSIDAD DE LA LAGUNA

Fecha: 30/06/2017 14:40:15

JOHN E. BECKMAN
UNIVERSIDAD DE LA LAGUNA

30/06/2017 15:07:38

JOAN FONT SERRA
UNIVERSIDAD DE LA LAGUNA

30/06/2017 15:10:02

ERNESTO PEREDA DE PABLO
UNIVERSIDAD DE LA LAGUNA

06/07/2017 13:51:28

shell (Relaño & Beckman (2005))

$$L_{H\alpha}(\text{shell}) = 4\pi R^2 \Delta R n_e^2 \alpha(H, T) h\nu \quad (2.12)$$

Among the parameters appearing in this equation are the effective recombination coefficient for hydrogen $\alpha_{H\alpha}^{\text{eff}}(H, T)$, which can be taken as $4 \cdot 10^{-13}$ for HII regions (Osterbrock (1989)), $h\nu_{H\alpha}$ is the energy of an $H\alpha$ photon and the shell width ΔR which we usually take as 15% of the radius. We do not expect this ratio to vary much from case to case and when calculating the mass and subsequent quantities its contribution varies as $\Delta R^{-1/2}$, so it does not affect the final result very strongly. Observational uncertainties give a much larger possible variation so we can safely consider it as constant.

Since we already know the luminosity of the shell from the product of the region luminosity and the shell-to-region luminosity ratio we are especially interested in the density to calculate the total mass of the shell and its energy. We can also make a zero order estimate of the age of the bubble by dividing the radius by the expansion velocity, which is equivalent to assuming the region has expanded at constant velocity. Thus:

$$n_e = \sqrt{\frac{L_{H\alpha}(\text{shell})}{4\pi R^2 \Delta R \alpha_{H\alpha}^{\text{eff}}(H, T) h\nu_{H\alpha}}} \quad (2.13)$$

$$M = 4\pi R^2 \Delta R n_e m_p \quad (2.14)$$

$$E_k = \frac{1}{2} M * v_{exp}^2 \quad (2.15)$$

$$\text{Age} = R/v_{exp} \quad (2.16)$$

The errors for the parameters are determined by propagation of the errors in radius, expansion velocity and $H\alpha$ luminosity. The first two parameters are estimated by us directly by inspection of the expansion map, so we took a conservative error of 10% for both radius and expansion velocity. For the luminosity the most important source of error is, by far, the uncertainty in the radius of the region, though it does not propagate in a mathematically straightforward way as it affects the pixels over which we sum the detected flux and depends on the physical characteristics of each region. What we do is measure three sets of fluxes for each region, two of which correspond to the high and low extreme values of the radius as allowed by the radius error, and take their mean deviation from the central value as the error for the flux.

Este documento incorpora firma electrónica, y es copia auténtica de un documento electrónico archivado por la ULL según la Ley 39/2015.
Su autenticidad puede ser contrastada en la siguiente dirección <https://sede.ull.es/validacion/>

Identificador del documento: 973636 Código de verificación: QpwS3TwF

Firmado por: ARTEMI CAMPS FARIÑA UNIVERSIDAD DE LA LAGUNA	Fecha: 30/06/2017 14:40:15
JOHN E. BECKMAN UNIVERSIDAD DE LA LAGUNA	30/06/2017 15:07:38
JOAN FONT SERRA UNIVERSIDAD DE LA LAGUNA	30/06/2017 15:10:02
ERNESTO PEREDA DE PABLO UNIVERSIDAD DE LA LAGUNA	06/07/2017 13:51:28

Age dating

A precise determination of the age of a superbubble is very important as it is equivalent to the age of the associated HII region and can therefore be used to give a short-term map of the star forming history of the galaxy. There are analytic solutions for the ideal case of a bubble expanding in a homogeneous, isotropic medium, with $t = 0.6R/v$ typically used for wind-blown bubbles and equivalent relations for supernova remnants. In general, the bubbles studied in this work do not fulfill the conditions that make these relations valid, especially since the relations assume a constantly decreasing velocity with time, while superbubbles in the break-out phase can in fact accelerate in the direction of elongation. For these cases we prefer to make less assumptions and give a simple estimation of the age as simply R/v_{exp} . This is the solution for free expansion, and while the actual age should remain of the same order, it can be used as a lower limit for age except for bubbles which are strongly accelerating into the intergalactic medium.

A better approach to the issue is therefore necessary and entails models of the interaction. We have experimented with analytic models for the expansion of superbubbles with moderate success, comparison with observations of line equivalent widths in clusters to produce their stellar ages gives compatible ages in most cases, especially for the younger regions. The models assume homogeneous distribution of gas in all directions, while in reality and on the scales we are studying, it becomes necessary to take into account the 3D shape of the distribution. See Chapter 5 for more details.

2.3.3 Approximations

The determination of the physical parameters from the observables naturally depends on a number of approximations, which affect the results in different ways. The first and foremost approximation is the assumption of a perfectly spherical shell. This is the case that arises from the ideal theoretical case of uniform and isotropic momentum injection into an equally isotropic and homogeneous medium. This approximation holds well for smaller scales of a few dozen pc provided that the medium is not highly inhomogeneous, such as having remnants of molecular clouds around a young cluster.

On larger scales, however, the general shape of the galaxy comes into effect. There have been many theoretical and simulation studies of the evolution of such superbubbles (Mac Low & McCray (1988); Zaninetti (2004)), all of them concluding that they soon acquire an elongated shape, with the long axis perpendicular to the plane of the galaxy, as the ambient density decreases in that

Este documento incorpora firma electrónica, y es copia auténtica de un documento electrónico archivado por la ULL según la Ley 39/2015.
Su autenticidad puede ser contrastada en la siguiente dirección <https://sede.ull.es/validacion/>

Identificador del documento: 973636 Código de verificación: QpwS3TwF

Firmado por: ARTEMI CAMPS FARIÑA UNIVERSIDAD DE LA LAGUNA	Fecha: 30/06/2017 14:40:15
JOHN E. BECKMAN UNIVERSIDAD DE LA LAGUNA	30/06/2017 15:07:38
JOAN FONT SERRA UNIVERSIDAD DE LA LAGUNA	30/06/2017 15:10:02
ERNESTO PEREDA DE PABLO UNIVERSIDAD DE LA LAGUNA	06/07/2017 13:51:28

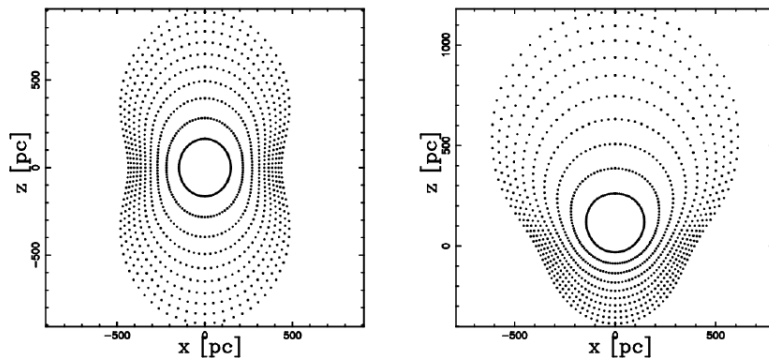


Figure 2.8: Results of two hydrodynamic simulations from Zaninetti (2004) showing the effects of a density gradient associated with a galaxy disc. The figures show the shape and size of consecutive snapshots in the bubble evolution as dotted lines.

direction, morphing into a peanut shape for bigger and older superbubbles (see Figure 2.8). The projection effects described still apply, but it can be expected, for example, that the observed projected expansion velocity will be affected. As the superbubble has a peanut shape its observed edge as seen from above will not have a zero value of the vertical velocity, so we still see the gradient, but the expansion velocity will decrease more slowly and we will stop detecting the bubble before it approaches zero. The expansion velocity profiles we have found for larger bubbles do agree better with the elongated case.

Under these circumstances the bubble does not have the same properties over its entire extend, as was the case for a perfectly spherical bubble. The density and expansion velocity are very different along directions with different ambient density.

Another point to be taken into account is that our calculations for the mass, and subsequently the kinetic energy only refer to the ionized gas in the shell, ignoring any possible presence of neutral or molecular phases of hydrogen. We also ignore the presence of other elements in the gas. These should not affect the results much, the shells tend to be more ionized than the HII region itself on account of the collisional excitation produced by the shock, and the gas it sweeps up should follow suit. As for the presence of other elements, this is not a big deviation as we are equating one electron to one hydrogen atom; heavier elements have conversely more electrons, so the error lies in the difference between the mass of an atom of atomic number N and N hydrogen

atoms. This is not a big difference, and hydrogen greatly dominates the element distribution in the gas regardless.

2.4 Discussion

We have presented our method and associated software designed to detect and fit multiple components to integral field spectroscopy of emission lines, with an application to superbubbles using our Fabry-Perot instrument.

In section 3 we have explained in detail the method for the line profile decomposition into a set of Gaussians and the way it is implemented in BUBBLY. The next section applied the results from the decomposition to produce expansion maps that can be used to search for and characterise superbubbles. In this regard with a relatively simple approach we already obtain reliable detection and characterization of superbubbles.

The presence of multiple components in an emission line is a powerful way to study the fainter, and more difficult to detect, kinematic phenomena in a galaxy, as well as numerous other applications such as separating the emission of different regions or clouds or even galaxies that overlap or AGN and violent galactic outflows (see §3.2). Our algorithm has the advantage of being both simple and easy to use and very flexible with regards to the input data, which makes it a potent tool to study galaxy kinematics.

In this chapter we have centred on the application of multi-component analysis to the search and characterisation of superbubbles, where the method proves especially useful allowing us to detect several superbubbles clearly associated with giant HII regions. The fact that it does not need purpose-programmed observations to work means it offers added value to integral field spectroscopy observations of galaxies.

Current alternative methods for the detection of superbubbles are to use morphological features observed through narrow H α filters such as cavities and arches around OB associations, shock-fuelled forbidden emission lines such as SII and OIII and morphological and kinematic features in HI. X-ray observations of extended emission interior to the observed shells is a complementary diagnostic.

All morphology-based methods require very high spatial resolution and shells which are bright with respect to their surroundings in order to detect them, which restricts the methods to nearby galaxies and/or observations with very high angular resolution. This is not the case for our method, where the shell emission is separated from the HII region emission kinematically, although of course with better angular resolution we will be able to detect more and smaller bubbles.

Este documento incorpora firma electrónica, y es copia auténtica de un documento electrónico archivado por la ULL según la Ley 39/2015.
Su autenticidad puede ser contrastada en la siguiente dirección <https://sede.ull.es/validacion/>

Identificador del documento: 973636 Código de verificación: QpwS3TwF

Firmado por: ARTEMI CAMPS FARIÑA UNIVERSIDAD DE LA LAGUNA	Fecha: 30/06/2017 14:40:15
JOHN E. BECKMAN UNIVERSIDAD DE LA LAGUNA	30/06/2017 15:07:38
JOAN FONT SERRA UNIVERSIDAD DE LA LAGUNA	30/06/2017 15:10:02
ERNESTO PEREDA DE PABLO UNIVERSIDAD DE LA LAGUNA	06/07/2017 13:51:28

Except for HI cube observations the other methods do not provide kinematics of the shell which prevents a detailed characterization of the bubble and its dynamic properties, limiting the utility of the data. It would be possible to complement the observations with high-resolution spectra to detect the expanding components but the total observing time required would be very high, considering that each region would require an individual spectrum.

The most direct competition for our method when it is applied to superbubbles is, therefore, observing HI using the classical 21 cm method. The long wavelength of this HI emission makes it very difficult to achieve the spatial resolution necessary to distinguish these features properly, (even though the velocity resolution is high), making it very difficult to extend these studies beyond the closest galaxies in the local group, such as M101 where several shells have been detected in this manner (Kamphuis et al. (1991); Chakraborti & Ray (2011)).

In any case the shells detected with HI normally correspond to the late stages of the superbubble, after the massive stars which ionized the shell have disappeared and the superbubble has decelerated greatly. Because of this the typical expansion velocities lie in the range 5-50 km/s (Kamphuis et al. (1991); Chakraborti & Ray (2011); McClure-Griffiths et al. (2002)) and in many cases it is difficult or impossible to find the OB association corresponding to the superbubble. This is not the case for our method which traces the superbubbles from the ionized gas, so we find young superbubbles clearly associated with the cluster. In this manner, it can be said that HI observations and ours are complementary, each detecting superbubbles in different stages of their evolution.

Este documento incorpora firma electrónica, y es copia auténtica de un documento electrónico archivado por la ULL según la Ley 39/2015.
Su autenticidad puede ser contrastada en la siguiente dirección <https://sede.ull.es/validacion/>

Identificador del documento: 973636

Código de verificación: QpwS3TwF

Fecha: 30/06/2017 14:40:15

Firmado por: ARTEMI CAMPS FARIÑA
UNIVERSIDAD DE LA LAGUNA

JOHN E. BECKMAN
UNIVERSIDAD DE LA LAGUNA

JOAN FONT SERRA
UNIVERSIDAD DE LA LAGUNA

ERNESTO PEREDA DE PABLO
UNIVERSIDAD DE LA LAGUNA

30/06/2017 15:07:38

30/06/2017 15:10:02

06/07/2017 13:51:28

Este documento incorpora firma electrónica, y es copia auténtica de un documento electrónico archivado por la ULL según la Ley 39/2015.
Su autenticidad puede ser contrastada en la siguiente dirección <https://sede.ull.es/validacion/>

Identificador del documento: 973636

Código de verificación: QpwS3TwF

Firmado por: ARTEMI CAMPS FARIÑA
UNIVERSIDAD DE LA LAGUNA

Fecha: 30/06/2017 14:40:15

JOHN E. BECKMAN
UNIVERSIDAD DE LA LAGUNA

30/06/2017 15:07:38

JOAN FONT SERRA
UNIVERSIDAD DE LA LAGUNA

30/06/2017 15:10:02

ERNESTO PEREDA DE PABLO
UNIVERSIDAD DE LA LAGUNA

06/07/2017 13:51:28

3

Improvement on noise determination

3.1 Introduction

In the previous chapter we explained in detail the basis for how our method works and how it was implemented to create BUBBLY. This chapter deals with a very specific, but essential, part of the program which took an unexpected amount of time and effort to properly characterise: noise and error treatment.

We seek to detect very faint signals on data obtained from observations originally intending to analyse the dominant emission signal in galaxies. In order to detect these signals we need to get very close to the noise level, which makes it essential to properly assess its value.

As described in Section 1.4, our instrument uses a photon-counting system for detection with no instrumental noise, meaning that the uncertainty for each value should be the square root of the number of photons measured. This is actually not exactly the case, as we will see shortly.

For the first implementation of BUBBLY, a naive approach of a constant value measured from the dispersion of off-peak values was used. This is manifestly wrong because for Poisson statistics noise, as stated above, depends on the signal and should have yielded clearly erroneous results. This was not the case, and the first results obtained with this method were reasonably good expansion maps showing indeed the presence of bubbles, albeit many of them without detections in the very centre. The reason for this was found later to be that the reduction procedure COMPUTEVERYTHING (Daigle et al. (2006)) gave erroneous continuum estimations, which overestimated the continuum in the brighter zones significantly. This means that the signal in the brighter regions was excessively reduced, and this not only cancelled the mistake of

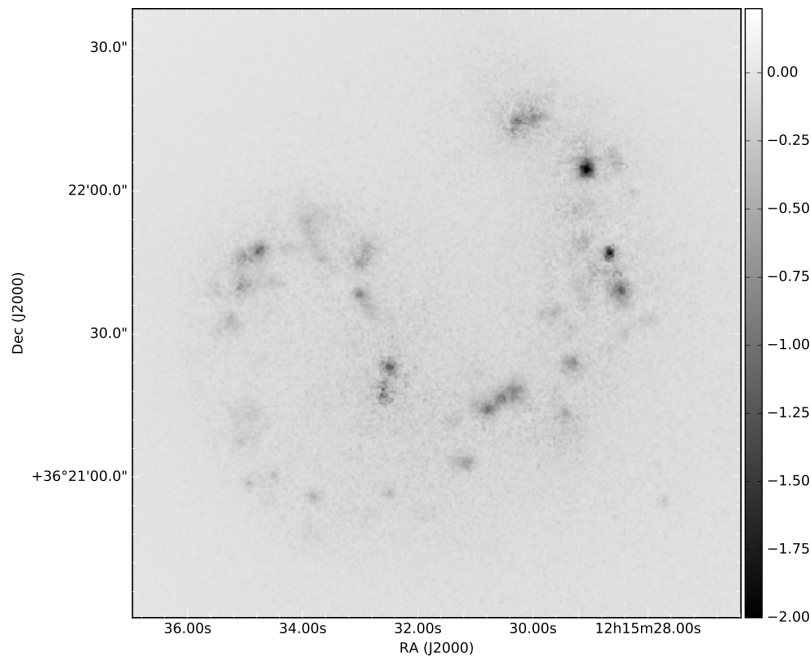


Figure 3.1: Map showing the continuum overestimation performed by COMPUTEVERYTHING for the Antennae galaxies, obtained by measuring the continuum on the processed cube. The fact that the values are negative means that it was indeed overestimated, and it is also apparent that it correlates with the region brightness.

assuming a constant noise level, but actually prevented us from detecting the central parts of the bubble, which lie in the brightest part of the HII region.

In Figure 3.1 we show the continuum overestimation performed by the reduction pipeline. The continuum overestimation was detected upon investigating why the centres of bubbles were not detected in general, and upon correcting this the inadequacy of the noise treatment became apparent in the output expansion maps. The new continuum estimation is built into BUBBLY, and consists simply of finding the lowest brightness point in the profile, a method that relies on the assumption that the profile will reach the continuum value at some spectral bin. At this point we tried to implement a new method for determining the noise levels, a task that proved far more complicated than initially assumed.

Este documento incorpora firma electrónica, y es copia auténtica de un documento electrónico archivado por la ULL según la Ley 39/2015.
Su autenticidad puede ser contrastada en la siguiente dirección <https://sede.ull.es/validacion/>

Identificador del documento: 973636 Código de verificación: QpwS3TwF

Firmado por: ARTEMI CAMPS FARIÑA UNIVERSIDAD DE LA LAGUNA	Fecha: 30/06/2017 14:40:15
JOHN E. BECKMAN UNIVERSIDAD DE LA LAGUNA	30/06/2017 15:07:38
JOAN FONT SERRA UNIVERSIDAD DE LA LAGUNA	30/06/2017 15:10:02
ERNESTO PEREDA DE PABLO UNIVERSIDAD DE LA LAGUNA	06/07/2017 13:51:28

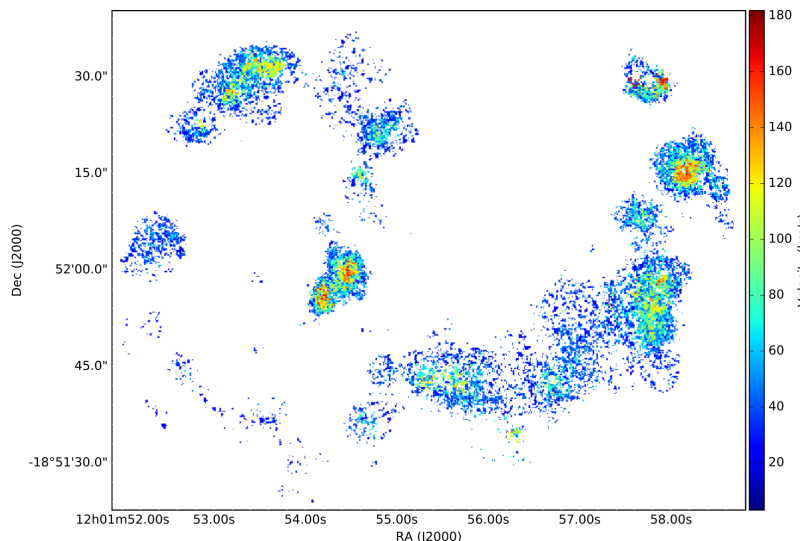


Figure 3.2: Expansion map resulting from using BUBBLY on the derotated cube before applying the reduction pipeline and imposing S:N \geq 1.

3.2 Validity of the theoretical noise value

As stated above, our instrument should follow a purely Poisson distribution given the nature of the detector. In practice, however, when imposing the value for noise as \sqrt{I} the results showed this to be an overestimation, with the real value being below this. This is so even for the raw data cube obtained immediately after derotation, as can be seen in Fig 3.2, where we show the expansion map for a minimum signal to noise (S:N) of 1. This value of the parameter means that anything with at least 1 detected photon is accepted as a valid signal, and yet the map is not nearly as noisy as it should be.

Upon examining the raw data cube we find that the values are not integers but floats, no doubt as a result of the derotation procedure.

Further proof is that in another galaxy, UGC 3995, the reduced data cube exhibits some spaxels clearly showing an emission peak, but with the maximum value below one count (see Fig. 3.3).

All of this suggests that the reduction procedures are lowering the fluctuation of the values intrinsic to the data, thus reducing the noise and making the

Este documento incorpora firma electrónica, y es copia auténtica de un documento electrónico archivado por la ULL según la Ley 39/2015.
Su autenticidad puede ser contrastada en la siguiente dirección <https://sede.ull.es/validacion/>

Identificador del documento: 973636 Código de verificación: QpwS3TwF

Firmado por: ARTEMI CAMPS FARIÑA UNIVERSIDAD DE LA LAGUNA	Fecha: 30/06/2017 14:40:15
JOHN E. BECKMAN UNIVERSIDAD DE LA LAGUNA	30/06/2017 15:07:38
JOAN FONT SERRA UNIVERSIDAD DE LA LAGUNA	30/06/2017 15:10:02
ERNESTO PEREDA DE PABLO UNIVERSIDAD DE LA LAGUNA	06/07/2017 13:51:28

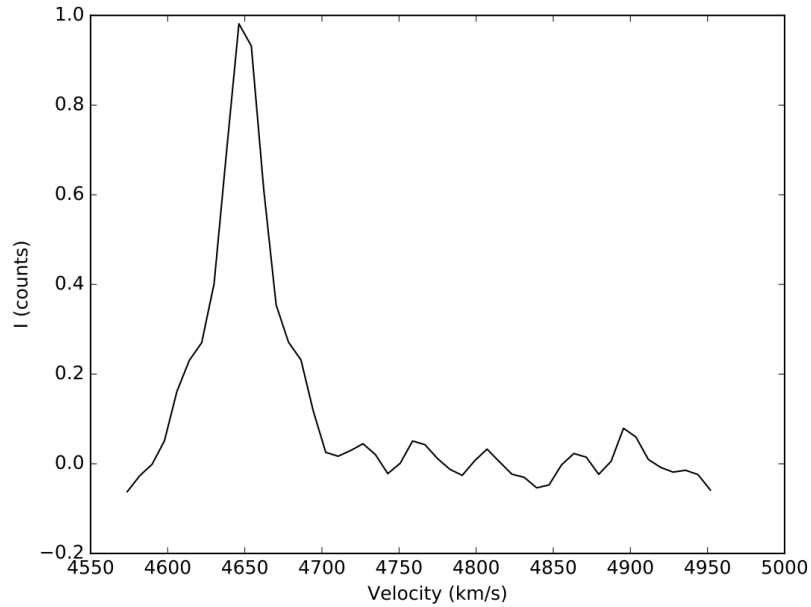


Figure 3.3: Emission profile for a spaxel in UGC 3995, where the digression from Poisson statistics can be appreciated. The profile shows an emission peak with a maximum value below 1 count and noisy fluctuations of order ~ 0.1 counts.

Este documento incorpora firma electrónica, y es copia auténtica de un documento electrónico archivado por la ULL según la Ley 39/2015.
Su autenticidad puede ser contrastada en la siguiente dirección <https://sede.ull.es/validacion/>

Identificador del documento: 973636 Código de verificación: QpwS3TwF

Firmado por: ARTEMI CAMPS FARIÑA UNIVERSIDAD DE LA LAGUNA	Fecha: 30/06/2017 14:40:15
JOHN E. BECKMAN UNIVERSIDAD DE LA LAGUNA	30/06/2017 15:07:38
JOAN FONT SERRA UNIVERSIDAD DE LA LAGUNA	30/06/2017 15:10:02
ERNESTO PEREDA DE PABLO UNIVERSIDAD DE LA LAGUNA	06/07/2017 13:51:28

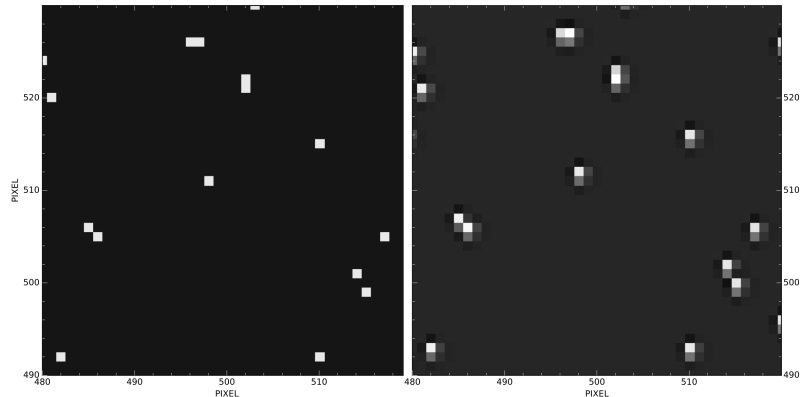


Figure 3.4: These two snapshots show the effect of the derotation software on the detections. On the left we show a region of an observed frame with sparse detections, and on the right the same region after the derotation has been performed. The detections on the right are no longer point-like, showing an extended structure.

assumed pure Poisson statistic to be wrong.

Upon close examination of the derotation process and its effect on the data we found that there is a "spread" effect on the individual detections upon rotating each observed frame to add it up with the rest. Our exposures are 10 seconds long and the sky rotates very slowly on this time-scale, so the rotated angle differential between frames is generally very small, meaning that the shift in position for the detections is comparable to the pixel scale in most cases.

The software uses an interpolation algorithm to produce the rotated frame that is to be added to the rest, and this is where the effect occurs: interpolation works best with continuous distributions while most of the detector area in our frames has zero signal with sparse individual detections and a zone of higher intensity where the scanning wavelength coincides with the H α emission maximum. The result is that the pixels adjacent to the detection have non-zero values owing to the nature of the algorithm. In Figure 3.4 we show this effect on isolated photon detections.

This phenomenon should not have a big impact on the final data, as the cumulative effect tends to cancel out when sweeping the spectral range several times. In fact, this process is similar to the DRIZZLE method used on Hubble Space Telescope (HST) images to improve their resolution, where exposures slightly offset from one another are combined by shrinking the pixel size and

Este documento incorpora firma electrónica, y es copia auténtica de un documento electrónico archivado por la ULL según la Ley 39/2015.
Su autenticidad puede ser contrastada en la siguiente dirección <https://sede.ull.es/validacion/>

Identificador del documento: 973636

Código de verificación: QpwS3TwF

Fecha: 30/06/2017 14:40:15

Firmado por: ARTEMI CAMPS FARIÑA
UNIVERSIDAD DE LA LAGUNA

JOHN E. BECKMAN
UNIVERSIDAD DE LA LAGUNA

JOAN FONT SERRA
UNIVERSIDAD DE LA LAGUNA

ERNESTO PEREDA DE PABLO
UNIVERSIDAD DE LA LAGUNA

30/06/2017 15:07:38

30/06/2017 15:10:02

06/07/2017 13:51:28

interpolating the final image. In principle the derotation process might improve the spatial resolution of the data compared to the reported seeing for the night of the observations, by aligning and interpolating the individual frames, but as we suffer from atmospheric turbulence unlike the HST we can only average out fluctuations on the time-scale of about 10 seconds.

In practice, the process equates to a kind of spatial smoothing, which reduces the noise in the data assuming a roughly continuous distribution, as is the case for galaxy objects. The reduction pipeline COMPUTEVERYTHING also includes spatial smoothing for this particular purpose and, therefore, the Poisson value for the noise becomes incorrect after applying the reduction procedures on the data.

The particular effect of spreading individual detections out and later combining them proved too difficult to characterize in an analytical manner, especially since it would vary depending on whether each detection is isolated or part of a larger structure. This is so because as stated above the validity of the interpolated values increases with a continuous distribution.

3.3 Estimation using the reduced data

The first attempts at solving this problem involved trying to derive an effective noise value from the properties of the reduced data themselves. One particular advantage of this approach is that there would then be no need to perform the entire data reduction again, which is a lengthy process. The derotation routine typically takes around 10 hours to finish and it can easily fail if there are not two or more bright stars available, therefore we typically we need to run it several times per cube.

Measuring the noise on the data is, while less formally rigorous, also more robust, as we don't need to worry about the effects of the various processes that influence its value, only the final result. In the end, however, none of the attempts yielded satisfactory results in terms of the resulting expansion map, so we had to pursue other methods. We present here a brief overview of some of the methods that were attempted and their results.

3.3.1 Use total flux of the peak

A first attempt to improve the signal was to not use highest value of the intensity as a discriminator, but instead the sum of all the flux contained in the line. The theoretical justification is straightforward, as an emission line's true signal is indeed all the flux contained within the line, but at the same time this method is not actually a solution to the problem we have on the noise statistics.

Este documento incorpora firma electrónica, y es copia auténtica de un documento electrónico archivado por la ULL según la Ley 39/2015.
Su autenticidad puede ser contrastada en la siguiente dirección <https://sede.ull.es/validacion/>

Identificador del documento: 973636 Código de verificación: QpwS3TwF

Firmado por: ARTEMI CAMPS FARIÑA UNIVERSIDAD DE LA LAGUNA	Fecha: 30/06/2017 14:40:15
JOHN E. BECKMAN UNIVERSIDAD DE LA LAGUNA	30/06/2017 15:07:38
JOAN FONT SERRA UNIVERSIDAD DE LA LAGUNA	30/06/2017 15:10:02
ERNESTO PEREDA DE PABLO UNIVERSIDAD DE LA LAGUNA	06/07/2017 13:51:28

Since the problem we have when using the Poisson statistic for the noise value is that low intensity peaks are weeded out in excess, raising the overall emission per peak might be a sufficient solution to produce useful expansion maps. On the other hand, we are completely ignoring the fact that our statistics have been modified and the square root is no longer the correct representation of the noise.

In Fig. 3.5 a) we show the best expansion map obtained using this method. We see that the detection is definitely improved, but the result still has significant noise as well as patchy superbubbles.

3.3.2 Continuum dispersion

Another idea was to use the spatial dispersion of the calculated continuum to estimate a noise level associated with each spectra. The continuum for each spatial point is calculated as constant, so we use the standard deviation of the values of the continuum in a 3x3 box centred on each point as a measure of the spectral noise. The basic assumption is that the true continuum should be fairly smooth within such a short spectral range, so the variation in values within a small region should be dominated by the spectral noise.

This method, like some of the following ones, has the problem that it does not take into account that brighter peaks should have a larger noise value, but since we are the noise value affects mostly the fainter, lower signal peaks we might expect this method to still be useful.

As can be seen in Fig 3.5 b), we obtain an expansion map that is worse than the previous one, with a higher ratio of noisy detections.

3.3.3 Smoothed spectrum subtraction

The true distribution for the noise in the spectra would be obtained if we could subtract the true distribution of the emission from the source. We cannot actually obtain the true emission profile, but we can try to approximate it by smoothing the spectra, which reduces the noise, and subtracting the result from the original spectrum. This should leave a predominantly stochastic distribution of values characteristic of the noise in our data.

This method has some problems, smoothing reduces the high frequency variations in the data, which are not only produced by noise. In practice, an emission line will have its width artificially increased by the smoothing, which can produce artefacts when subtracting it from the spectrum. Because of this we need to use a small kernel for the smoothing algorithm, which in turn means we are not completely removing the noisy fluctuations, leading to

Este documento incorpora firma electrónica, y es copia auténtica de un documento electrónico archivado por la ULL según la Ley 39/2015.
Su autenticidad puede ser contrastada en la siguiente dirección <https://sede.ull.es/validacion/>

Identificador del documento: 973636

Código de verificación: QpwS3TwF

Fecha: 30/06/2017 14:40:15

Firmado por: ARTEMI CAMPS FARIÑA
UNIVERSIDAD DE LA LAGUNA

JOHN E. BECKMAN
UNIVERSIDAD DE LA LAGUNA

JOAN FONT SERRA
UNIVERSIDAD DE LA LAGUNA

ERNESTO PEREDA DE PABLO
UNIVERSIDAD DE LA LAGUNA

30/06/2017 15:07:38

30/06/2017 15:10:02

06/07/2017 13:51:28

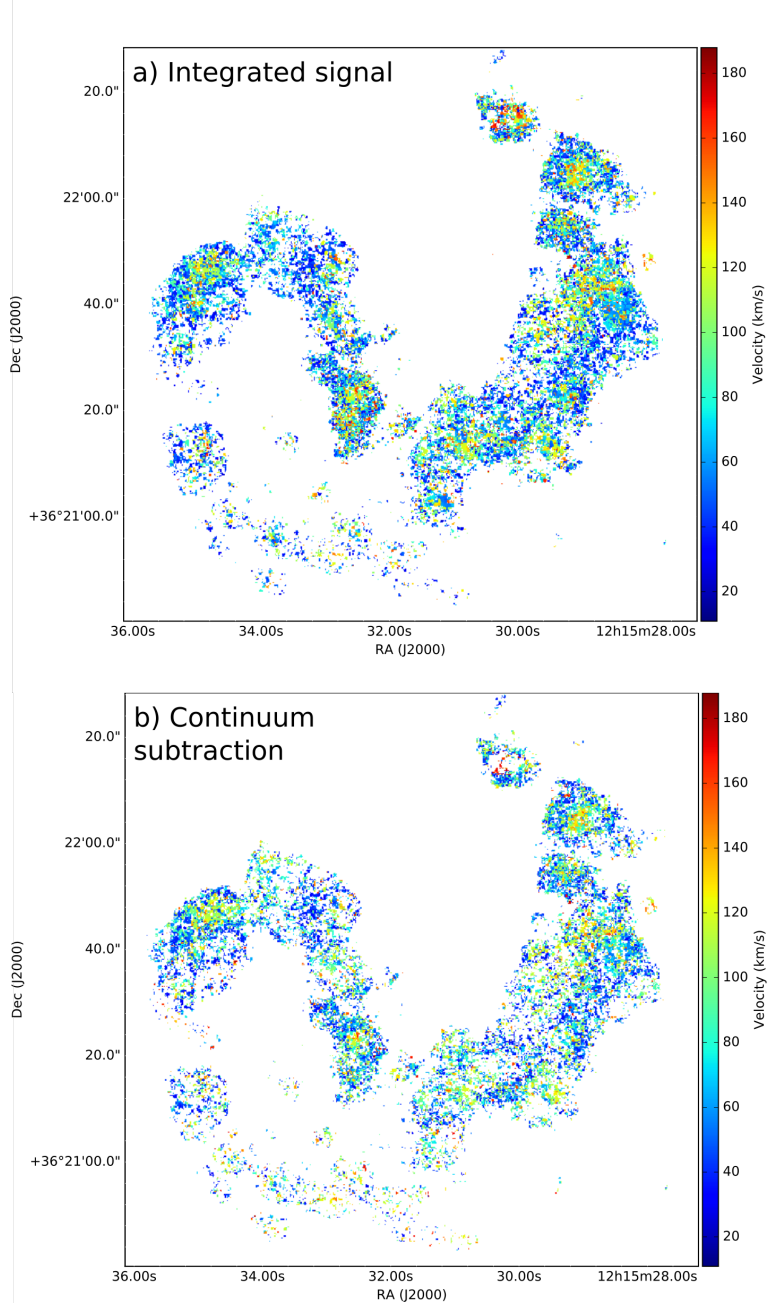


Figure 3.5: Expansion maps obtained by two different methods to estimate noise. a) uses Poisson statistics for the entire flux of a peak instead of each element, while b) estimates the noise from the standard deviation of the continuum.

Este documento incorpora firma electrónica, y es copia auténtica de un documento electrónico archivado por la ULL según la Ley 39/2015.
Su autenticidad puede ser contrastada en la siguiente dirección <https://sede.ull.es/validacion/>

Identificador del documento: 973636 Código de verificación: QpwS3TwF

Firmado por: ARTEMI CAMPS FARÍÑA UNIVERSIDAD DE LA LAGUNA	Fecha: 30/06/2017 14:40:15
JOHN E. BECKMAN UNIVERSIDAD DE LA LAGUNA	30/06/2017 15:07:38
JOAN FONT SERRA UNIVERSIDAD DE LA LAGUNA	30/06/2017 15:10:02
ERNESTO PEREDA DE PABLO UNIVERSIDAD DE LA LAGUNA	06/07/2017 13:51:28

an underestimation of the value for the noise.

After a few trials, we settled for a kernel of width 1 pixel in the spectral direction, and used the standard deviation of the residual as the noise value for the spectrum. In Fig.3.6 a) we show the results, which show a remarkable improvement on noise-dominated detections, but the price is that we lose the detections on the centre of the bubbles, which was the original problem.

3.3.4 Local smoothed spectrum subtraction

The previous method managed to solve half the problem, as it worked well for low-luminosity regions, so we tried to improve it so that there was not a single noise value for the profile, but one that depended on the brightness of the spectral point.

The implementation is similar to the previous case, but we no longer calculate the standard deviation with all the remnant spectrum, but instead we produce a vector where the value for each bin is the standard deviation of it and its surrounding bins.

The resulting expansion map is shown in Fig. 3.6 b), where we see that though the detection in the centres of the brightest regions does improve a little, we again introduce noise in the lower brightness regions.

3.3.5 Spline fitting

Smoothing the profile has a limitation in that the smoothing kernel cannot not be too large lest we introduce artificial variations in the subtracted profile. A better way to implement this idea would be to fit a function which correctly describes the distribution to the data. In our case the best option would be a Gaussian function, but this assumes that there are no multiple peaks, which in practice means that any secondary peaks would end up in the residual and assumed to be noise when computing the value. Lumping the very secondary peaks we are interested in together with the noise we are trying to determine incorrectly increases the noise value where precision is most needed.

An intermediate option is to use smoothed splines to fit to the data, which do not assume a given distribution for the data nor artificially widen the features. A well-chosen spline should provide a good guess for the true distribution of the data.

The critical parameter for this method is the smoothing value of the spline, which unfortunately cannot be chosen as a constant parameter, each individual spectrum having an optimal value. The determination of this value is non-trivial, with several schemes available. We used an implementation of the

Este documento incorpora firma electrónica, y es copia auténtica de un documento electrónico archivado por la ULL según la Ley 39/2015.
Su autenticidad puede ser contrastada en la siguiente dirección <https://sede.ull.es/validacion/>

Identificador del documento: 973636 Código de verificación: QpwS3TwF

Firmado por: ARTEMI CAMPS FARIÑA UNIVERSIDAD DE LA LAGUNA	Fecha: 30/06/2017 14:40:15
JOHN E. BECKMAN UNIVERSIDAD DE LA LAGUNA	30/06/2017 15:07:38
JOAN FONT SERRA UNIVERSIDAD DE LA LAGUNA	30/06/2017 15:10:02
ERNESTO PEREDA DE PABLO UNIVERSIDAD DE LA LAGUNA	06/07/2017 13:51:28

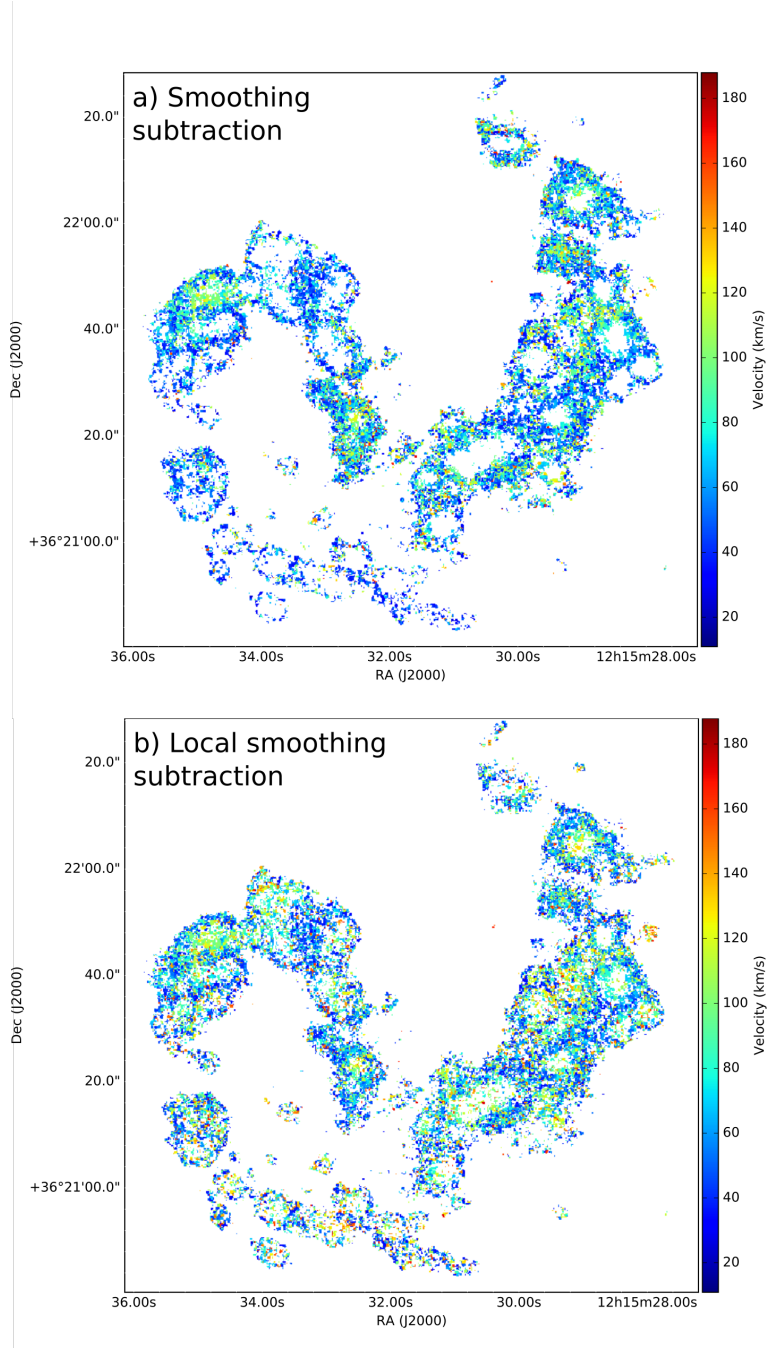


Figure 3.6: Expansion maps obtained by two different methods to estimate noise based on subtracting a smoothed spectrum from the original. a) obtains a single standard deviation of the remnant, while b) calculates a vector of standard deviations using the adjacent values only.

Este documento incorpora firma electrónica, y es copia auténtica de un documento electrónico archivado por la ULL según la Ley 39/2015.
Su autenticidad puede ser contrastada en la siguiente dirección <https://sede.ull.es/validacion/>

Identificador del documento: 973636

Código de verificación: QpwS3TwF

Firmado por: ARTEMI CAMPS FARÍÑA
UNIVERSIDAD DE LA LAGUNA

Fecha: 30/06/2017 14:40:15

JOHN E. BECKMAN
UNIVERSIDAD DE LA LAGUNA

30/06/2017 15:07:38

JOAN FONT SERRA
UNIVERSIDAD DE LA LAGUNA

30/06/2017 15:10:02

ERNESTO PEREDA DE PABLO
UNIVERSIDAD DE LA LAGUNA

06/07/2017 13:51:28

Generalized Cross Validation method by (Garcia (2010)).

The result is shown in Fig. 3.7 a), we see an improvement on the detection on the centres without introducing too much noise, the results sit between the previous two methods, but are still not too good.

3.3.6 Spatial smoothing subtraction

The previous methods work on the spectral dimension, attempting to obtain an approximation of the spectral profile. Another approach is to work on the spatial dimension instead, by assuming that the emission profile of close points is similar. In this manner we perform a spatial smoothing of the cube and subtract it from the original, and use the remnant to obtain values for the noise.

The resulting expansion map is shown in Fig. 3.7 b), it shows an increased level of noise in some of the brighter regions, while in others it has no detections on the centre, in general this method performs worse than the spectrum-based methods.

3.4 Noise estimation using simulated data and mock observations

The final and successful attempt at characterizing the noise statistics for our data was to use a model galaxy to perform a mock observation and apply the reduction procedure on it. By subtracting the resulting data cube from the model we can perform statistics on the typical deviation of the observation from the original. This method has the decisive advantage of having no previous assumptions on the effects of the reduction on the data, instead we directly measure these directly by comparing the result to the "true" source, which is impossible with real data.

3.4.1 Mock observation

The first thing we need is a model galaxy to produce the mock observation. Rather than constructing a galaxy from zero we preferred to preserve the kinematic structure present in our observed galaxy and thus used a heavily smoothed cube of the Antennae galaxies as the model data cube. We also added four artificial stars near the corners of the cube to ensure an easy and reliable derotation.

In order to simulate the detection process we will assume that the light emission follows a Poisson distribution:

Este documento incorpora firma electrónica, y es copia auténtica de un documento electrónico archivado por la ULL según la Ley 39/2015.
Su autenticidad puede ser contrastada en la siguiente dirección <https://sede.ull.es/validacion/>

Identificador del documento: 973636 Código de verificación: QpwS3TwF

Firmado por: ARTEMI CAMPS FARIÑA UNIVERSIDAD DE LA LAGUNA	Fecha: 30/06/2017 14:40:15
JOHN E. BECKMAN UNIVERSIDAD DE LA LAGUNA	30/06/2017 15:07:38
JOAN FONT SERRA UNIVERSIDAD DE LA LAGUNA	30/06/2017 15:10:02
ERNESTO PEREDA DE PABLO UNIVERSIDAD DE LA LAGUNA	06/07/2017 13:51:28

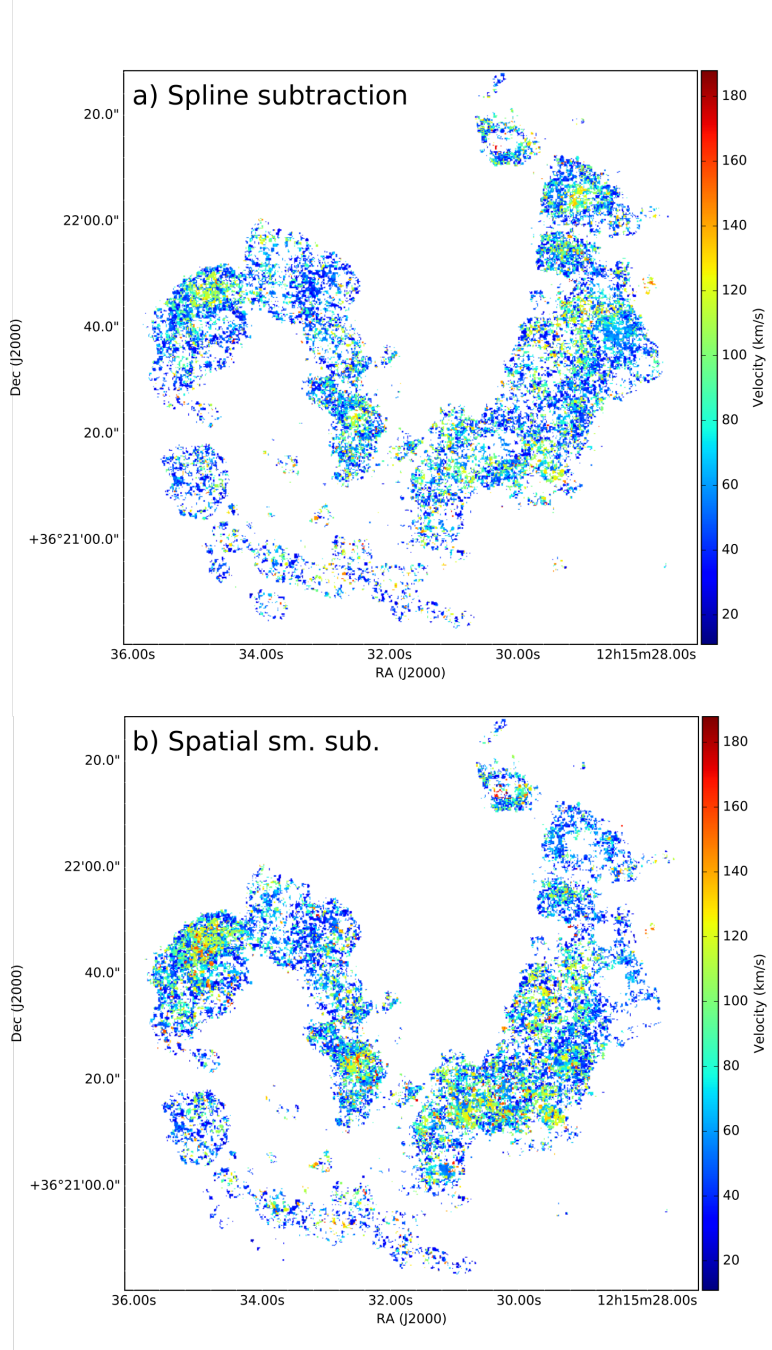


Figure 3.7: Expansion maps obtained by two different methods to estimate noise. a) fits a spline to the spectral profile to obtain the noise, b) performs a spatial smoothing instead and subtracts it from the cube to obtain the noise.

Este documento incorpora firma electrónica, y es copia auténtica de un documento electrónico archivado por la ULL según la Ley 39/2015.
Su autenticidad puede ser contrastada en la siguiente dirección <https://sede.ull.es/validacion/>

Identificador del documento: 973636

Código de verificación: QpwS3TwF

Firmado por: ARTEMI CAMPS FARÍÑA
UNIVERSIDAD DE LA LAGUNA

Fecha: 30/06/2017 14:40:15

JOHN E. BECKMAN
UNIVERSIDAD DE LA LAGUNA

30/06/2017 15:07:38

JOAN FONT SERRA
UNIVERSIDAD DE LA LAGUNA

30/06/2017 15:10:02

ERNESTO PEREDA DE PABLO
UNIVERSIDAD DE LA LAGUNA

06/07/2017 13:51:28

$$P(k) = \frac{\gamma^k e^{-\gamma}}{k!} \quad (3.1)$$

This equation represents the probability of observing k photons in an interval of time, where γ is the average number of photons emitted in the same interval. The units for our mock galaxy are the number of photons collected within the observing time. Each (X,Y,v) point is observed once per cycle, so the average number of photons observed in one frame can be obtained by dividing the intensity by the number of cycles for each position and wavelength.

The observation is produced cycling the channel range a number of times (the number of cycles), the channels are swept in a zig-zag manner as in the observations, if the cycle number is even we proceed in normal order, and reverse order for odd cycles.

The process for producing each frame is as follows:

- Increase the total angle rotated by one step.
- Produce a rotated copy of the model galaxy cube.
- Obtain the wavelength corresponding to each X,Y position.
- Read the γ associated to each X, Y, wavelength from the model galaxy.
- Produce a random number of photons for each pixel using the Poisson distribution with the aforementioned γ array.
- Save the array to a file.

We use a constant step rotation of the galaxy between frames, its value estimated from the values TWIRL calculated during the actual derotation process. In real observations the rotation speed changes throughout the observation, but this is typically a small variation unless we are observing close to the zenith (owing to the WHT having an altazimuth mount). Furthermore, the effects we are concerned with arise from interpolating between pixels, so the precise speed of rotation is not critical.

The next step is to obtain the wavelength map for the channel in question. As explained in section 1.4 when a Fabry-Pérot instrument sweeps the channel range each frame does not measure the same wavelength throughout the spatial range. In order to simulate this we used the calibration files to produce a wavelength cube containing the spectral information for each channel. We use this to look up the correct intensity value from the model galaxy cube which is then used to randomly generate a number of photons.

Este documento incorpora firma electrónica, y es copia auténtica de un documento electrónico archivado por la ULL según la Ley 39/2015.
Su autenticidad puede ser contrastada en la siguiente dirección <https://sede.ull.es/validacion/>

Identificador del documento: 973636 Código de verificación: QpwS3TwF

Firmado por: ARTEMI CAMPS FARIÑA UNIVERSIDAD DE LA LAGUNA	Fecha: 30/06/2017 14:40:15
JOHN E. BECKMAN UNIVERSIDAD DE LA LAGUNA	30/06/2017 15:07:38
JOAN FONT SERRA UNIVERSIDAD DE LA LAGUNA	30/06/2017 15:10:02
ERNESTO PEREDA DE PABLO UNIVERSIDAD DE LA LAGUNA	06/07/2017 13:51:28

In this manner we can produce the equivalent of an actual observation using our model galaxy.

The last step is to actually perform the reduction of this data to produce an "observed" data cube to compare to the model galaxy.

We present three relevant cases of reduction processing and their noise statistics.

3.4.2 Noise statistics

Now that we have the mock observation we need to calculate the behaviour of signal to noise ratio. We will assume that the noise value can be characterised as a function of the signal, which will allow us to find a relation to use in BUBBLY to implement the S:N discrimination of the detected peaks.

To this end, we make plots of the relative intensity versus intensity, I_{obs}/I_{mod} vs I_{obs} , on which we will calculate the percentiles representing the standard deviations of the data for each intensity. The width of the distribution can then be transformed into a relative error, we will fit a function to this data so that we can obtain the desired intensity-noise relation.

The first case we will analyse is the output of the derotation process, which should have the lowest level of noise filtering and is useful for the characterization of the instrumental response of GH α FaS. This analysis should also be of use to any future studies which require a precise determination of noise statistics.

In Figure 3.8 we show the intensity ratio between the points in the derotated cube and the original model versus the measured intensity. We also plot the quantiles for the various sigma levels. The area between the lines of each quantile can be used to determine the uncertainty in the data as a function of intensity. We see that in this case the low-intensity points have a very large dispersion and an odd behaviour close to zero. At high count levels we also see a deviation from the expected mean value for the ratio of 1, which implies that somehow the brightest pixels intensity is being enhanced.

Next we have the output cube from the reducing program COMPUTEVERYTHING, which is the standard reduction used for our data. Also, given that most of the cubes we have available are legacy data from other projects, this is generally the format in which they are saved. Obtaining a reliable noise statistic for these would then save us the time to perform once again the derotation on the raw data from the GH α FaS archive.

The intensity ratio distribution for this case can be seen in Figure 3.9, where we see a marked improvement with respect to the previous case, with a tighter distribution that implies lower noise values. We still have many points at low

Este documento incorpora firma electrónica, y es copia auténtica de un documento electrónico archivado por la ULL según la Ley 39/2015.
Su autenticidad puede ser contrastada en la siguiente dirección <https://sede.ull.es/validacion/>

Identificador del documento: 973636 Código de verificación: QpwS3TwF

Firmado por: ARTEMI CAMPS FARIÑA UNIVERSIDAD DE LA LAGUNA	Fecha: 30/06/2017 14:40:15
JOHN E. BECKMAN UNIVERSIDAD DE LA LAGUNA	30/06/2017 15:07:38
JOAN FONT SERRA UNIVERSIDAD DE LA LAGUNA	30/06/2017 15:10:02
ERNESTO PEREDA DE PABLO UNIVERSIDAD DE LA LAGUNA	06/07/2017 13:51:28

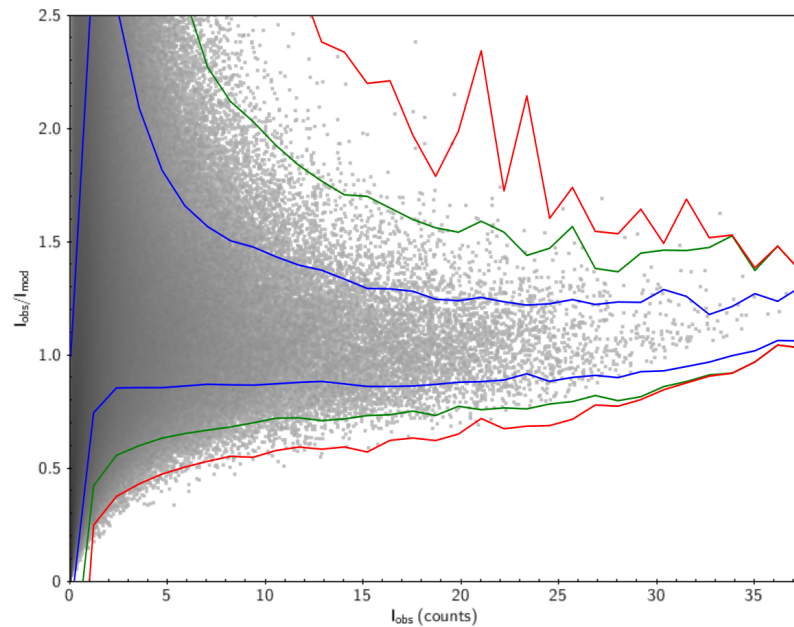


Figure 3.8: Relative intensity plot for the derotated cube. We show the ratio between the intensity measured in the derotated cube and the model cube with respect to the measured intensity. The coloured lines correspond to the different sigma values, blue for 1σ (68%), green for 2σ (95%) and red for 3σ (99%). The width between the low and high lines defines the associated relative noise for each intensity value.

Este documento incorpora firma electrónica, y es copia auténtica de un documento electrónico archivado por la ULL según la Ley 39/2015.
Su autenticidad puede ser contrastada en la siguiente dirección <https://sede.ull.es/validacion/>

Identificador del documento: 973636

Código de verificación: QpwS3TwF

Firmado por: ARTEMI CAMPS FARIÑA
UNIVERSIDAD DE LA LAGUNA

Fecha: 30/06/2017 14:40:15

JOHN E. BECKMAN
UNIVERSIDAD DE LA LAGUNA

30/06/2017 15:07:38

JOAN FONT SERRA
UNIVERSIDAD DE LA LAGUNA

30/06/2017 15:10:02

ERNESTO PEREDA DE PABLO
UNIVERSIDAD DE LA LAGUNA

06/07/2017 13:51:28

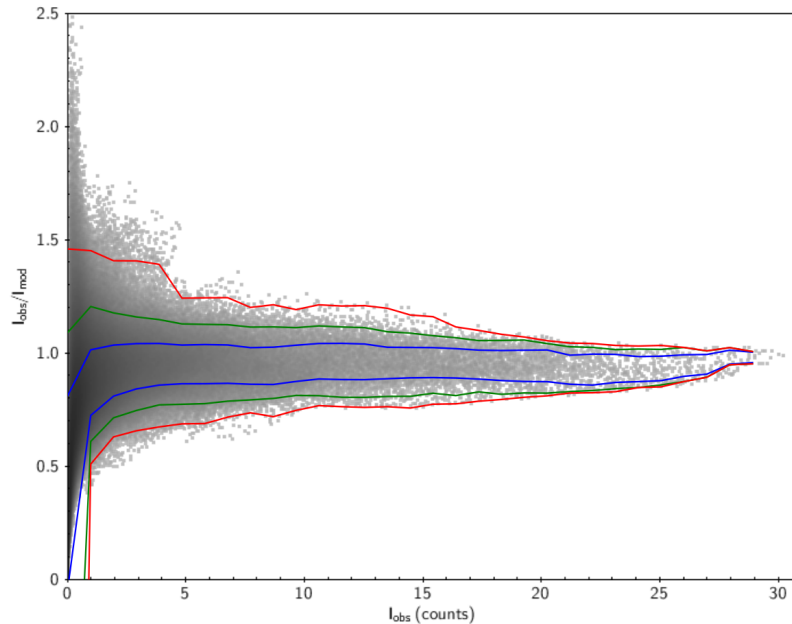


Figure 3.9: Relative intensity plot for the fully reduced cube. We show the ratio between the intensity measured in the derotated cube and the model cube with respect to the measured intensity. The coloured lines correspond to the different sigma values, blue for 1σ (68%), green for 2σ (95%) and red for 3σ (99%). The width between the low and high lines defines the associated relative noise for each intensity value.

intensity that do not behave correctly with many going to negative values, a fact that can be appreciated by the dip in the quantiles close to zero.

The last case is a simpler treatment of the data obtained by simply smoothing the derotated data cube with a Gaussian kernel of size 2 in the spatial direction. The results show that this method yields in general the best compromise between noise removal and preservation of weak real components. This fact can be appreciated in Figure 3.10, where we see a much better behaviour of the data at low intensity compared to the cube reduced by the usual procedure. We also don't have negative values which is also a good sign.

For this case we can also derive a theoretical treatment of the noise values if we assume that the effect of the derotation is marginal with respect to the Gaussian smoothing.

Este documento incorpora firma electrónica, y es copia auténtica de un documento electrónico archivado por la ULL según la Ley 39/2015.
Su autenticidad puede ser contrastada en la siguiente dirección <https://sede.ull.es/validacion/>

Identificador del documento: 973636

Código de verificación: QpwS3TwF

Firmado por: ARTEMI CAMPS FARIÑA
UNIVERSIDAD DE LA LAGUNA

Fecha: 30/06/2017 14:40:15

JOHN E. BECKMAN
UNIVERSIDAD DE LA LAGUNA

30/06/2017 15:07:38

JOAN FONT SERRA
UNIVERSIDAD DE LA LAGUNA

30/06/2017 15:10:02

ERNESTO PEREDA DE PABLO
UNIVERSIDAD DE LA LAGUNA

06/07/2017 13:51:28

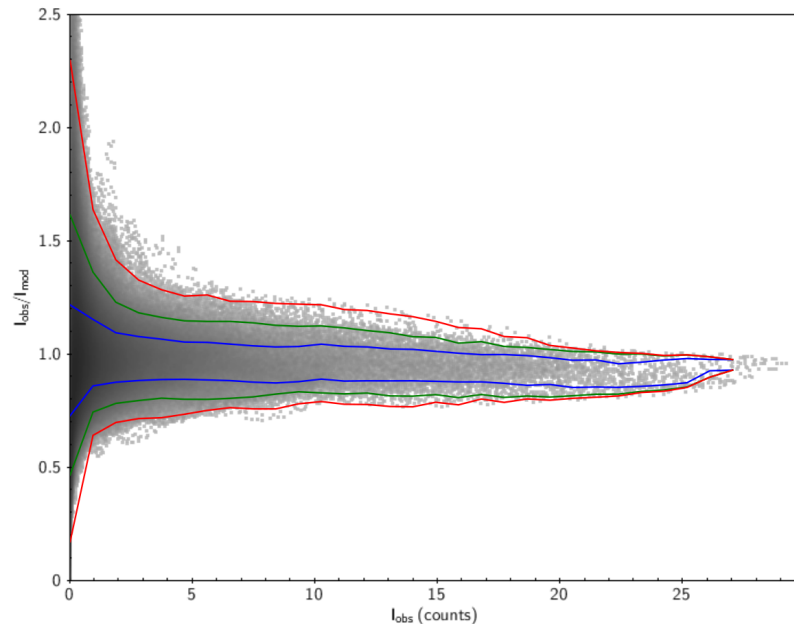


Figure 3.10: Relative intensity plot for the derotated cube after applying Gaussian smoothing in the spatial direction. We show the ratio between the intensity measured in the derotated cube and the model cube with respect to the measured intensity. The coloured lines correspond to the different sigma values, blue for 1σ (68%), green for 2σ (95%) and red for 3σ (99%). The width between the low and high lines defines the associated relative noise for each intensity value.

Este documento incorpora firma electrónica, y es copia auténtica de un documento electrónico archivado por la ULL según la Ley 39/2015.
Su autenticidad puede ser contrastada en la siguiente dirección <https://sede.ull.es/validacion/>

Identificador del documento: 973636

Código de verificación: QpwS3TwF

Firmado por: ARTEMI CAMPS FARIÑA
UNIVERSIDAD DE LA LAGUNA

Fecha: 30/06/2017 14:40:15

JOHN E. BECKMAN
UNIVERSIDAD DE LA LAGUNA

30/06/2017 15:07:38

JOAN FONT SERRA
UNIVERSIDAD DE LA LAGUNA

30/06/2017 15:10:02

ERNESTO PEREDA DE PABLO
UNIVERSIDAD DE LA LAGUNA

06/07/2017 13:51:28

Gaussian smoothing is essentially a weighted mean, the operation consists of a sum of a number of intensities weighted according to the separation between pixels:

$$I'(x, y) = \sum_{i,j} g_{ij} I(x_i, y_j) \quad (3.2)$$

where g_{ij} are the corresponding values of the Gaussian kernel for each position around (x, y) . In order to calculate how the operation affects the error we will assume that each intensity value $I(x_i, y_j)$ is an independent variable and perform the error propagation according to the general formula:

$$\sigma_f = \sqrt{\sum_k \left(\frac{\delta f}{\delta x_k} \right)^2 \sigma_{x_k}^2} \quad (3.3)$$

where x_k are the independent variables of the function $f(x_k)$. In our case then:

$$\sigma_{I(x,y)} = \sqrt{\sum_k \left(\frac{\delta I(x, y)}{\delta I_k} \right)^2 \sigma_{I_k}^2} \Rightarrow \sigma_{I(x,y)} = \sqrt{\sum_k g_k^2 I_k} \quad (3.4)$$

with k sweeping over all (i, j) values. Now if we take the approximation that the intensity is fairly constant we can obtain a general value depending only on the kernel used:

$$I_k \simeq I(x, y) \Rightarrow \sigma_{I(x,y)} = \sqrt{I(x, y)} \sqrt{\sum_k g_k^2} \quad (3.5)$$

Therefore the uncertainty for each point can be approximated by the Poisson value multiplied by a factor consisting of the quadratic sum of the Gaussian kernel. We have tested this method and it yields the same results as the uncertainty relation obtained from the simulated observation. This method is easier to use and implement as it only needs to know the smoothing applied to obtain the correct noise values, so it is the one used in the data.

Este documento incorpora firma electrónica, y es copia auténtica de un documento electrónico archivado por la ULL según la Ley 39/2015.
Su autenticidad puede ser contrastada en la siguiente dirección <https://sede.ull.es/validacion/>

Identificador del documento: 973636 Código de verificación: QpwS3TwF

Firmado por: ARTEMI CAMPS FARIÑA UNIVERSIDAD DE LA LAGUNA	Fecha: 30/06/2017 14:40:15
JOHN E. BECKMAN UNIVERSIDAD DE LA LAGUNA	30/06/2017 15:07:38
JOAN FONT SERRA UNIVERSIDAD DE LA LAGUNA	30/06/2017 15:10:02
ERNESTO PEREDA DE PABLO UNIVERSIDAD DE LA LAGUNA	06/07/2017 13:51:28

4

Three supernova shells around an M33 star cluster

4.1 Introduction

The interaction of winds and supernova remnants with the surrounding interstellar medium is a phenomenon which cannot be understood from examples in isolated environments; the mechanisms that affect it take place on a broad range of spatial and temporal scales. Galaxy formation models without strong stellar feedback convert their gas into stars too rapidly by two orders of magnitude (e.g. Hopkins et al. (2011)) and predict that star formation in galaxies would have finished when the universe had only 10% of its present age. They also cannot explain the dispersion of heavy elements into the intergalactic medium (e.g. Wiersma et al. (2010)). Approximations to the effects of supernovae on the interstellar medium are now a feature of simulation models (e.g. Marinacci et al. (2014)) which, as well as making ad hoc approximations to ensure that the feedback is sufficiently strong to reproduce the properties of observed galaxies, have traditionally assumed as simplifying limitations that the surrounding ISM is homogeneous, and supernovae occur singly (Chevalier (1974), Thornton et al. (1998)). These limitations have been gradually relaxed, as computing power has increased.

It is known that the real ISM is highly inhomogeneous (Osterbrock & Flather (1959), McKee & Ostriker (1977), Giammanco et al. (2004)) and this has been used in a recent set of models by Martizzi et al. (2015). The effect of multiple supernovae occurring within a stellar cluster was modelled by Kim et al. (2011) and more recently by Hennebelle & Ifrig (2014). Martizzi et al.

(2015) produced models with both of these features. The aim of all the models is to reproduce the balance between star formation enhancement and quenching due to the effects of the supernovae on their surroundings, and thereby to predict the macroscopic properties of galaxies. As is frequent in all issues related to star formation, particularly massive star formation, a key difficulty for modellers is the lack of observational constraints; in this chapter we report observations which take a step forward in improving them.

The results presented here are from a high resolution kinematic survey of the local group galaxy M33 using its ionized hydrogen emission in H α . M33 is preferred to the Galaxy because its known distance gives reliable values for the physical parameters measured, while it is sufficiently close to yield good linear resolution. More results from the wider scale study are presented in Chapter 5.

4.2 Observations

We observed a field on the southern arm of M33 centred on the HII region studied in this chapter during on 31st October 2014 using the Galaxy H α Fabry-Perot System (see Chapter 1), and followed this up using the Intermediate dispersion Spectrograph and Imaging System (ISIS) on 25th December 2014. The region in question is listed as BCLMP17-d, the central part of the BCLMP17 complex, in the 1974 Boulesteix HII region catalogue (Boulesteix et al. (1974),Hodge et al. (2002)).

ISIS is a high-efficiency, double-armed, medium-resolution (8-120 Å/mm) spectrograph,at the Cassegrain focus of the WHT, capable of providing up to 4' slit length and 22" slit width. We observed the region with a 10" wide slit using the red arm R1200R grating centred at 6800 Å. This allowed us to observe simultaneously the H α , SII and NII lines with a spectral resolution of ~12 km/s. We used a slit width of 10" to encompass in a single observation the central part of the region where we detected the bubbles with GHoFaS.

We reduced the spectrum using *IRAF*. The ISIS data was used to compute line flux ratios of very close emission lines, which removed the necessity for flux calibration of the spectra.

4.3 Expansion maps

We applied BUBBLY to the data cube with the default configuration in the BUBBLY parameter file and a minimum S:N ratio of 5 to detect the expansion components. In Fig. 4.1 we show the line profile of H α emission which indicates

Este documento incorpora firma electrónica, y es copia auténtica de un documento electrónico archivado por la ULL según la Ley 39/2015.
Su autenticidad puede ser contrastada en la siguiente dirección <https://sede.ull.es/validacion/>

Identificador del documento: 973636 Código de verificación: QpwS3TwF

Firmado por: ARTEMI CAMPS FARIÑA UNIVERSIDAD DE LA LAGUNA	Fecha: 30/06/2017 14:40:15
JOHN E. BECKMAN UNIVERSIDAD DE LA LAGUNA	30/06/2017 15:07:38
JOAN FONT SERRA UNIVERSIDAD DE LA LAGUNA	30/06/2017 15:10:02
ERNESTO PEREDA DE PABLO UNIVERSIDAD DE LA LAGUNA	06/07/2017 13:51:28

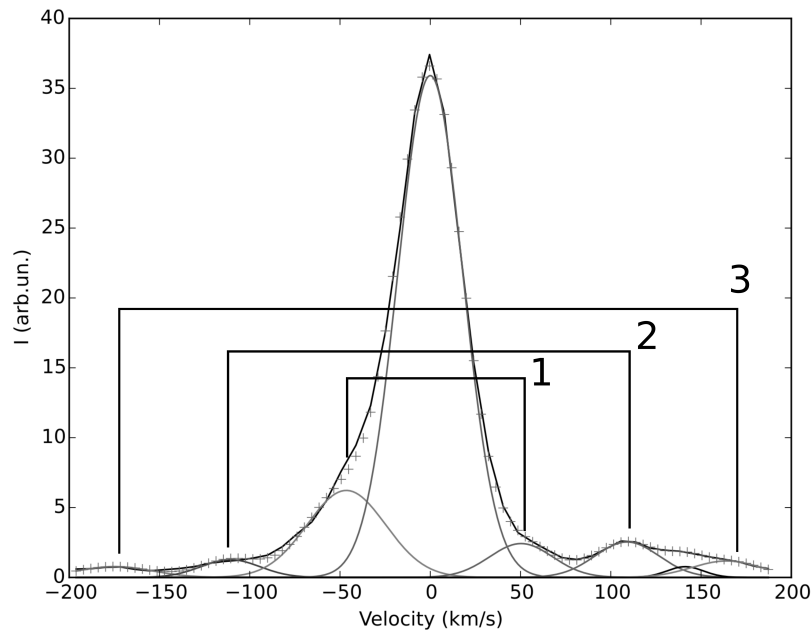


Figure 4.1: Example of a spaxel from the GHaFaS data cube which shows three pairs of symmetrically placed secondary peaks, indicating expansion. The detection and fitting was performed automatically using BUBBLY.

the presence of the three shells, with a central main peak and three pairs of secondary components. This profile comes from only a single resolved element of the velocity map.

Figure 4.2 was produced by mapping all the pixels where a given pair of peaks was detected, which displays the projected extent of the shell; the process was repeated for each of the three shells. We can see that the smallest shell has the most rapid expansion velocity, and the largest shell has the slowest, as expected for shells originating in the centre and doing work on the surrounding interstellar medium during their expansion.

Este documento incorpora firma electrónica, y es copia auténtica de un documento electrónico archivado por la ULL según la Ley 39/2015.
Su autenticidad puede ser contrastada en la siguiente dirección <https://sede.ull.es/validacion/>

Identificador del documento: 973636

Código de verificación: QpwS3TwF

Firmado por: ARTEMI CAMPS FARÍÑA
UNIVERSIDAD DE LA LAGUNA

Fecha: 30/06/2017 14:40:15

JOHN E. BECKMAN
UNIVERSIDAD DE LA LAGUNA

30/06/2017 15:07:38

JOAN FONT SERRA
UNIVERSIDAD DE LA LAGUNA

30/06/2017 15:10:02

ERNESTO PEREDA DE PABLO
UNIVERSIDAD DE LA LAGUNA

06/07/2017 13:51:28

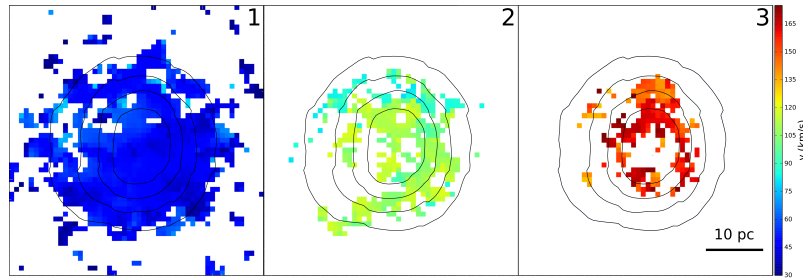


Figure 4.2: Expansion maps of the three detected bubbles, which show the detected expansion velocity in each pixel, all in the same velocity scale. Overlaid are contours of the region's H α emission, it can be seen that the bubbles are roughly concentric with each other and the region

4.4 Properties of the bubbles

We performed the calculation of the physical properties of the bubbles in the manner explained in Chapter 2, other than for two of the parameters, the width of the shell and the age. In this case, the shell width was not taken as the typical value for superbubbles of $\sim 15\%$, but instead a lower limit of 1% arising from the evolution of a strong shock disregarding instabilities (Lozinskaya (1992)). A lower limit in shell thickness means a lower limit in the total mass of the shell. The fact that we measure a lower limit in mass will be important later in the discussion.

For the age we use the relation $t = 2/7 * (R/v)$, from the analytic expression for the evolution of a supernova remnant in the snowplough phase (McKee & Ostriker (1977)). The use of this expression is justified in the following sections, where we also discuss the validity of the values calculated.

Lastly, we calculate the mean pre-shock density for each bubble assuming the shells swept out all of the gas they encountered, dividing the total mass of the shell by the total spherical bubble volume. We disregard the masses of the SN ejecta (a few solar masses), as the shell masses have much larger values.

The ISIS spectrum was used to compute emission line ratios, to probe the origin of the shells. To obtain results for each shell separately we applied a modified version of BUBBLY to each spectrum over the region in the spatial direction for each of these lines: H α , [SII] $_{6716}$, [SII] $_{6731}$ and [NII] $_{6584}$. To compute the doublet [NII] we used the relation [NII] $_{6584} = 3 * [NII]_{6548}$ which is independent of the physical parameters of the gas.

To improve the statistical significance of the ratios we repeated the detection

Este documento incorpora firma electrónica, y es copia auténtica de un documento electrónico archivado por la ULL según la Ley 39/2015.
Su autenticidad puede ser contrastada en la siguiente dirección <https://sede.ull.es/validacion/>

Identificador del documento: 973636

Código de verificación: QpwS3TwF

Fecha: 30/06/2017 14:40:15

Firmado por: ARTEMI CAMPS FARIÑA
UNIVERSIDAD DE LA LAGUNA

JOHN E. BECKMAN
UNIVERSIDAD DE LA LAGUNA

JOAN FONT SERRA
UNIVERSIDAD DE LA LAGUNA

ERNESTO PEREDA DE PABLO
UNIVERSIDAD DE LA LAGUNA

30/06/2017 15:07:38

30/06/2017 15:10:02

06/07/2017 13:51:28

using binning of 2, 3, 5, 6, 15 and 30 elements in the spatial direction, and used the mean value with the standard deviation as the error after eliminating clearly discrepant values.

The $[\text{SII}]_{6716}/[\text{SII}]_{6731}$ ratio is normally used as an indicator of density, following Osterbrock (1989), but in our case the values for density are in a range where the indicator has poor precision, and accounting for the uncertainties in the values the range in densities is rather high compared to the usual method with the $\text{H}\alpha$ flux. Despite this, the two methods yield compatible values. We show this in Figure 4.3, where we show simultaneously the density diagnostic, the line ratios we measured and the electron density obtained from the $\text{H}\alpha$ flux. We also represent the uncertainties in the values as coloured areas around the lines representing a value. To use the ratios as a diagnostic, we would take the X-value of the intersection between a blue line and the black line, but the flatness of the diagnostic line in the low-density area, coupled with the wide uncertainty margin means that we can only ascertain that the densities are in general below $\sim 300 \text{ cm}^{-3}$. Upon plotting the density values we should ideally expect that they intersect with both the ratios values and the diagnostic line if the measurements are compatible, which does happen as is clearly visible in the figure.

We could in principle also use the $[\text{SII}]_{6716}/[\text{SII}]_{6731}$ ratio as an indicator of density, but unfortunately the values measured are not within the range in which the ratio is sufficiently sensitive to density. Table 4.1 lists all parameters measured in the bubbles, both from GHaFaS and ISIS data.

4.4.1 Archival properties of the cluster

We have supporting information from the literature obtained by querying the position with VizieR; the presence of a supernova remnant in this HII region detected using radio observations at lower angular resolution is reported by Gordon et al. (Gordon et al. (1999)) (Tables 1,2 #90). Also relevant is a survey of HII regions and molecular gas by Miura et al. (2012) which used archival Hubble Legacy Archive images to date the accompanying star cluster by fitting isochrones to a colour-magnitude diagram extracted using aperture photometry (see section 3.2.2). This gives an age range of 6-12 Myr for the cluster, which is also reported to have 51 O stars (Table 3 #27). This survey also shows a $2.2 \cdot 10^6 M_\odot$ molecular cloud adjacent to the cluster (Table 2 #24).

Este documento incorpora firma electrónica, y es copia auténtica de un documento electrónico archivado por la ULL según la Ley 39/2015.
Su autenticidad puede ser contrastada en la siguiente dirección <https://sede.ull.es/validacion/>

Identificador del documento: 973636 Código de verificación: QpwS3TwF

Firmado por: ARTEMI CAMPS FARIÑA UNIVERSIDAD DE LA LAGUNA	Fecha: 30/06/2017 14:40:15
JOHN E. BECKMAN UNIVERSIDAD DE LA LAGUNA	30/06/2017 15:07:38
JOAN FONT SERRA UNIVERSIDAD DE LA LAGUNA	30/06/2017 15:10:02
ERNESTO PEREDA DE PABLO UNIVERSIDAD DE LA LAGUNA	06/07/2017 13:51:28

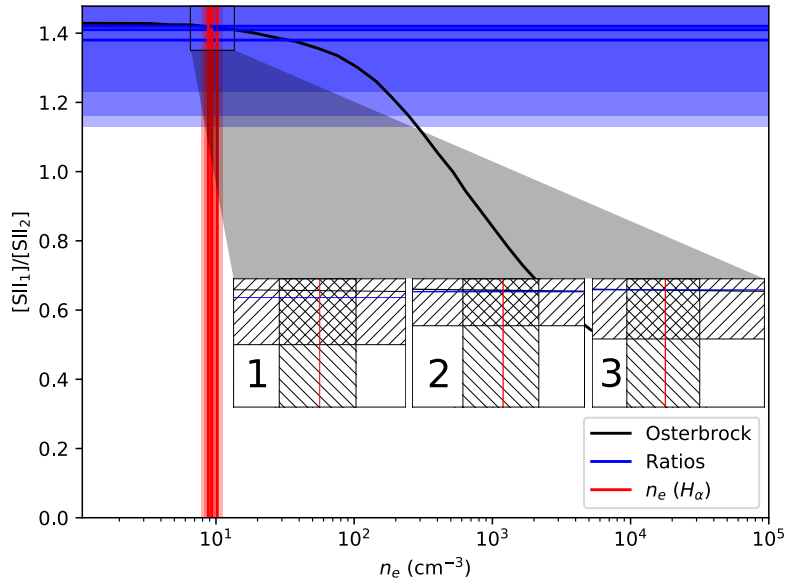


Figure 4.3: Comparison between the two methods for determining the electron density. The black line represents the Osterbrock (1989) line ratio diagnostic to obtain the density from a given $[\text{SII}]_{6716}/[\text{SII}]_{6731}$ ratio. The blue lines are the values of the ratio for our bubbles, with the uncertainty represented as blue-coloured areas. In the same fashion but in red, we show the densities obtained using the $H\alpha$ flux, with the corresponding errors represented as red-coloured areas. For ease of comparison, we show a zoom-in on the intersection of each bubble individually, with the uncertainties represented as patterns. It is apparent that the values for density and the ratios cross at a point compatible with the line diagnostic for each case.

Este documento incorpora firma electrónica, y es copia auténtica de un documento electrónico archivado por la ULL según la Ley 39/2015.
Su autenticidad puede ser contrastada en la siguiente dirección <https://sede.ull.es/validacion/>

Identificador del documento: 973636

Código de verificación: QpwS3TwF

Firmado por: ARTEMI CAMPS FARIÑA
UNIVERSIDAD DE LA LAGUNA

Fecha: 30/06/2017 14:40:15

JOHN E. BECKMAN
UNIVERSIDAD DE LA LAGUNA

30/06/2017 15:07:38

JOAN FONT SERRA
UNIVERSIDAD DE LA LAGUNA

30/06/2017 15:10:02

ERNESTO PEREDA DE PABLO
UNIVERSIDAD DE LA LAGUNA

06/07/2017 13:51:28

Table 4.1: Physical properties of the bubbles

	Bubble 1	Bubble 2	Bubble 3
Radius (pc)	22 ± 2	16 ± 2	12.5 ± 1
v_{exp} (km/s)	55 ± 5	115 ± 12	165 ± 17
$L_{H\alpha}$ (10^{36} erg/s)	4.4 ± 0.4	1.4 ± 0.2	0.61 ± 0.06
n_e (cm $^{-3}$)	10.2 ± 1.1	9.3 ± 1.1	8.8 ± 1.0
Mass (M $_\odot$)	337 ± 34	118 ± 12	54 ± 5
E $_k$ (10^{49} erg)	1.0 ± 0.2	1.6 ± 0.3	1.4 ± 0.3
Age* (kyr)	114 ± 16	40 ± 6	21 ± 3
n_0^* (cm $^{-3}$)	0.31 ± 0.06	0.28 ± 0.06	0.26 ± 0.05
[SII]/H α	0.4 ± 0.15	0.45 ± 0.16	0.43 ± 0.09
[NII]/H α	0.44 ± 0.2	0.35 ± 0.09	0.27 ± 0.13
[SII] ₁ /[SII] ₂	1.38 ± 0.25	1.41 ± 0.18	1.42 ± 0.26

Notes. See Chapter 2 for details on how the properties were determined. n_e is the electron density inside the shell, while n_0 is the average ambient particle density it encountered. The properties marked with * (Age and ambient density) are only valid for a shock evolving in a homogeneous medium. The calculations use a lower limit for shell thickness, this implies that mass and kinetic energy are lower limits while density is an upper limit. Even then, the dependence on shell thickness is $\sqrt{\Delta R}$, so a factor 10 increase in the thickness would increase mass and energy a factor ~ 3 .

Este documento incorpora firma electrónica, y es copia auténtica de un documento electrónico archivado por la ULL según la Ley 39/2015.
Su autenticidad puede ser contrastada en la siguiente dirección <https://sede.ull.es/validacion/>

Identificador del documento: 973636 Código de verificación: QpwS3TwF

Firmado por: ARTEMI CAMPS FARIÑA UNIVERSIDAD DE LA LAGUNA	Fecha: 30/06/2017 14:40:15
JOHN E. BECKMAN UNIVERSIDAD DE LA LAGUNA	30/06/2017 15:07:38
JOAN FONT SERRA UNIVERSIDAD DE LA LAGUNA	30/06/2017 15:10:02
ERNESTO PEREDA DE PABLO UNIVERSIDAD DE LA LAGUNA	06/07/2017 13:51:28

4.4.2 Identification as supernova remnants

The identification as supernova remnants was made using forbidden line ratios [SII]/H α and [NII]/H α to place our bubbles within diagnostic plots which distinguish between supernova remnants, HII regions and planetary nebulae (Sabbadin et al. (1977), Garcia Lario et al. (1991)). The classic diagnostic of [SII]/H α > 0.4 is included in these plots as the region for SNR is delimited by this value on the X axis (see Fig. 4.4). All three fall well within the defined regions for SNR, though for bubbles 1 and 2 the error reaches the area for photoionized gas. Significantly, the same analysis for the central peak places it, as expected, within the area for HII regions.

Though the ratios indicate otherwise, an alternative origin for the bubbles might be stellar winds, but this is ruled out in practice; as winds are continuously injecting energy since the stars' birth they cannot produce the segregated concentric structure observed, as the individual bubbles would blend and merge into one structure before growing to their current size, which already encompasses most of the cluster. The only possibility for winds to produce bubbles afterwards would be a red supergiant wind accelerated by a subsequent Wolf-Rayet phase (see Freyer et al. (2006)), but the stars capable of producing this effect have masses over $25 M_{\odot}$ and could no longer be present, barring multiple star formation bursts.

An O9 star ejects about 1 solar mass in wind throughout its lifetime with a velocity of around 2000 km/s, taking values on the high side. This yields an injected kinetic energy of $4 \cdot 10^{51}$ erg, similar to our energies though assuming perfect efficiency. The momentum, however, does not match the value for these parameters: $2 \cdot 10^3 M_{\odot} \text{ km s}^{-1}$, while our bubbles have values of around $9 \cdot 10^3$, $13 \cdot 10^3$, $18 \cdot 10^3 M_{\odot} \text{ km s}^{-1}$ in respective order. Interestingly, this does match the momentum for a supernova remnant, which typically has an initial ejecta mass of $\sim 1\text{-}10 M_{\odot}$ with a velocity of $10 \cdot 10^3 \text{ km s}^{-1}$.

Another possibility is that we are observing recurrent bursts from a Luminous Blue Variable (LBV) star. LBV are massive stars in an advanced stage of evolution that exhibit sudden outbursts and explosions, which have been sometimes been confused with supernova explosions, η Carinae is the best-known example of this type of object. The outflow of a LBV star is a plausible explanation for what we observe observations and has the advantage of requiring only a single star instead of three supernovae exploding within a short time-frame, but these stars typically have initial masses over $40 M_{\odot}$, which is incompatible with the age of the cluster as after 6 Myr all stars more massive than $19 M_{\odot}$ would have already died.

Este documento incorpora firma electrónica, y es copia auténtica de un documento electrónico archivado por la ULL según la Ley 39/2015.
Su autenticidad puede ser contrastada en la siguiente dirección <https://sede.ull.es/validacion/>

Identificador del documento: 973636

Código de verificación: QpwS3TwF

Fecha: 30/06/2017 14:40:15

Firmado por: ARTEMI CAMPS FARIÑA
UNIVERSIDAD DE LA LAGUNA

JOHN E. BECKMAN
UNIVERSIDAD DE LA LAGUNA

JOAN FONT SERRA
UNIVERSIDAD DE LA LAGUNA

ERNESTO PEREDA DE PABLO
UNIVERSIDAD DE LA LAGUNA

30/06/2017 15:07:38

30/06/2017 15:10:02

06/07/2017 13:51:28

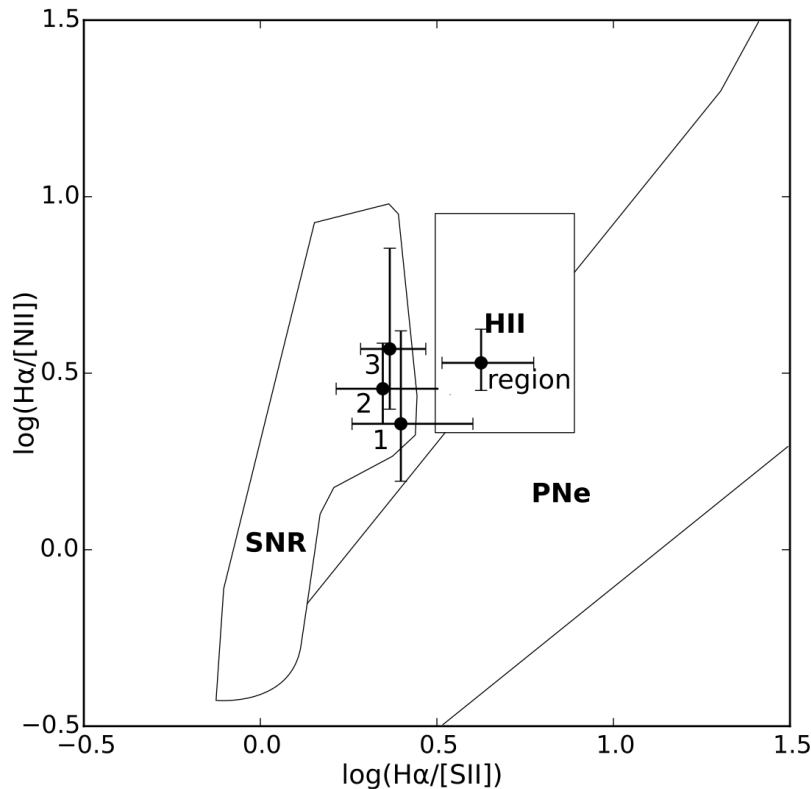


Figure 4.4: Diagnostic diagram used to distinguish between supernova remnants (SNR), HII regions (HII) and planetary nebulae (PNe) based on the relation between the SII to H α and NII to H α line ratios. We plot the remnants with their identifier numbers as well as the HII region.

Este documento incorpora firma electrónica, y es copia auténtica de un documento electrónico archivado por la ULL según la Ley 39/2015.
Su autenticidad puede ser contrastada en la siguiente dirección <https://sede.ull.es/validacion/>

Identificador del documento: 973636

Código de verificación: QpwS3TwF

Firmado por: ARTEMI CAMPS FARIÑA
UNIVERSIDAD DE LA LAGUNA

Fecha: 30/06/2017 14:40:15

JOHN E. BECKMAN
UNIVERSIDAD DE LA LAGUNA

30/06/2017 15:07:38

JOAN FONT SERRA
UNIVERSIDAD DE LA LAGUNA

30/06/2017 15:10:02

ERNESTO PEREDA DE PABLO
UNIVERSIDAD DE LA LAGUNA

06/07/2017 13:51:28

4.4.3 Physical properties

The evolution of supernova remnants is divided into three main phases, an initial free expansion while the mass of the ejecta dominates, an adiabatic expansion once the swept-up material mass is similar to that of the ejecta and a radiative phase, also called snowplough phase, in which the losses by radiation become significant and the gas cools. Given that the initial energy of a supernova is around 10^{51} erg our remnants currently have lost some 99% of their energy, which means that they must have been radiative for some time. We can check this using the expressions for the adiabatic phase (Hnatyk et al. (2007)):

$$R_{ST}(t) = \left(\frac{25E_{SN}}{4\pi\rho_0} \right)^{1/5} t^{2/5} \quad (4.1)$$

$$t_{tr} = 2.84 \cdot 10^4 E_{51}^{4/17} n_0^{-9/17} \quad (4.2)$$

Eq. 4.1 represents the evolution of radius with time as a factor of the energy in the supernova E_{SN} and the ambient density ρ_0 . Eqn 4.2 shows the expression to calculate the transition time between the adiabatic Sedov-Taylor phase and the radiative, snowplough phase as a factor of the energy in units of 10^{51} erg (E_{51}) and the ambient particle density n_0 .

Using the measured ambient density we find a transition time of 54 kyr which does not fit the data, as two of our remnants should not have transitioned yet. Furthermore, even with the faster expansion of the adiabatic phase we find predicted sizes roughly double the measured radii. This means that, apparently, we have remnants that should still be in the energy conserving phase yet have lost most of it already, and they are much smaller than expected. We will address this apparent inconsistency again shortly.

The mass range for the progenitor stars, calculated from the age of the cluster, is from ~ 15 to $19 M_\odot$, which is not unreasonable if we find three similar mass stars in a cluster of this size. Given the relatively short intervals between the supernova explosions, their progenitors must have had very similar masses.

It bears mention, however, that other factors such as metallicity and helium abundance affect the lifespan of a star Mengel et al. (1979), and given the small differences in mass we are considering these can be relevant factors. In practice, what this means is that the order in remnant ages is not necessarily that of the masses of the progenitor stars.

Este documento incorpora firma electrónica, y es copia auténtica de un documento electrónico archivado por la ULL según la Ley 39/2015.
Su autenticidad puede ser contrastada en la siguiente dirección <https://sede.ull.es/validacion/>

Identificador del documento: 973636 Código de verificación: QpwS3TwF

Firmado por: ARTEMI CAMPS FARIÑA UNIVERSIDAD DE LA LAGUNA	Fecha: 30/06/2017 14:40:15
JOHN E. BECKMAN UNIVERSIDAD DE LA LAGUNA	30/06/2017 15:07:38
JOAN FONT SERRA UNIVERSIDAD DE LA LAGUNA	30/06/2017 15:10:02
ERNESTO PEREDA DE PABLO UNIVERSIDAD DE LA LAGUNA	06/07/2017 13:51:28

The swept-up masses of the shells are very interesting. Their values are not consistent with the simplest models but they give us a clue to solve the inconsistency in the physical parameters. In a homogeneous medium the expanding shock should sweep out almost all the surrounding gas into the shell leaving a very rarefied medium, so that a second supernova soon after the first should sweep up hardly any material, lengthening the free-expansion phase. In spite of this, we find that each consecutive remnant has accumulated tens of solar masses of material. This is so even though our value for the thickness of each shell is a lower limit, meaning the masses are also lower limits as they scale with the square root of the thickness. A mechanism is needed to replenish gas inside a remnant for the next shell to encounter sufficient material. The most plausible is mass-loading from cold dense clouds. It has long been suspected that the interior of an HII region is not homogeneous nor fully ionized, and that small molecular clouds can survive for a long time inside it as they slowly evaporate (Bok & Reilly (1947)).

Hydrodynamic ablation by shocks or supersonic winds can also disrupt such clouds, so each supernova shell feeds gas to the next one. The effects of the interaction on the shell are also important. Simulations show (Chevalier (1974)) that upon encountering a cold, dense cloud, the shell will tend towards radiative evolution, rapidly slowing down and losing energy, greatly advancing its stage of evolution. In the cited paper a simple model with a single density jump at a fixed radius is used, while we expect clusters of clodlets instead. Either way, the effect of a density jump on the shell is what we have observed in our remnants, so adding the condition of inhomogeneity to our model explains the apparent inconsistencies. It also means that the ages estimated assuming a homogeneous medium are not correct. An inhomogeneous medium slows down the remnants, so our values are upper limits, but they should be within a small factor of the real expansion ages.

4.5 Discussion

We have presented results which are a good indication of the presence of three currently expanding supernova remnants within a single young HII region. Our key claim is that the expansion detected must arise from three different objects. Initially, we considered other geometrical configurations, such as typical complex structures in HII regions with several arches and cavities, but we detect very clearly an approaching and receding component for all three along the same lines of sight, so they are either nested or aligned on the line of sight. Given the similar size of the bubbles relative to the cluster, and their concentricity, we believe that nested shells offer the simpler explanation.

Este documento incorpora firma electrónica, y es copia auténtica de un documento electrónico archivado por la ULL según la Ley 39/2015.
Su autenticidad puede ser contrastada en la siguiente dirección <https://sede.ull.es/validacion/>

Identificador del documento: 973636 Código de verificación: QpwS3TwF

Firmado por: ARTEMI CAMPS FARIÑA UNIVERSIDAD DE LA LAGUNA	Fecha: 30/06/2017 14:40:15
JOHN E. BECKMAN UNIVERSIDAD DE LA LAGUNA	30/06/2017 15:07:38
JOAN FONT SERRA UNIVERSIDAD DE LA LAGUNA	30/06/2017 15:10:02
ERNESTO PEREDA DE PABLO UNIVERSIDAD DE LA LAGUNA	06/07/2017 13:51:28

We found that the physical properties appeared inconsistent given their masses, kinetic energies and ages. This is solved considering an inhomogeneous medium with embedded dense clumps of molecular gas, which would rob the remnants of energy as well as refill the ambient gas to be swept up by the subsequent supernova explosions. Because of this, our interpretation requires such clumps to survive for a long time inside the HII region.

The survival of clumps inside HII regions has long since been documented, (Bok & Reilly (1947)), and they have been found even in extreme examples such as 30 Doradus (Indebetouw et al. (2013)), where a complex of molecular clouds is found associated with the brightest star cluster.

The effect of stellar winds and radiation on their parent molecular clouds has been studied in simulations by Rogers & Pittard (2013) and Dale et al. (2014). In the former, three massive $\sim 30 M_{\odot}$ stars affect a surrounding 4 pc massive molecular cloud. The main finding is that the winds carve low density channels through which the gas escapes, making the denser regions surprisingly resistant to ablation. Another important result is that dense clumps are largely impervious to supernova shocks. They find that the dense material is either destroyed or pushed outside the original 4 pc radius in just over 6 Myr, which coincides with the lower limit of the age for our HII region. Dale et al. (2014) perform cluster-scale simulations and find results compatible to those of Rogers & Pittard (2013) with a very structured dense medium. They use molecular clouds with a variety of physical parameters finding that the denser, more massive clouds are much harder to disrupt. For lower mass clouds the stars carve irregular cavities on scales of 10 pc. The molecular cloud associated with our cluster is similar to the densest and most massive of Dale et al. (2014)'s.

Both studies show that the presence of embedded clumps is expected in clusters born from massive molecular clouds, and that they can easily survive until the stars explode as supernovae. We also need to estimate the rate of cloud evaporation required to refill the gas and reproduce the masses in the observed shell. From the masses and ages of the remnants we require an injection rate of about $25 M_{\odot}$ per 10 kyr. Dale et al. (2014) find that except at the onset of star formation, winds hardly affect the disruption of the molecular cloud; with photoevaporation dominating this process, so here we need consider only cloud destruction by photoevaporation.

Using the relation from Pittard (2007) for photoevaporation and taking a sample cloud with radius 1 pc at a distance of 10 pc from the centre of the cluster, we estimate the flux of ionizing photons from the cluster using its H α luminosity and obtain an injection rate of $0.8 M_{\odot}$ per 10 kyr. We can therefore easily reproduce the required mass injection without an overly large number of clouds, even accounting for the fact that our masses are lower limits.

Este documento incorpora firma electrónica, y es copia auténtica de un documento electrónico archivado por la ULL según la Ley 39/2015.
Su autenticidad puede ser contrastada en la siguiente dirección <https://sede.ull.es/validacion/>

Identificador del documento: 973636 Código de verificación: QpwS3TwF

Firmado por: ARTEMI CAMPS FARIÑA UNIVERSIDAD DE LA LAGUNA	Fecha: 30/06/2017 14:40:15
JOHN E. BECKMAN UNIVERSIDAD DE LA LAGUNA	30/06/2017 15:07:38
JOAN FONT SERRA UNIVERSIDAD DE LA LAGUNA	30/06/2017 15:10:02
ERNESTO PEREDA DE PABLO UNIVERSIDAD DE LA LAGUNA	06/07/2017 13:51:28

Feedback from stellar winds and supernovae plays an important role in many processes relevant to galaxy evolution. As well as those mentioned above there is the possible dissipation of nuclear dark matter cusps (Pontzen & Governato (2012)), the dissipation of metals both within galaxies (Spitoni et al. (2009)) and from galaxies into the intergalactic medium (Heckman et al. (1990)), and the enhancement of the infall rate of low metallicity intergalactic gas to the disc, by its interaction with supernova ejectae in the galactic halo (Marasco et al. (2012)). To incorporate any of these effects into models of the formation and evolution of galaxies, it is clearly important to have not only model inputs to the dynamics of the interaction of the winds and supernovae with the surrounding ISM, but measurements which can help quantify the process. As the stars in massive star clusters form virtually simultaneously, cases of multiple supernova explosions must be common enough to be incorporated into the relevant models. But much more generally to make realistic models mass loading of the expansion via the dissipation of dense cool clumps must be taken into consideration. The triple supernova has allowed us to illustrate its importance, and make quantitative estimates of relevant parameters for much wider application.

Este documento incorpora firma electrónica, y es copia auténtica de un documento electrónico archivado por la ULL según la Ley 39/2015.
Su autenticidad puede ser contrastada en la siguiente dirección <https://sede.ull.es/validacion/>

Identificador del documento: 973636

Código de verificación: QpwS3TwF

Fecha: 30/06/2017 14:40:15

Firmado por: ARTEMI CAMPS FARIÑA
UNIVERSIDAD DE LA LAGUNA

JOHN E. BECKMAN
UNIVERSIDAD DE LA LAGUNA

JOAN FONT SERRA
UNIVERSIDAD DE LA LAGUNA

ERNESTO PEREDA DE PABLO
UNIVERSIDAD DE LA LAGUNA

30/06/2017 15:07:38

30/06/2017 15:10:02

06/07/2017 13:51:28

Este documento incorpora firma electrónica, y es copia auténtica de un documento electrónico archivado por la ULL según la Ley 39/2015.
Su autenticidad puede ser contrastada en la siguiente dirección <https://sede.ull.es/validacion/>

Identificador del documento: 973636

Código de verificación: QpwS3TwF

Firmado por: ARTEMI CAMPS FARIÑA
UNIVERSIDAD DE LA LAGUNA

Fecha: 30/06/2017 14:40:15

JOHN E. BECKMAN
UNIVERSIDAD DE LA LAGUNA

30/06/2017 15:07:38

JOAN FONT SERRA
UNIVERSIDAD DE LA LAGUNA

30/06/2017 15:10:02

ERNESTO PEREDA DE PABLO
UNIVERSIDAD DE LA LAGUNA

06/07/2017 13:51:28

5

Superbubbles in the Antennae galaxies

5.1 Introduction

The injection of energy by massive stars into their surrounding medium generally produces expanding bubbles which occur over a wide range of scales, from sizes of a few pc around single stars to kpc scale superbubbles blown by starbursts. Measuring the properties of these bubbles, notably their kinetic energies of expansion, is essential for the evaluation of stellar feedback, in galaxy discs and in their circumnuclear zones. These measurements can also be useful for indirect estimation of the properties of the originating star or star cluster, constraining parameters such as the minimum number of OB stars in a cluster which could power the bubble. It is particularly interesting to estimate the age of the bubble, because this allows us to estimate the age of the star cluster itself, given that feedback commonly shuts off further star formation inside an HII region after the initial burst and the winds by the massive stars begin to act immediately on the gas. However the accuracy of these estimates is limited by the reliability of the model used to predict the evolution of the expanding bubble, which tend to be simplified, unless one performs detailed studies of individual cases, and preferably with well-structured simulations. In spite of the limitations this is a useful method for estimating cluster ages when lacking the resolution needed to resolve the individual stars.

The strongly interacting pair of galaxies NGC 4038/4039 (also Arp 244, and commonly known as the Antennae) is in the intermediate stages of a merger. The interaction has triggered a powerful starburst, notably in the overlap region

where the interaction is strongest. As this object is one of the nearest examples of this type of starbursts it attracts considerable attention, and is one of the most studied galaxy pairs in the sky. This environment is an ideal laboratory for the probing of feedback by massive stars. The young stellar clusters have been studied extensively both as a population, measuring their luminosity and mass functions (Whitmore et al. (1999),Fritze-v. Alvensleben (1999),Zhang & Fall (1999),Mengel et al. (2005),Whitmore et al. (2010)), and individually in detail (Bastian et al. (2006),Mengel et al. (2002),Whitmore et al. (2005)). There are also studies of the molecular gas and dust, and their relation to the star clusters (Wilson et al. (2000),Nikola et al. (1998),Gao et al. (2001),Zhu et al. (2003),Wilson et al. (2003)). In a recent publication (Zaragoza-Cardiel et al. (2014)) the authors of this thesis and collaborators have compared the mass functions and the density distributions of the molecular and ionized gas clouds, showing that for both gas phases there are two populations, divided at a critical mass which is comparable for the HII region population and that of the molecular clouds.

Bubbles and superbubbles in general have long been subjects of study, as they have been well detected in the Galaxy and in nearby galaxies. Most of these detections have been made in neutral hydrogen, using the kinematics of the 21 cm line, and include the local bubble around the solar neighbourhood (Cox & Reynolds (1987)) as well as bubbles in M31 (Brinks & Bajaja (1986)), M33 (Deul & den Hartog (1990)). Detections have also been made using the ionized gas with H α in the Magellanic clouds (Meaburn (1980),Meaburn (1984),Rosado (1986),Le Coarer et al. (1993),Chu & Kennicutt (1994)), and more recently Ambrocio-Cruz et al. (2016); Reyes-Iturbide et al. (2014) for the LMC superbubbles. Examples of expansion in galactic outbursts such as in M82 (Bland & Tully (1988)), NGC 3079 (Veilleux et al. (1994)) and the irregular galaxy IC 1613 (Valdez-Gutiérrez et al. (2001)) have been reported. These are only a few selected examples of a progressively extending literature on the subject. But given the importance of stellar feedback on galaxy evolution in general amplifying the observation and above all the quantification of superbubbles to as large a sample of galaxies as possible is of strong interest to the field.

5.2 Observations

We observed the Antennae pair of galaxies using the Galaxy H α Fabry-Perot system (GH α FaS,Hernandez et al. (2008); Fathi et al. (2008)), obtaining a calibrated data cube which mapped kinematically the H α emission line over the extent of both galaxies, with only the extended HI tails falling outside the

Este documento incorpora firma electrónica, y es copia auténtica de un documento electrónico archivado por la ULL según la Ley 39/2015.
Su autenticidad puede ser contrastada en la siguiente dirección <https://sede.ull.es/validacion/>

Identificador del documento: 973636 Código de verificación: QpwS3TwF

Firmado por: ARTEMI CAMPS FARÍÑA UNIVERSIDAD DE LA LAGUNA	Fecha: 30/06/2017 14:40:15
JOHN E. BECKMAN UNIVERSIDAD DE LA LAGUNA	30/06/2017 15:07:38
JOAN FONT SERRA UNIVERSIDAD DE LA LAGUNA	30/06/2017 15:10:02
ERNESTO PEREDA DE PABLO UNIVERSIDAD DE LA LAGUNA	06/07/2017 13:51:28

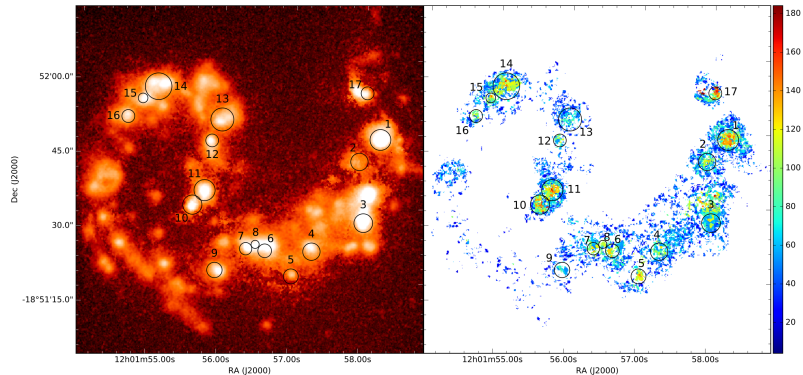


Figure 5.1: On the right we show the expansion map for the Antennae galaxies, colour coded in velocity of expansion, that is, the mean separation in velocity of the secondary components. On the left is a map of H α intensity for comparison. The circles represent the superbubble detections in both maps for ease of comparison, with their radius coinciding with the estimated bubble radius. The superbubbles clearly appear around most of the brightest regions. The presence of an extended, widely disseminated low expansion velocity component can also be appreciated (see text for a discussion on its possible origins).

field. In practice we mapped the full extent of the H α emission from the object. The observations were first presented in Zaragoza-Cardiel et al. (2014).

For the spectroscopic part of the study we used the Intermediate Dispersion Spectrograph (IDS) at the Cassegrain focus of the 2.5 m Isaac Newton Telescope (INT) also at the ORM. This yields long-slit spectra, 3.3 arcmin unvignetted, and we used a slit-width of 1 arcsec, and a grating which produced a plate scale of 0.44 Å/pixel using the RED+2 detector. The aim of the long-slit spectroscopy was to measure the relative intensities of the H α , [NII] doublet, and [SII] doublet lines, to compute line ratios and then perform tests on the ionizing radiation of the detected expanding shells. The spectra were reduced using IRAF and was particularly simple; the lines are close enough together and observed with the same system so that reddening correction was not needed, nor was calibration necessary as we were interested only in the line ratios.

5.3 Expansion map

In Figure 5.1 we show the expansion map of the Antennae, next to an H α surface brightness image, for comparison. The map shows detected expansion at some level of significance across practically the full extent of the area with

Este documento incorpora firma electrónica, y es copia auténtica de un documento electrónico archivado por la ULL según la Ley 39/2015.
Su autenticidad puede ser contrastada en la siguiente dirección <https://sede.ull.es/validacion/>

Identificador del documento: 973636

Código de verificación: QpwS3TwF

Fecha: 30/06/2017 14:40:15

Firmado por: ARTEMI CAMPS FARIÑA
UNIVERSIDAD DE LA LAGUNA

JOHN E. BECKMAN
UNIVERSIDAD DE LA LAGUNA

JOAN FONT SERRA
UNIVERSIDAD DE LA LAGUNA

ERNESTO PEREDA DE PABLO
UNIVERSIDAD DE LA LAGUNA

30/06/2017 15:07:38

30/06/2017 15:10:02

06/07/2017 13:51:28

detected H α emission, but it is clear that around most of the brightest HII regions we find more coherent structures, which show higher detected velocities of expansion. These are what we claim are superbubble detections, and this claim is supported by the coincidence of their centres with those of the HII regions themselves, as well as by the radial symmetry they show. In the figure we have marked the presence of each superbubble with black circles both on the expansion map and on the H α map; these circles show their estimated radial sizes.

Some of these bubbles are very well defined: bubbles with the identifiers 1, 10, 11 and 14 are particularly prominent, showing better coverage and spatial coherence. It is also interesting to pay particular attention to the overlap zone, the area where the interaction has the most effect on the ISM, and where there are some of the brightest HII regions, which have made this the most explored part of the object as found in the literature. In this area we find the clearest superbubble, identified as bubble 1, but we also see in the area below bubble 2 a zone with quite a lot of high velocity expansion which does not, however, show circular morphology coincident with the underlying HII regions. This probably indicates that while there are indeed massive outflows from these young regions they do not maintain the pseudo-spherical shape of a bubble, (due probably to the inhomogeneity of the surrounding ISM), or that the shape is too complicated for us to determine with our data and method. For an irregularly shaped expanding shell the difference in velocity between the approaching and receding surfaces would in any case prevent our method from detecting it. This is a possible factor underlying the incoherent detections shown.

We can also see that, apart from the detections on and around the bright HII regions there is extended, less geometrically coherent detection across the full face of the interacting galaxies. It is interesting to note, however, that in other galaxies analysed in the same way we have found much less, or none of this extended expansion detection, above all in those galaxies in a more quiescent state. This leads us to believe that the dominant cause of these detections is not noise, but unresolved expansion, and more complex kinematic structure. These features also have low expansion velocities, which fits the scenario of smaller, less energetic drivers of the motion.

5.4 Physical properties of the superbubbles

From the expansion map we have a direct measurement of the expansion velocity and size of a superbubble. The flux is calculated using the relative intensities of the secondary peaks and a calibrated H α image of the object. These are the

Este documento incorpora firma electrónica, y es copia auténtica de un documento electrónico archivado por la ULL según la Ley 39/2015.
Su autenticidad puede ser contrastada en la siguiente dirección <https://sede.ull.es/validacion/>

Identificador del documento: 973636

Código de verificación: QpwS3TwF

Fecha: 30/06/2017 14:40:15

Firmado por: ARTEMI CAMPS FARIÑA
UNIVERSIDAD DE LA LAGUNA

JOHN E. BECKMAN
UNIVERSIDAD DE LA LAGUNA

JOAN FONT SERRA
UNIVERSIDAD DE LA LAGUNA

ERNESTO PEREDA DE PABLO
UNIVERSIDAD DE LA LAGUNA

30/06/2017 15:07:38

30/06/2017 15:10:02

06/07/2017 13:51:28

primary quantities used to calculate the other physical parameters. A detailed description of the calculations was described in chapter 2, but essentially we use the relation:

$$L_{H\alpha}(\text{shell}) = 4\pi R^2 \Delta R n_e^2 \alpha(H, T) h\nu \quad (5.1)$$

R stands for the shell radius, ΔR is its thickness and n_e is the electron density. $\alpha(H, T)$ is the effective recombination coefficient for hydrogen and $h\nu$ is the energy of an $H\alpha$ photon. We have no direct way of measuring the shell width ΔR so we need to use an approximation. In section 5.5 we perform hydrodynamical simulations of one of the detected bubbles, from which we derive a canonical value of 15% of the radius, which is also consistent with observations of local superbubbles (Oey (1996)).

With these quantities we can estimate the electronic density in the shell, and together with the radius, the shell thickness, and the velocity we can derive the total mass and the current kinetic energy for the ionized gas. While the uncertainty in the shell thickness certainly affects our results the systematic uncertainty depends on $\sqrt{\Delta R}$ implying that an error by a factor as high as 3 in shell width implies only a change of ~ 1.8 in density, mass and energy. The density decreases with increasing shell width, whereas mass and density decrease. The values of the derived physical parameters for all the identified superbubbles are given in Table 5.1. An additional initial approximation we have used is that the bubbles are spherical. This would be good for homogeneous environments, but as our superbubbles are comparable to the scale height of the surrounding ISM, its density gradient is relevant. Many superbubbles are approaching or in the breakout phase of their evolution, so their shapes will be elongated perpendicular to the disc, i.e. in the direction of falling density, and their expansion velocity will not be isotropic. In section 5.5 we use hydrodynamic simulations to reproduce one of the superbubbles, which gives us a useful approach to discuss these effects and their implications for the validity of our numerical parameters.

The age we present is a simple estimate, obtained by dividing the observed radius by the expansion velocity, as though the bubbles expanded freely. The surrounding gas will always slow down the bubbles, so these estimates are lower limits to the bubble ages. A formula which has been commonly used in the literature for the expansion time t , is $t = 0.6R/v$, which is obtained assuming constant momentum injection into a homogeneous isotropic medium. But this is a reasonable assumption only for bubbles which are small compared to the disc scale height, which is not the case for the superbubbles we have found here. As there is no standard treatment of this problem, we have preferred, in the

Este documento incorpora firma electrónica, y es copia auténtica de un documento electrónico archivado por la ULL según la Ley 39/2015.
Su autenticidad puede ser contrastada en la siguiente dirección <https://sede.ull.es/validacion/>

Identificador del documento: 973636 Código de verificación: QpwS3TwF

Firmado por: ARTEMI CAMPS FARIÑA UNIVERSIDAD DE LA LAGUNA	Fecha: 30/06/2017 14:40:15
JOHN E. BECKMAN UNIVERSIDAD DE LA LAGUNA	30/06/2017 15:07:38
JOAN FONT SERRA UNIVERSIDAD DE LA LAGUNA	30/06/2017 15:10:02
ERNESTO PEREDA DE PABLO UNIVERSIDAD DE LA LAGUNA	06/07/2017 13:51:28

Chapter 5. Superbubbles in the Antennae galaxies

Table 5.1: Table with the physical parameters of the superbubbles detected in the Antennae galaxies.

No.	Radius (pc)	v_{exp} (km/s)	L_{shell} (10^{39} erg/s)	n_e (cm $^{-3}$)	Mass (10^{35} Kg)	E_k (10^{51} erg)	Age (Myr)	AgeG&G (Myr)	Agew&Z (Myr)
(1)	(2)	(3)	(4)	(5)	(6)	(7)	(8)	(9)	(10)
1	391 ± 39	132 ± 13	1.45 ± 0.1	0.73 ± 0.08	31 ± 6	267 ± 76	2.9 ± 0.4	3.45	3.8,3.7 ^a
2	326 ± 33	115 ± 12	0.9 ± 0.1	0.77 ± 0.1	19 ± 4	124 ± 35	2.8 ± 0.4	5.72 ^a	3.0
3	352 ± 35	62 ± 6	1.3 ± 0.1	0.83 ± 0.09	25 ± 5	49 ± 14	5.5 ± 0.8		7.4,2.5
4	326 ± 33	115 ± 12	0.2 ± 0.03	0.36 ± 0.04	9 ± 2	57 ± 16	2.8 ± 0.4	6.19	
5	280 ± 28	125 ± 13	0.14 ± 0.02	0.38 ± 0.04	6 ± 1	45 ± 13	2.2 ± 0.3		8.4 ^a
6	257 ± 26	125 ± 13	0.22 ± 0.04	0.53 ± 0.07	6 ± 1	49 ± 14	2 ± 0.3		
7	232 ± 23	120 ± 12	0.21 ± 0.03	0.61 ± 0.08	5 ± 1	38 ± 11	1.9 ± 0.3		5.0
8	153 ± 15	110 ± 11	0.09 ± 0.02	0.7 ± 0.1	1.8 ± 0.4	11 ± 3	1.4 ± 0.2		4.0 ^a
9	289 ± 29	97 ± 10	0.18 ± 0.02	0.41 ± 0.05	7 ± 1	32 ± 9	2.9 ± 0.4		2.0 ^a
10	361 ± 36	152 ± 15	0.92 ± 0.1	0.66 ± 0.07	22 ± 4	250 ± 71	2.3 ± 0.3	7.0	2.0
11	396 ± 40	168 ± 17	0.37 ± 0.03	0.36 ± 0.04	16 ± 3	224 ± 63	2.3 ± 0.3		2.0,4.8 ^a
12	240 ± 24	115 ± 12	0.12 ± 0.02	0.43 ± 0.05	4.2 ± 0.8	28 ± 8	2 ± 0.3		2.0
13	432 ± 43	85 ± 9	0.4 ± 0.04	0.33 ± 0.04	19 ± 4	68 ± 19	5 ± 0.7		6.0
14	501 ± 50	117 ± 12	1.3 ± 0.2	0.48 ± 0.06	42 ± 8	287 ± 81	4.2 ± 0.6		4.5,6.4,4.0 ^a
15	182 ± 18	145 ± 15	0.12 ± 0.02	0.67 ± 0.08	2.8 ± 0.6	30 ± 8	1.2 ± 0.2	6.61 ^a	7.0
16	243 ± 24	120 ± 12	0.17 ± 0.03	0.51 ± 0.06	5 ± 1	37 ± 10	2 ± 0.3		5.2 ^a
17	243 ± 24	165 ± 17	0.24 ± 0.04	0.61 ± 0.08	6 ± 1	83 ± 23	1.4 ± 0.2		

Notes. Col. (1) corresponds to the superbubble identifier numbers, radius (2) and v_{exp} (3) are estimated directly on the expansion map and have an assigned 10% error. Luminosity is measured from the ACAM image, its error inferred from the difference in luminosity at low and high limits for radius. The rest of the properties are calculated using the first three (see text for details) except for the cluster ages (9,10) which are taken from spectroscopic and photometric studies of the clusters. Column (9) corresponds to ages measured by Gilbert & Graham (2007) using their Br- γ equivalent width. Column (10) shows Whitmore & Zhang (2002)'s measurement of the cluster ages, comparing UBVRI colors with spectral evolution models. The clusters are matched spatially to our bubbles, though several bubbles encompassed several clusters, we show the ages for all spatially coincident clusters, ordered by putting the clusters closest to the centre of the bubble first. The less reliable matches, which correspond to clusters found close to the edge of the superbubble detection are marked with ^a.

Este documento incorpora firma electrónica, y es copia auténtica de un documento electrónico archivado por la ULL según la Ley 39/2015. Su autenticidad puede ser contrastada en la siguiente dirección https://sede.ull.es/validacion/		
Identificador del documento: 973636		Código de verificación: QpwS3TwF
Firmado por: ARTEMI CAMPS FARÍÑA UNIVERSIDAD DE LA LAGUNA	Fecha: 30/06/2017 14:40:15	
JOHN E. BECKMAN UNIVERSIDAD DE LA LAGUNA	30/06/2017 15:07:38	
JOAN FONT SERRA UNIVERSIDAD DE LA LAGUNA	30/06/2017 15:10:02	
ERNESTO PEREDA DE PABLO UNIVERSIDAD DE LA LAGUNA	06/07/2017 13:51:28	

first instance to use fewer assumptions and present lower limits to the ages.

Fortunately, as this is a well-studied object, there are references in the literature for the ages of the star clusters in this object. Gilbert & Graham (2007) use Hubble Space Telescope (HST) spectra to measure the Br- γ equivalent width of the clusters and compare it to synthetic stellar populations obtained using *Starburst99*. Another source is Whitmore & Zhang (2002), where they improve on a previous age determination comparing *UBVI* colors to spectral evolution models by A.G. Bruzual and S. Charlot. This is done using HST H α images to break the age-reddening degeneracy and correct the contamination of the V observations by the emission line. We present the associated cluster ages in Table 5.1 for each bubble. The clusters were spatially matched to the measured extent of the superbubbles, and all matches found are presented for each age determination. Given the size of our superbubbles, they tend to encompass several stellar clusters, so in some cases we have multiple age determinations associated with a superbubble. Some of these lie close to the edge of the superbubble, making them less reliable, these are indicated in the table. Most of our superbubbles have at least a cluster with similar age, with only bubbles 5 and 17 having no clear spatial match. This does not mean that there is no detected underlying cluster, only that there is not an age determination available from the literature.

The superbubbles listed in Table 5.1 are all very large, with radii in the range 150-500 pc. We do not detect smaller bubbles because of an inherent selection effect caused by the limit to the linear resolution at the distance of the Antennae and our requirement of morphological coherence to admit bubble candidates. As explained above, the smaller bubbles should be present within the widespread expansion signatures detected across the whole of the merging discs. Indeed there are "detection clusters" with 3-8 conjoined pixels having similar expansion velocities, but too small for us to make an estimate of a radius with reasonable accuracy. Given that the inferred physical parameters of a bubble are strongly dependent on its radius, we have chosen not to include these as detected bubbles in our list but have tried to make a macroscopic quantification of the total kinetic energy injected into the ISM of the complete system in a following subsection.

The luminosities of the bubbles correlate well with the total luminosity of the region in the area occupied by the bubble; the bubble luminosity is around an order of magnitude less than the luminosity of its region. Bubble 1 is significantly brighter than the others, with correspondingly higher values for the mass and kinetic energy of its shell, as might well be expected as its associated HII region is by far the brightest and youngest of the giant HII regions in the Antennae. The kinetic energy of an expanding shell is its key

Este documento incorpora firma electrónica, y es copia auténtica de un documento electrónico archivado por la ULL según la Ley 39/2015.
Su autenticidad puede ser contrastada en la siguiente dirección <https://sede.ull.es/validacion/>

Identificador del documento: 973636 Código de verificación: QpwS3TwF

Firmado por: ARTEMI CAMPS FARIÑA UNIVERSIDAD DE LA LAGUNA	Fecha: 30/06/2017 14:40:15
JOHN E. BECKMAN UNIVERSIDAD DE LA LAGUNA	30/06/2017 15:07:38
JOAN FONT SERRA UNIVERSIDAD DE LA LAGUNA	30/06/2017 15:10:02
ERNESTO PEREDA DE PABLO UNIVERSIDAD DE LA LAGUNA	06/07/2017 13:51:28

parameter, given the important role played by the energy injected into the ISM in galaxy evolution. It also provides a conservative constraint on population of the cluster, giving an estimated lower limit to the number of massive stars in the cluster necessary to power the expansion. To make interpretation easier we present the kinetic energies of the shells in units of 10^{51} erg, a canonical value of the kinetic energy produced in a supernova explosion. This is not to be taken as an estimate of the number of supernovae that have powered the superbubble, because the energy losses during the expansion are quite high, and increase in time as the shell moves outwards and each supernova remnant has to travel further to reach the shell. It does, however, serve as a lower limit on the number of O stars necessary to power it.

5.4.1 Extended detections

In order to estimate the kinetic energy in the unresolved expansion we carried out an estimate, using a set of assumptions. The main problem in calculating the kinetic energy associated with the unresolved detections is the value for the expansion radii. The velocity and luminosity detected on each pixel are straightforward quantities in the sense that they can be assigned to sections of a bubble without much loss of generality save for the projection effects on the velocity. The radius, however, is a global property of the bubble, so lacking a measurement of the radius corresponding to each pixel we cannot evaluate it correctly. For this reason we will assume that for our purposes each pixel is composed of a slab of material of dimensions X, Y, Z where X and Y correspond to the pixel size of 0.2 arcsec, corresponding to 23.4 pc, and Z is taken as the width of a shell of typical size, assuming a width of 15% as for the resolved superbubbles. In order to obtain a "typical" bubble size we use Zaragoza-Cardiel et al. (2015)'s sample of HII regions¹ and take the median radius of the HII regions with radius lower than that of our smallest resolved bubble (153 pc). In Zaragoza-Cardiel et al. (2015) the HII regions with an uncertainty in radius greater than 15% are discarded, but we need not do this for the estimate sought here. This selection would bias the sample to higher radii, and as we want the median value the individual uncertainties will cancel. The resulting median radius is 60 pc. Using this value the total kinetic energy for the extended, unresolved detection s is $1.72 \cdot 10^{54}$ erg, while the total equivalent energy in the resolved bubbles is $1.68 \cdot 10^{54}$ erg. The energy in the extended detections is thus of the same order as that in the resolved bubbles.

A possible caveat for this comparison is that the method for calculating the energy is different from that used for the resolved bubbles, where we have been

¹ Available at Vizier: J/MNRAS/451/1307

Firmado por: ARTEMI CAMPS FARIÑA UNIVERSIDAD DE LA LAGUNA	30/06/2017 15:07:38
JOHN E. BECKMAN UNIVERSIDAD DE LA LAGUNA	30/06/2017 15:10:02
JOAN FONT SERRA UNIVERSIDAD DE LA LAGUNA	06/07/2017 13:51:28
ERNESTO PEREDA DE PABLO UNIVERSIDAD DE LA LAGUNA	

able to measure the derived radius and expansion velocity. To account for this we simulated the effect by calculating the ratio between the two methods for a 60 pc radius bubble at our spatial resolution.

To project the bubble emission into equivalent pixels we calculated geometrically the volume of the intersection between a 23.4 pc x 23.4 pc wide column and a spherical shell to take into account the quantity of gas which emits the light observed in a single pixel. This enables us to derive a mock luminosity at the resolution of the instrument which, combined with the projected velocity along the line of sight allows us to estimate the difference between the true kinetic energy of the simulated bubble and that measured by summing the energy over all the pixels. For a bubble of typical size 60 pc the real energy is 1.9 times higher than the value calculated in this exercise. We carried out the equivalent computation for the full range of sizes in the HII region sample, and the median ratio coincides with that for the median radius, yielding a value of 1.9. This result implies that the method used to estimate the kinetic energy for the extended detections does not entail a large discrepancy from the true value, so if we correct by the factor the energy in the extended detections is $3.27 \cdot 10^{54}$ erg, now somewhat larger than, but still of the same order as that for the resolved superbubbles.

Of course this value cannot be taken as an accurate measurement, as there are several competing effects which could lower or raise it. We would expect the typical value for the radius to be skewed to larger radii because of the selection due to the limit of spatial resolution, which we would mean that we are overestimating the shell width, and consequently the mass and the energy. However our detections of expanding features are almost certainly not complete. The SNR ratio on which we base the estimates affects the fraction of true detections which are discarded, as well as false noise-generated "detections" which are included.

Even with these uncertainties it is apparent that the budget for kinetic energy injection into the ISM in this merging pair of galaxies is not dominated by the giant HII regions; the smaller regions are essentially on a par. This kind of energy input, affecting the whole of the observed pair of merging galaxies, must be taken into account when modelling the physics of mergers.

5.5 Hydrodynamic simulation

As the bubbles we have detected in the Antennae have radii of order several hundred pc we would expect them not to be spherical but to expand more rapidly in the direction perpendicular to the plane of the disc of their originating galaxy, and therefore to be elongated in that direction (Mac Low & McCray

Este documento incorpora firma electrónica, y es copia auténtica de un documento electrónico archivado por la ULL según la Ley 39/2015.
Su autenticidad puede ser contrastada en la siguiente dirección <https://sede.ull.es/validacion/>

Identificador del documento: 973636 Código de verificación: QpwS3TwF

Firmado por: ARTEMI CAMPS FARIÑA UNIVERSIDAD DE LA LAGUNA	Fecha: 30/06/2017 14:40:15
JOHN E. BECKMAN UNIVERSIDAD DE LA LAGUNA	30/06/2017 15:07:38
JOAN FONT SERRA UNIVERSIDAD DE LA LAGUNA	30/06/2017 15:10:02
ERNESTO PEREDA DE PABLO UNIVERSIDAD DE LA LAGUNA	06/07/2017 13:51:28

(1988)) even though the discs have become somewhat distorted during the interaction. They are likely to be approaching the break-out phase. In order to better quantify the values of the parameters derived from our observations, notably the ages of the bubbles, we considered it valuable to run models to simulate the phenomena. The exercise we used to test this approach was to attempt to reproduce our best detection, namely bubble 1.

5.5.1 Modelling setup

To perform the simulation we used a version of YGUAZU-A (Raga et al. (2000), Raga et al. (2002)) a 3D adaptive grid code which solves the Euler equations for each grid element. It was created in order to simulate the conditions of the interaction of the ISM with supernovae and the winds from massive stars, rather than using cosmological simulations or those simulating the evolution of complete galaxies, which are the focus of most hydrodynamic codes. It has also been used on larger scale outflows such as galactic filaments originating in star cluster winds (Rodríguez-González et al. (2008)) and a galactic jet from a galaxy cluster (Rodríguez-Martínez et al. (2006)).

This code is well suited to our problem, as it is easy to set the relevant physical parameters. We ran the code within an elongated box to accommodate to the evolution of the bubble, which grows quicker in the Z direction, with a maximum allowed resolution in the XYZ coordinates of 1024x1024x2048, corresponding to a physical size of 1000x1000x2000pc. The maximum resolution is just the number of cells, provided that all the cells are at maximum refinement. The time step for the outputs was set at 0.25 Myr.

The first step is to introduce the parameters which control the properties of the ISM and the injection of energy from the cluster. To model the input of momentum we assumed continuous injection and divided the total kinetic energy by the photometric age of the cluster, using a wind velocity of 1000 km s⁻¹. There are two implications of this choice: in the first place we are assimilating the momentum added by the supernovae to that injected by the winds. This assumption would be very inaccurate during the initial stages of the expansion, but given the current mass and radius of one of our shells it should not affect the outcome significantly. However, equating the current kinetic energy to the total input from the stars ignores radiation losses, implying that the input momentum is underestimated.

The distribution of the surrounding gas is more problematic, as we have little information on its details in order to deduce valid inputs. We have used a simple model of a disc, with an exponentially decreasing density profile in the Z direction, and isotropic XY. This gives us two free parameters, the density in

Este documento incorpora firma electrónica, y es copia auténtica de un documento electrónico archivado por la ULL según la Ley 39/2015.
Su autenticidad puede ser contrastada en la siguiente dirección <https://sede.ull.es/validacion/>

Identificador del documento: 973636 Código de verificación: QpwS3TwF

Firmado por: ARTEMI CAMPS FARIÑA UNIVERSIDAD DE LA LAGUNA	Fecha: 30/06/2017 14:40:15
JOHN E. BECKMAN UNIVERSIDAD DE LA LAGUNA	30/06/2017 15:07:38
JOAN FONT SERRA UNIVERSIDAD DE LA LAGUNA	30/06/2017 15:10:02
ERNESTO PEREDA DE PABLO UNIVERSIDAD DE LA LAGUNA	06/07/2017 13:51:28

the plane and the scale height. As we lack reliable measurements of these in the object under study we performed several simulations, changing the parameters in order best to match observations, until we obtained a satisfactory match with a scale height of 200 pc and a central density of 4 cm^{-3} . These values are not unreasonable, but they are not uniquely determined, an increase in one of them can offset a decrease in the other. The shape of the bubble would be slightly affected by these interchanges, but the effect is not easy to detect when matching the simulation to the observed bubble. The initial simulations were run assuming the thickness of the shell was 1% of its radius, but based on the results from these we deduced that the best value to assign was about 15% of the radius, and this value was used when correcting the quantities in Table 5.1. We also checked that with the revised energy and ISM distributions this thickness to radius ratio was still valid.

5.5.2 Results of the modelling exercise

With the model and the assumptions described in section 5.5.1 we can reproduce well the size and velocity of bubble 1. In Figure 5.2 we show a density cross-section in the XZ plane, as well as a simulated observation in the XY plane and the observed detection for comparison. The effects of the exponential fall-off in gas density perpendicular to the plane are clear, as the bubble is elongated in the Z direction; the density of the shell is also clearly direction dependent.

Figure 5.3 shows a simulated observation in the XY plane and the observed detection for comparison, obtained by projecting the velocity at the point of maximum density in the Z direction, i.e. for each X, Y position we find where the density is maximum along the Z axis and assign the corresponding velocity projected along this axis. The result is very similar to what we observe; not only is the central expansion velocity almost the same (which is the result of the inputs to this specific model) the distribution of observed velocities also follows the pattern displayed in the model of a slow decrease with projected radius before an abrupt fall to zero. This arises from the elongated shape of the superbubble, and should be characteristic of bubbles close to breakout. This model enhances the plausibility of our detection of a superbubble with the measured physical parameters, but we can further test our approximations by deriving the predicted physical parameters of the simulated superbubble, so as to compare them to the observed values.

In Table 5.2 we show a set of parameters for the simulated bubble for two time steps, one corresponding to the closest match in expanding velocity at 4.0 Myr, close to the photometric age of the cluster (3.8 Myr) as given by Whitmore

Este documento incorpora firma electrónica, y es copia auténtica de un documento electrónico archivado por la ULL según la Ley 39/2015.
Su autenticidad puede ser contrastada en la siguiente dirección <https://sede.ull.es/validacion/>

Identificador del documento: 973636 Código de verificación: QpwS3TwF

Firmado por: ARTEMI CAMPS FARIÑA UNIVERSIDAD DE LA LAGUNA	Fecha: 30/06/2017 14:40:15
JOHN E. BECKMAN UNIVERSIDAD DE LA LAGUNA	30/06/2017 15:07:38
JOAN FONT SERRA UNIVERSIDAD DE LA LAGUNA	30/06/2017 15:10:02
ERNESTO PEREDA DE PABLO UNIVERSIDAD DE LA LAGUNA	06/07/2017 13:51:28

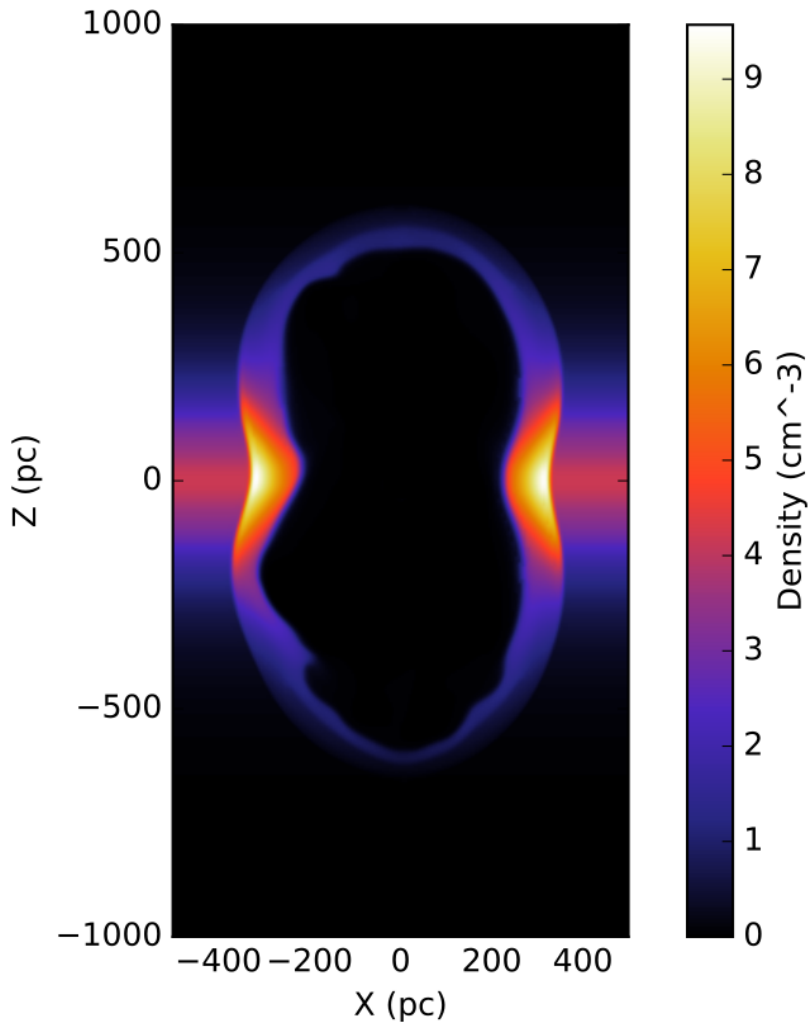


Figure 5.2: Result of the simulation at age 4.0 Myr, the figure represents an XZ slice of the density, showing a distorted shape caused by the density gradient in the disc. The bubble is elongated in the Z axis, following the direction of decrease in density. The density in the shell is also not constant, being much higher for the part expanding into the disc. The linear color scale gives the number density in units of cm^{-3}

Este documento incorpora firma electrónica, y es copia auténtica de un documento electrónico archivado por la ULL según la Ley 39/2015.
Su autenticidad puede ser contrastada en la siguiente dirección <https://sede.ull.es/validacion/>

Identificador del documento: 973636 Código de verificación: QpwS3TwF

Firmado por: ARTEMI CAMPS FARIÑA UNIVERSIDAD DE LA LAGUNA	Fecha: 30/06/2017 14:40:15
JOHN E. BECKMAN UNIVERSIDAD DE LA LAGUNA	30/06/2017 15:07:38
JOAN FONT SERRA UNIVERSIDAD DE LA LAGUNA	30/06/2017 15:10:02
ERNESTO PEREDA DE PABLO UNIVERSIDAD DE LA LAGUNA	06/07/2017 13:51:28

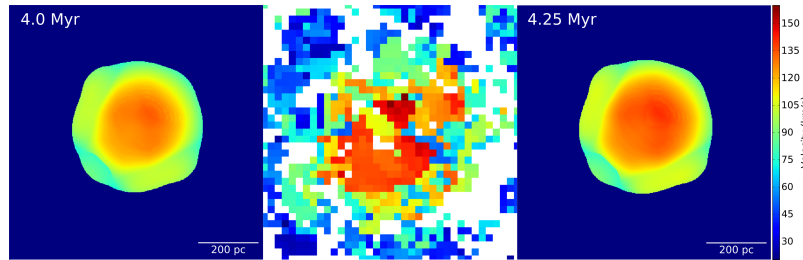


Figure 5.3: Comparison between mock observations of the simulation bubble and the expansion map for this bubble. We show two close time-frames to show the evolution of the bubble appearance in time.

& Zhang (2002) which was the value we used to compute the injection rate, and another 0.25 Myr later, to compare with properties which have evolved with time.

We show also the measured parameters for ease of comparison. The density we observe coincides reasonably well with the density in the centre of the projected shell, but is quite different from the density in XY, the plane of the disc. This could be expected, as the emission we receive comes from the approaching part of the shell. However the discrepancy is carried into the computed mass of the model shell, where there is a considerable difference between this mass and the mass we measure. This is clearly important for the determination of the kinetic energy, as a mass discrepancy translates directly into the same discrepancy factor in the kinetic energy. As it happens, there is a compensating effect because the denser parts of the shell are also significantly slower, and the kinetic energy depends on the square of the velocity. We made the appropriate calculations on the simulation to ascertain the difference made because we observe only the approaching part of the shell. The result was that our observational technique underestimates the mass in the simulation by a factor 2, while the kinetic energy is overestimated by a factor 3. Given that we have used the observed measurement of the kinetic energy as an input to represent the total kinetic energy fed into the bubble, while according to the simulation around half the kinetic energy has been lost by radiation, the current simulation is a really reasonable fit to the data, and accomplishes the basic goal of analyzing the plausibility of the measured parameters for such a superbubble, given the limited data set for any bubble determined at the distance of the Antennae.

The relations between the input physical parameters and those found by performing a mock observation of the simulation results could be used to per-

Table 5.2: Results of the simulation

		Observed	4.0 Myr	4.25 Myr
Radius	(pc)	391	361	378
v_{exp}	(km/s)	132	134	141
n_e (Z)	(cm $^{-3}$)	0.73	1.08	0.97
n_e (XY)	(cm $^{-3}$)		9.49	9.23
E_k	(10 51 erg)	267	151	164
Mass	(10 35 Kg)	31	106	115

Notes. The first column lists the observational properties for bubble 1, the other two correspond to two time steps in the simulation. The radius for the simulation results is taken as half the highest separation of density maxima in XY planes. The expansion velocity refers to the velocity in the Z direction at the centre of the projected bubble. n_e (Z) is the maximum density along the Z axis, we consider this measurement equivalent to the measurement done on the expansion map given the area of the bubble from which we extract the properties. n_e (XY) is the maximum density in the XY axes, corresponding to expansion into the disc, we do not have a measurement of this value from the observational data. It is important to note that the kinetic energy and mass cannot be compared directly as the observational quantity is overestimated for the kinetic energy and the mass is underestimated (see text).

Este documento incorpora firma electrónica, y es copia auténtica de un documento electrónico archivado por la ULL según la Ley 39/2015.
Su autenticidad puede ser contrastada en la siguiente dirección <https://sede.ull.es/validacion/>

Identificador del documento: 973636 Código de verificación: QpwS3TwF

Firmado por: ARTEMI CAMPS FARIÑA UNIVERSIDAD DE LA LAGUNA	Fecha: 30/06/2017 14:40:15
JOHN E. BECKMAN UNIVERSIDAD DE LA LAGUNA	30/06/2017 15:07:38
JOAN FONT SERRA UNIVERSIDAD DE LA LAGUNA	30/06/2017 15:10:02
ERNESTO PEREDA DE PABLO UNIVERSIDAD DE LA LAGUNA	06/07/2017 13:51:28

fect the simulation iteratively until we obtain an exact reproduction of the observed data. While tempting, we admit that this would not enhance the scientific value of the work, as it would in practice be "overfitting" the data. The model is schematic, and among the simplifications we note that we have not taken the supernova kinetic impact directly into account but have imitated this, using winds. We have also assumed a homogeneous ionized ISM, and have not included the presence of molecular clouds or other inhomogeneities. If these could be well characterized by observation we would be able to use the observed kinematic parameters to derive accurate values for the energy injected, and thus constrain the properties of the cluster, but with the available information all we have tried to do is to present some useful semi-quantitative comparisons which put this work in a plausible context.

5.6 Degree of shock-induced ionization

There are two main mechanisms for injecting kinetic energy from stars in a massive stellar cluster into the expanding shell of a superbubble, stellar winds, and supernova explosions. Supernova shocks are far more violent than the continuous input due to fast winds, and this is reflected in the ionization state of a shell produced by each of the mechanisms. Collisional excitation is much more important in supernova remnants, while wind-blown bubbles are photoionized. By spectroscopic examination of the state of ionization of the shell we can try to determine which mechanism currently dominates its excitation, and therefore whether winds or supernovae are the principal contributors to the expansion at the stage when we observe it. For this we use the diagnostic plots from Sabbadin et al. (1977); Garcia Lario et al. (1991) in which the line ratios [SII]/H α and [NII]/H α are used.

The observations were made using long slit spectroscopy with the ISIS spectrograph on the WHT. The slit, with a 1 arcsec width, was placed to cover the overlap zone, including bubbles 1 and 3. A modified version of BUBBLY was run on each of the lines: [SII]₆₇₁₆, [SII]₆₇₃₄, [NII]₆₅₈₄, and H α . The total flux for the [NII] doublet was calculated using the relation [NII]₆₅₈₄=3*[NII]₆₅₄₈ which is virtually independent of the physical parameters of the gas.

In Fig. 5.4 we show the results for the two bubbles and the incoherent region, in which we compare the line intensity ratios for the shells with those for the underlying HII regions. The circles correspond to the HII region flux while the triangles correspond to the shell.

The shell ratios were calculated using the fluxes in the secondary peaks, while the fluxes for the regions were obtained from the central primary peak. We can see from the figure that in all the cases both the shell of the bubble,

Este documento incorpora firma electrónica, y es copia auténtica de un documento electrónico archivado por la ULL según la Ley 39/2015.
Su autenticidad puede ser contrastada en la siguiente dirección <https://sede.ull.es/validacion/>

Identificador del documento: 973636 Código de verificación: QpwS3TwF

Firmado por: ARTEMI CAMPS FARIÑA UNIVERSIDAD DE LA LAGUNA	Fecha: 30/06/2017 14:40:15
JOHN E. BECKMAN UNIVERSIDAD DE LA LAGUNA	30/06/2017 15:07:38
JOAN FONT SERRA UNIVERSIDAD DE LA LAGUNA	30/06/2017 15:10:02
ERNESTO PEREDA DE PABLO UNIVERSIDAD DE LA LAGUNA	06/07/2017 13:51:28

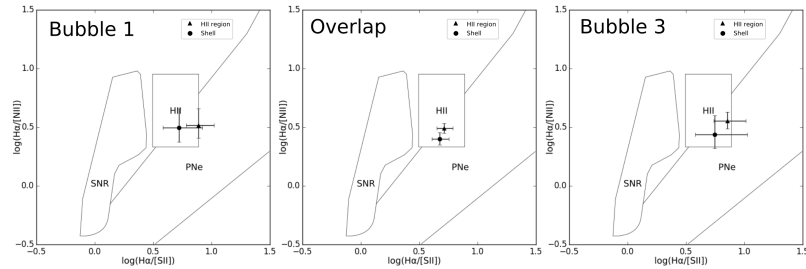


Figure 5.4: Identification diagrams used to distinguish between supernova remnants, HII regions and planetary nebulae. We present measurements of shell (triangles) and main peak (circle) ratios for bubbles 1 and 3, as well as the overlap region. All the shells are clearly placed within the limits of the HII region area, meaning that at this stage they are primarily ionized by radiation, rather than supernova shocks. It is interesting to note, though, that they all fall closer to the supernova remnant area than their corresponding HII region emission.

and the HII region show ratios well within the zone of the diagram which characterizes an HII region, showing that photoionization is currently dominant compared with shock-induced ionization. The points for the shells are, however, clearly somewhat nearer to the SNR zone, which implies a somewhat greater role for shocks in the shells than in the bodies of the HII regions. This result is what one would expect, given the masses and the evolutionary stages of all our observed bubbles. A supernova remnant has masses of order a few solar masses, while our bubbles have accumulated many thousands of solar masses, as well as having had time to relax from initial supernova shocks. At this stage, the addition of an additional supernova remnant expanding into the shell would not have a strong effect on its ionization state.

5.7 Comparison with HST

The hydrodynamic simulation shows that it is plausible to expect superbubbles with the physical parameters we have measured, but for this object we can do better in the assessment of the validity of our results. There are existing archival narrowband H α images taken with the Hubble Space Telescope of the Antennae, which allow us to compare our detections with images at a spatial resolution capable of resolving the shells. The images were taken from the ESA HST archive, and were observed with the filter F658N. We examined the image to match structure observed in the gas to our detections, as well as see if there are any shells visible in the HST image that were missed with our method.

Este documento incorpora firma electrónica, y es copia auténtica de un documento electrónico archivado por la ULL según la Ley 39/2015.
Su autenticidad puede ser contrastada en la siguiente dirección <https://sede.ull.es/validacion/>

Identificador del documento: 973636

Código de verificación: QpwS3TwF

Fecha: 30/06/2017 14:40:15

Firmado por: ARTEMI CAMPS FARÍÑA
UNIVERSIDAD DE LA LAGUNA

JOHN E. BECKMAN
UNIVERSIDAD DE LA LAGUNA

JOAN FONT SERRA
UNIVERSIDAD DE LA LAGUNA

ERNESTO PEREDA DE PABLO
UNIVERSIDAD DE LA LAGUNA

30/06/2017 15:07:38

30/06/2017 15:10:02

06/07/2017 13:51:28

In figure 5.5 we present some examples of a comparison between the expansion map and the HST image, we show two clear cases where the bubble is detected in both the expansion map and the HST image, as well as a more uncertain case which does show filaments of gas that could be associated with expansion, but no clear shell. Finally, we also present two shells visible in the HST image which were not clearly detected in BUBBLY. A possible reason for this is that our program relies on kinematic detection, so bubbles in advanced evolutionary stages which have very low velocities or shell densities will be missed, whereas narrowband imaging which detects the projected outer ring (undetectable in kinematics) will succeed.

5.8 Summary and conclusions

- We applied BUBBLY, a program sensitive to the presence of expanding shells to a Fabry-Pérot observation of the Antennae pair of galaxies mapping the H α emission line. The program detects and fits multiple components to the H α line profile, for which the data obtained with GHaFaS is ideal given its high kinematic (8 km s^{-1}) and spatial (seeing-limited) resolution.
- Using a map of the detected expansion we report the presence of 17 superbubbles associated with most of the brightest HII regions in the object. We estimate the sizes, expansion velocities and luminosities of the superbubbles and use these quantities to derive their shell density, mass, kinetic energy and age. The bubbles range between $\sim 150\text{-}500 \text{ pc}$ in radius, with low shell densities and kinetic energy between a dozen and a few hundred supernovae. We use age determinations from the literature for the young clusters in this object and find that many of our bubbles have a matching age determination of a similar value, taking into account that the age we present is a lower limit assuming free expansion.
- The expansion map shows not only the superbubbles but also extended detections which cover most of the galaxy and do not show enough spatial coherence to be identified as superbubbles. Nevertheless, given that their expansion velocities are generally on the low side they should not originate in noise, but rather in spatially unresolved clusters. We make an estimate of the kinetic energy contained in this unresolved expansion with several approximations and find that it is of the same order as the energy in the bubbles, meaning that the biggest HII regions do not dominate the kinetic energy budget in this object.

Este documento incorpora firma electrónica, y es copia auténtica de un documento electrónico archivado por la ULL según la Ley 39/2015.
Su autenticidad puede ser contrastada en la siguiente dirección <https://sede.ull.es/validacion/>

Identificador del documento: 973636

Código de verificación: QpwS3TwF

Fecha: 30/06/2017 14:40:15

Firmado por: ARTEMI CAMPS FARIÑA
 UNIVERSIDAD DE LA LAGUNA

JOHN E. BECKMAN
 UNIVERSIDAD DE LA LAGUNA

JOAN FONT SERRA
 UNIVERSIDAD DE LA LAGUNA

ERNESTO PEREDA DE PABLO
 UNIVERSIDAD DE LA LAGUNA

30/06/2017 15:07:38

30/06/2017 15:10:02

06/07/2017 13:51:28

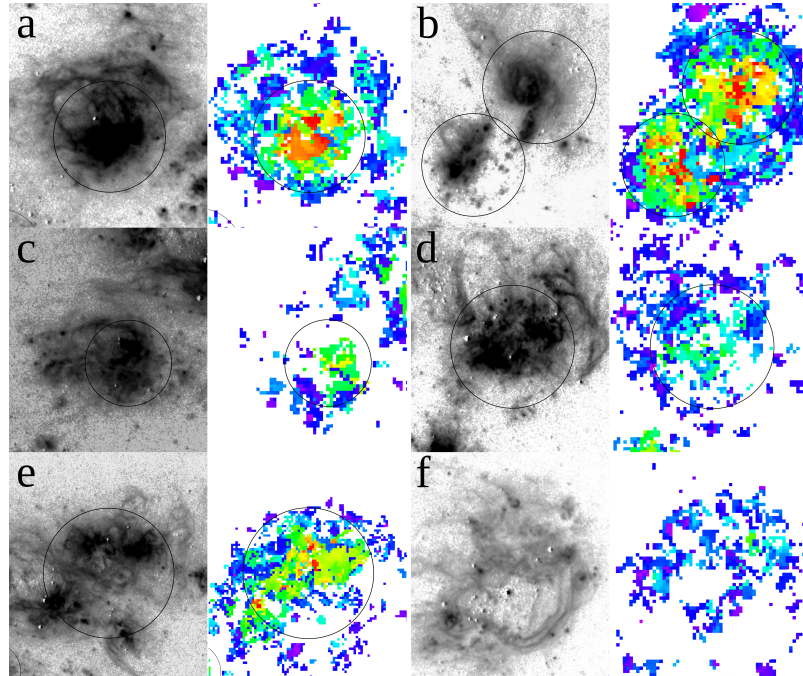


Figure 5.5: Comparison between our detections in the expansion map and the high resolution H α images taken by Hubble. The two top panels show clear agreement between the detections, with visible shells matching the expansion map. Panels c-f show other superbubbles with less clear HST detections, although filamentary structures characteristic of winds and supernovae working the ISM can be seen. The two bottom panels show structure missed by BUBBLY, on the left a clear shell seen in HST is not clear enough to warrant detection in the expansion map, while the right panel shows small HII regions which have some high velocity expansion detected at the centres but not enough spatial coverage to be accepted as proper detections.

Este documento incorpora firma electrónica, y es copia auténtica de un documento electrónico archivado por la ULL según la Ley 39/2015.
Su autenticidad puede ser contrastada en la siguiente dirección <https://sede.ull.es/validacion/>

Identificador del documento: 973636

Código de verificación: QpwS3TwF

Firmado por: ARTEMI CAMPS FARIÑA
UNIVERSIDAD DE LA LAGUNA

Fecha: 30/06/2017 14:40:15

JOHN E. BECKMAN
UNIVERSIDAD DE LA LAGUNA

30/06/2017 15:07:38

JOAN FONT SERRA
UNIVERSIDAD DE LA LAGUNA

30/06/2017 15:10:02

ERNESTO PEREDA DE PABLO
UNIVERSIDAD DE LA LAGUNA

06/07/2017 13:51:28

- To assess the validity of our results and check for bias in the determination of the physical properties we use hydrodynamic simulations to reproduce one of our bubbles using the physical parameters as inputs. We manage to reproduce a bubble with similar observational properties. Projecting the simulation into a mock expansion map as our program would observe it shows a remarkably similar distribution of velocities due to projection effects, showing a slow decrease in observed expansion velocity before cutting off. This arises from the non-spherical shape of the bubble induced by the density profile of the disk.
- The simulation also serves to check for bias in the physical parameter determination with our method, as we only probe the thinner, faster part of the shell which approaches us. We find that in this case the kinetic energy is overestimated by a factor 3 while the mass is underestimated by a factor 2.
- We also use long-slit observations of HII regions along the overlap zone to probe the ionization mechanisms in the expanding shells. A diagnostic on the ratio of forbidden lines $[\text{SII}]_{6716,6734}$ and $[\text{NII}]_{6584}$ to $\text{H}\alpha$ shows that photoionization dominates this process, though the forbidden line ratios are higher for the shells rather than the bulk of the HII region, showing that collisional excitation is more important in the shells.

Este documento incorpora firma electrónica, y es copia auténtica de un documento electrónico archivado por la ULL según la Ley 39/2015.
Su autenticidad puede ser contrastada en la siguiente dirección <https://sede.ull.es/validacion/>

Identificador del documento: 973636 Código de verificación: QpwS3TwF

Firmado por: ARTEMI CAMPS FARIÑA UNIVERSIDAD DE LA LAGUNA	Fecha: 30/06/2017 14:40:15
JOHN E. BECKMAN UNIVERSIDAD DE LA LAGUNA	30/06/2017 15:07:38
JOAN FONT SERRA UNIVERSIDAD DE LA LAGUNA	30/06/2017 15:10:02
ERNESTO PEREDA DE PABLO UNIVERSIDAD DE LA LAGUNA	06/07/2017 13:51:28

Este documento incorpora firma electrónica, y es copia auténtica de un documento electrónico archivado por la ULL según la Ley 39/2015.
Su autenticidad puede ser contrastada en la siguiente dirección <https://sede.ull.es/validacion/>

Identificador del documento: 973636

Código de verificación: QpwS3TwF

Firmado por: ARTEMI CAMPS FARIÑA
UNIVERSIDAD DE LA LAGUNA

Fecha: 30/06/2017 14:40:15

JOHN E. BECKMAN
UNIVERSIDAD DE LA LAGUNA

30/06/2017 15:07:38

JOAN FONT SERRA
UNIVERSIDAD DE LA LAGUNA

30/06/2017 15:10:02

ERNESTO PEREDA DE PABLO
UNIVERSIDAD DE LA LAGUNA

06/07/2017 13:51:28

6

Arp 70: An interacting galaxy with extreme outflows

6.1 Introduction

Arp 70 (also known as VV341) is an interacting pair of galaxies, considered by Laurikainen et al. (1998) to be 'M51-type': A larger galaxy with two well-defined spiral arms interacting with a small companion in its vicinity. These systems are likely to have mass exchange and the interaction with a small companion has been linked to the production of grand-design spiral arms (Salo & Laurikainen (1993); Donner & Thomasson (1994)). The larger galaxy with the spiral arms is denominated Arp 70b, while the smaller companion is Arp 70a. All the results presented in this chapter correspond to Arp70b.

This object has not been studied deeply and in most literature it appears as part of a sample of M51-type galaxies whose properties are analysed statistically. Laurikainen et al. (1998); Laurikainen & Salo (2000, 2001) studied the photometric properties of a sample of M51-type galaxies in the BVRI bands, while Rampazzo et al. (2005) and Gunthardt et al. (2016) analysed the kinematic properties of similar samples, the former using Fabry-Pérot data (on which this chapter is based) and the latter on long-slit observations. Holincheck et al. (2016) obtained dynamical models for a sample of 62 interacting pairs of galaxies by matching models to observations, which were obtained thanks to citizen collaboration as part of the *Galaxy Zoo* project.

In this chapter we report the discovery of two distinct outflows in one galaxy, both of which having extreme values scale and physical parameters compared to the previous bubbles presented in this thesis. One of them is found in the

centre of the galaxy, which appears to house an active supermassive black hole, while the other is a giant HII region housing an enormous expanding shell.

6.2 Data

For this object we do not have observations obtained with GH α FaS, unlike the other galaxies in this thesis. Instead, we use a cube from another Fabry-Pérot (FP) instrument, CIGALE, which we obtained from a repository for FP data. The *Fabry-Perot database*¹ is operated by the *Centre de donnéeS Astrophysiques de Marseille* (CeSAM), which is affiliated with the *Laboratoire d'Astrophysique de Marseille* (LAM). They offer data from several surveys including reduced products such as moment maps, continuum, and even rotation curves in some cases.

The observations of Arp 70 were performed with CIGALE at the SAO 6m telescope in Russia on October 1994, and they are reported in Rampazzo et al. (2005). The instrument has a field of view of 3.58 x 3.58 arcmin and a pixel size of 0.84 arcsec, with a 256 x 256 pixel detector. In the spectral dimension it has a spectral range of 599 km s⁻¹ with 32 scanning steps. The spectral resolution for the H α line is about 30 km s⁻¹.

Additionally, we also obtained a spectrum for the centre of the galaxy from the SDSS archive, which was obtained with the BOSS spectrograph on the eponymous survey (Baryon Oscillation Spectroscopic Survey). The spectrum fiber subtends 2 arcsec on the sky and has a spectral range of 360 - 1000 nm, with a spectral resolution between 1850 - 2650 in the red channel, which translates to between 113 - 162 km s⁻¹.

6.2.1 Reduction

The data we obtain from the respective archives is already reduced for the most part, but we required some additional processing for our purposes. The CIGALE cube is wavelength calibrated, but does not have flux calibration. We did not find archival H α images which would be the natural reference to calibrate the cube, so instead we used the SDSS spectrum to do so. The flux contained in the spectrum corresponds to a 2 arcsec circular window situated at the centre of the galaxy. We need to find an equivalence between the flux of this area in both instruments and, given that the fibre diameter is comparable to the pixel size (0.84") we cannot approximate it as a number of pixels. To obtain the flux in CIGALE units we projected the fibre area onto the cube

¹<http://cesam.lam.fr/fabryperot/>

and calculated the intersected area for each pixel, that is, the percentage of the pixel that falls within the fibre. We then sum the spectrum in each pixel weighted by this factor, and therefore obtain a reasonable approximation of the spectrum equivalent to the SDSS data in this spectral range. We calculate the equivalence in flux between the fitted main peaks of each spectrum, the reason for not simply taking the entirety of the flux in the shared spectral range is that we believe that flux from higher orders appears in the Fabry-Pérot data, this will be justified in the results section.

The SDSS data are fully calibrated, but in order to improve the detection and fitting of additional components we subtracted a model of the stellar continuum, which allowed for a clear detection of these components.

We fitted the continuum with the *Penalized Pixel Fitting method* (pPXF), a widely used tool to study the stellar properties of galaxies by fitting template spectra to observations (Cappellari & Emsellem (2004); Cappellari (2017)). This program uses a library of stellar spectra as templates of the emission and finds the linear combination of these that correctly fits the observed spectrum. The results are used to infer the stellar populations of a galaxy and their kinematics, taking advantage of the large number of features considered in the fit to obtain a much better velocity resolution than if we used just a few strong lines.

We used the *Indo-U.S. Coudé Feed Spectral Library*² as templates to perform the fit (Valdes et al. (2004)). This library consists of spectra for 1273 stars obtained with the 0.9 Coudé Feed telescope, located at Kitt Peak National Observatory. We are mostly interested in the H α , [NII], [SII] and [OI] lines, so we performed the fit for the range of 550–750 nm, obtaining a satisfactory model to subtract from the spectrum. In Figure 6.1 we show the spectrum and the resulting model.

In our calculation of the calibration value described previously we did not use the stellar continuum subtracted model, as this model calculates stellar absorption of the H α line, which is apparent in Fig. 6.1. The calibration value is instrumental and we need to compare the observed fluxes, so unless we can perform the same H α flux correction in the CIGALE cube we would be misrepresenting the observed flux in the SDSS spectrum. Because of this we estimated a constant continuum value for H α instead and compared only the measured fluxes, without stellar modelling.

²<https://www.noao.edu/cfclib/>

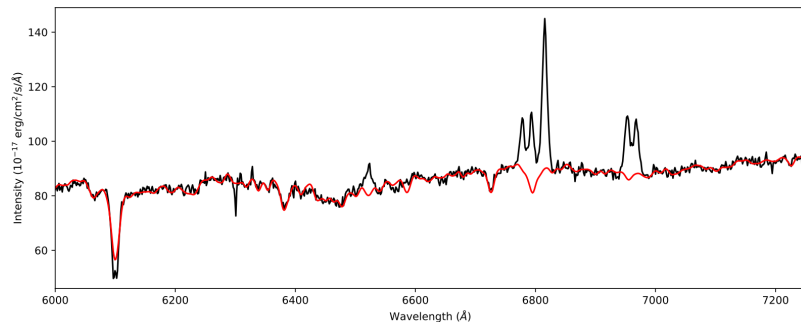


Figure 6.1: SDSS spectrum in the 550 - 750 nm (black) with the fitted stellar model overlaid (red).

6.3 Results

This galaxy initially drew interest over a detected superbubble in an HII region in the spiral arm of the galaxy, but upon inspecting the central area of the galaxy we found a striking feature of three peaks with similar fluxes and equidistant, with the central one being consistent with the velocity field of the galaxy (See Fig. 6.2). We will first present the results obtained for this feature and later show the properties of the aforementioned superbubble.

6.3.1 Outflow detection

The relative flux of the secondary peaks is very high, so the magnitude of the outflow in terms of ejected mass and energy must be similarly large which, coupled with the location at the centre of the galaxy, immediately reminds us of the characteristics of an AGN, with one caveat: owing to the high power nature of AGN the outflows they produce have typically high velocities, of order 500-1000 km s $^{-1}$ and up to several thousands of km s $^{-1}$. Our detection, however, has a very slow velocity of about 90 km s $^{-1}$ which is an anomalously low value. A possible solution to this lies in the cyclical nature of Fabry-Pérot instruments: each channel does not correspond to a single wavelength value, but to a set of wavelengths separated by one free spectral range (FSR), so that by sweeping over the full FSR we measure all wavelengths. This behaviour is prevented in practice by the use of a narrowband filter, which allows only the emission from the H α line to pass to the instrument. This width is still typically higher than the FSR, so if the galaxy has a steep gradient in observed velocity

Este documento incorpora firma electrónica, y es copia auténtica de un documento electrónico archivado por la ULL según la Ley 39/2015.
Su autenticidad puede ser contrastada en la siguiente dirección <https://sede.ull.es/validacion/>

Identificador del documento: 973636 Código de verificación: QpwS3TwF

Firmado por: ARTEMI CAMPS FARÍÑA UNIVERSIDAD DE LA LAGUNA	Fecha: 30/06/2017 14:40:15
JOHN E. BECKMAN UNIVERSIDAD DE LA LAGUNA	30/06/2017 15:07:38
JOAN FONT SERRA UNIVERSIDAD DE LA LAGUNA	30/06/2017 15:10:02
ERNESTO PEREDA DE PABLO UNIVERSIDAD DE LA LAGUNA	06/07/2017 13:51:28

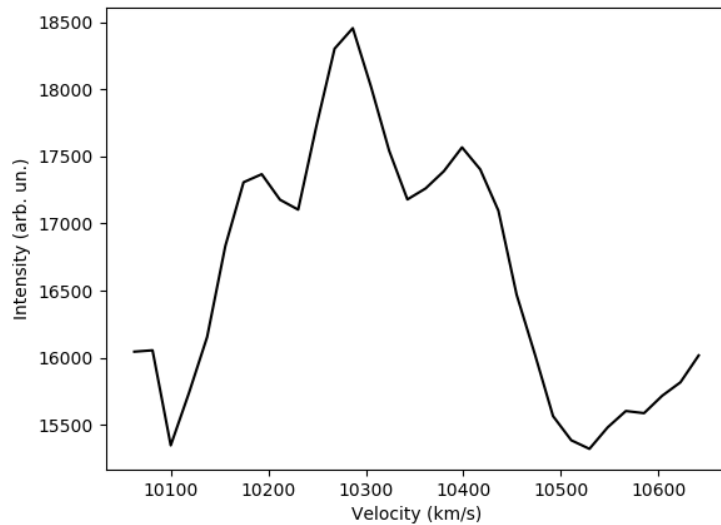


Figure 6.2: Spectrum of the central region of Arp 70b from the CIGALE data cube, showing an extreme version of the expansion signature.

Este documento incorpora firma electrónica, y es copia auténtica de un documento electrónico archivado por la ULL según la Ley 39/2015.
Su autenticidad puede ser contrastada en la siguiente dirección <https://sede.ull.es/validacion/>

Identificador del documento: 973636 Código de verificación: QpwS3TwF

Firmado por: ARTEMI CAMPS FARIÑA UNIVERSIDAD DE LA LAGUNA	Fecha: 30/06/2017 14:40:15
JOHN E. BECKMAN UNIVERSIDAD DE LA LAGUNA	30/06/2017 15:07:38
JOAN FONT SERRA UNIVERSIDAD DE LA LAGUNA	30/06/2017 15:10:02
ERNESTO PEREDA DE PABLO UNIVERSIDAD DE LA LAGUNA	06/07/2017 13:51:28

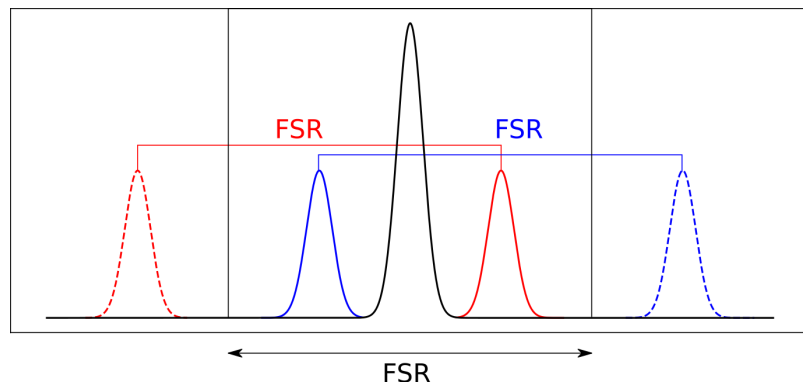


Figure 6.3: Diagram illustrating the effect of jumping an order on the position at which a peak appears on the spectrum of a Fabry-Pérot instrument. The dashed red and blue peaks are the true emission peaks that lie out of our spectral range, while the solid lines are the observed ones. The box indicates the spectral window of our instrument, spanning one Free Spectral Range (FSR). The effect of jumping an order is that the peak appears on the other end of the spectrum, shifted one FSR from its actual position. This property allows us to determine the true position of the peak.

(such as those with a high inclination) the emission can 'jump orders' and appear on one end of the spectrum as it disappears on the other. Sometimes emission from nearby [NII] lines can also leak if the filter is not narrow enough.

This opens a possibility, that the secondary peaks are not actually separated by 90 km s^{-1} but that they lie in a higher and lower order each, significantly increasing the velocity separation. If this is the case the symmetry respect to the central peak would not be affected, provided that both peaks have jumped an order. If we apply this correction the observed expansion velocity of the peaks then becomes $\sim 500 \text{ km s}^{-1}$, which is in much better agreement with the expected value for an AGN.

We illustrate the effect and the resulting change in expansion velocity from jumping an order in Figure 6.3.

The outflow is also detected in the SDSS spectrum in several lines, in Figure 6.4 we show the H α , [NII], [SII] and [OI] lines, in which we can appreciate the presence of additional components associated with expansion in H α and [NII] $_{6584}$. The [SII] doublet also shows an additional component between the peaks, this might be the result of both peaks having faint expansive components which can only be detected in the middle as the approaching and receding emission from each [SII] peak overlap doubling the flux.

Este documento incorpora firma electrónica, y es copia auténtica de un documento electrónico archivado por la ULL según la Ley 39/2015.
Su autenticidad puede ser contrastada en la siguiente dirección <https://sede.ull.es/validacion/>

Identificador del documento: 973636

Código de verificación: QpwS3TwF

Fecha: 30/06/2017 14:40:15

Firmado por: ARTEMI CAMPS FARÍÑA
UNIVERSIDAD DE LA LAGUNA

JOHN E. BECKMAN
UNIVERSIDAD DE LA LAGUNA

JOAN FONT SERRA
UNIVERSIDAD DE LA LAGUNA

ERNESTO PEREDA DE PABLO
UNIVERSIDAD DE LA LAGUNA

30/06/2017 15:07:38

30/06/2017 15:10:02

06/07/2017 13:51:28

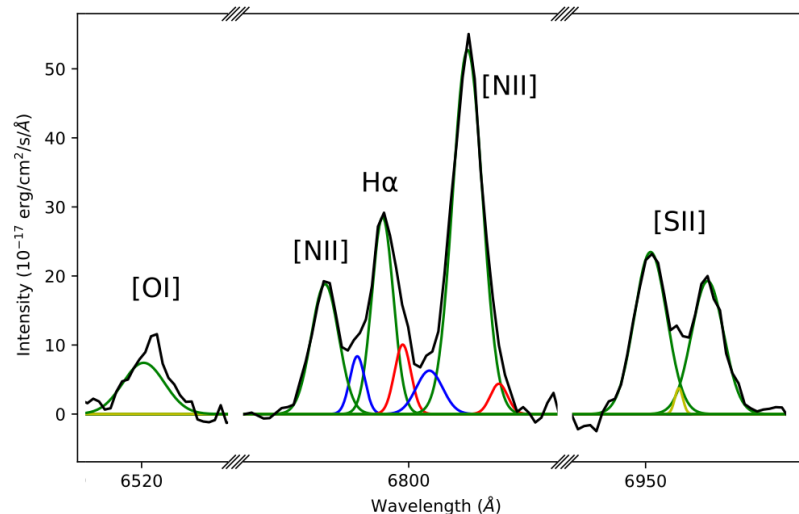


Figure 6.4: SDSS spectrum for $\text{H}\alpha$, [NII] and [SII], showing the additional components detected for each, we see expanding components detected in $\text{H}\alpha$ and $[\text{NII}]_{6584}$, as well as an additional component between the peaks of the [SII] doublet.

Este documento incorpora firma electrónica, y es copia auténtica de un documento electrónico archivado por la ULL según la Ley 39/2015.
Su autenticidad puede ser contrastada en la siguiente dirección <https://sede.ull.es/validacion/>

Identificador del documento: 973636

Código de verificación: QpwS3TwF

Firmado por: ARTEMI CAMPS FARIÑA
UNIVERSIDAD DE LA LAGUNA

Fecha: 30/06/2017 14:40:15

JOHN E. BECKMAN
UNIVERSIDAD DE LA LAGUNA

30/06/2017 15:07:38

JOAN FONT SERRA
UNIVERSIDAD DE LA LAGUNA

30/06/2017 15:10:02

ERNESTO PEREDA DE PABLO
UNIVERSIDAD DE LA LAGUNA

06/07/2017 13:51:28

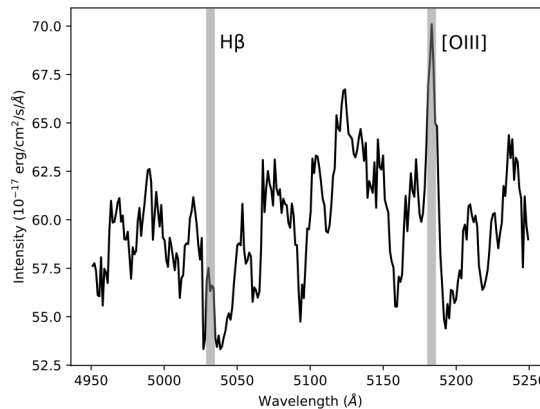


Figure 6.5: SDSS spectrum for the [OIII] and H β lines. We can see that [OIII] is detected, albeit weak, but H β is not. This spectrum has not been continuum model subtracted.

In Table 6.1 we show the properties of the detected components of these emission lines. The secondary lines are shown with their velocity offset from the main line, and we see that the previous hypothesis that the detected peaks correspond to different orders is confirmed by the measured expansion velocity in both lines, as the expansion velocities are closer to the value obtained when correcting for the FSR jump.

We can use these emission lines to test the nature of the object by plotting line ratios on a BPT diagram (Baldwin et al. (1981)), which distinguishes between the emission from HII-like objects and AGN using the strength of H β versus [OIII] and the ratio between H α and [NII], [SII] or [OI]. On the SDSS spectrum we do detect a faint [OIII] line, but the H β line is undetected (see Fig. 6.5).

In Figure 6.6 we show the identification of the object, which clearly lies in the zone for AGN for all of the diagnostic plots. The lack of an H β detection prevents us from identifying whether the AGN is a Seyfert galaxy or a LINER. In spite of this, based on the moderate width of the emission lines and the weakness of the [OIII] line we believe that this object to be a LINER.

Next we will take a look at the spatial distribution of the emission in the CIGALE data cube. To do so we have produced a map showing the spectrum corresponding to each point in a 7x7 pixel square (see Fig. 6.7). On the figure we see that while in the central zone both peaks are detected with similar fluxes,

Este documento incorpora firma electrónica, y es copia auténtica de un documento electrónico archivado por la ULL según la Ley 39/2015.
Su autenticidad puede ser contrastada en la siguiente dirección <https://sede.ull.es/validacion/>

Identificador del documento: 973636

Código de verificación: QpwS3TwF

Fecha: 30/06/2017 14:40:15

Firmado por: ARTEMI CAMPS FARÍÑA
UNIVERSIDAD DE LA LAGUNA

JOHN E. BECKMAN
UNIVERSIDAD DE LA LAGUNA

JOAN FONT SERRA
UNIVERSIDAD DE LA LAGUNA

ERNESTO PEREDA DE PABLO
UNIVERSIDAD DE LA LAGUNA

30/06/2017 15:07:38

30/06/2017 15:10:02

06/07/2017 13:51:28

Table 6.1: Emission lines from the SDSS spectrum

		Wavelength (nm)	V_{exp} (km/s)	Flux (10^{-17} erg/cm 2 /s)	Luminosity (10^{39} erg/s)	σ (nm)	σ (km/s)
$\text{H}\alpha$	main	679.32 ± 0.06		198 ± 68	4.7 ± 1.6	0.28 ± 0.09	122 ± 41
	approaching	678.67 ± 0.08	-289 ± 46	40 ± 24	1.0 ± 0.6	0.19 ± 0.08	86 ± 37
	receding	679.84 ± 0.06	230 ± 38	54 ± 22	1.3 ± 0.5	0.21 ± 0.09	94 ± 41
$[\text{NII}]_{6549}$	main	677.83 ± 0.03		167 ± 16	4.0 ± 0.4	0.35 ± 0.03	156 ± 13
	approaching	681.53 ± 0.02		506 ± 111	12 ± 3	0.38 ± 0.05	169 ± 22
	receding	680.54 ± 0.14	-436 ± 63	54 ± 34	1.3 ± 0.8	0.34 ± 0.15	151 ± 66
$[\text{NII}]_{6583}$	main	682.34 ± 0.11	357 ± 51	24 ± 15	0.6 ± 0.4	0.2 ± 0.1	97 ± 42
	approaching						
	receding						
$[\text{SII}]_{6717}$	main	695.31 ± 0.01		247 ± 11	5.9 ± 0.3	0.42 ± 0.02	181 ± 7
	main	696.79 ± 0.02		201 ± 11	4.8 ± 0.3	0.42 ± 0.02	179 ± 8
	middle	696.04 ± 0.04		10 ± 4	0.23 ± 0.08	0.10 ± 0.04	45 ± 20
$[\text{SII}]_{6731}$	main	652.04 ± 0.04		101 ± 13	2.4 ± 0.3	0.54 ± 0.04	249 ± 18
	main						
	middle						
$[\text{OI}]$	main	652.04 ± 0.04					
	main						
	middle						

Notes. Properties of emission lines in the SDSS spectrum. They are grouped by parent line for the cases of $\text{H}\alpha$ and $[\text{NII}]_{6583}$, which show expanding components, and for $[\text{SII}]$, where we detect an additional component but cannot distinguish to which line in the doublet it corresponds. We also show expansion velocities only for those secondary components that are clearly associated with a parent emission line.

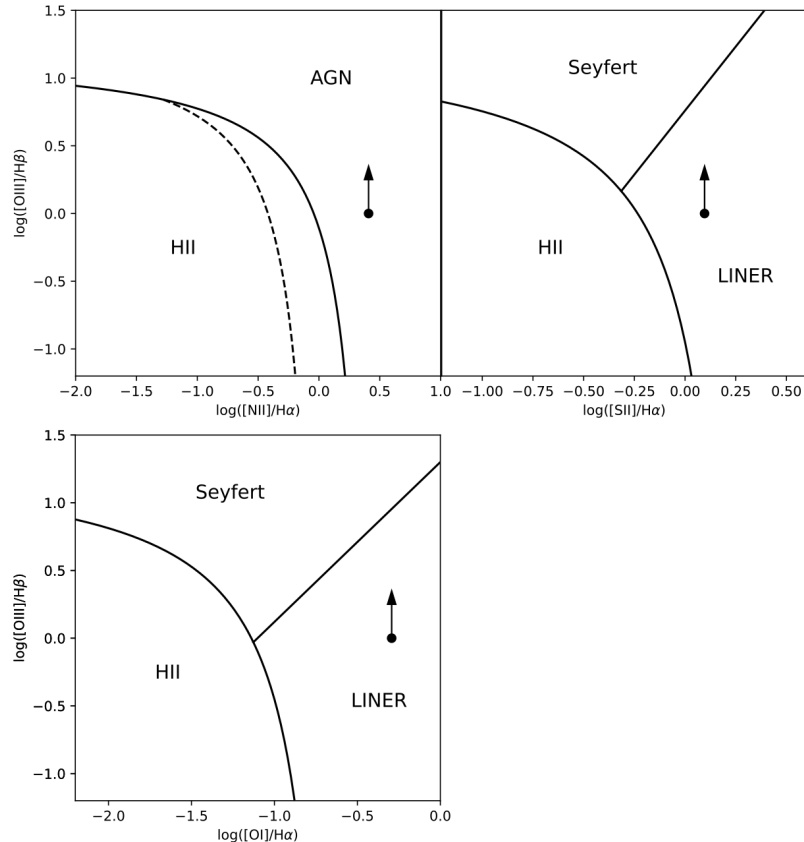


Figure 6.6: Figure showing the position of our object in a BPT diagram, clearly showing the it corresponds to an AGN. The $\text{H}\beta$ line has not been detected, so on account of [OIII] actually being detected we imposed an lower limit to the $[\text{OIII}]/\text{H}\beta$ ratio of 1, which corresponds to zero in the logarithmic scale of the figure.

Este documento incorpora firma electrónica, y es copia auténtica de un documento electrónico archivado por la ULL según la Ley 39/2015.
Su autenticidad puede ser contrastada en la siguiente dirección <https://sede.ull.es/validacion/>

Identificador del documento: 973636

Código de verificación: QpwS3TwF

Firmado por: ARTEMI CAMPS FARIÑA
UNIVERSIDAD DE LA LAGUNA

Fecha: 30/06/2017 14:40:15

JOHN E. BECKMAN
UNIVERSIDAD DE LA LAGUNA

30/06/2017 15:07:38

JOAN FONT SERRA
UNIVERSIDAD DE LA LAGUNA

30/06/2017 15:10:02

ERNESTO PEREDA DE PABLO
UNIVERSIDAD DE LA LAGUNA

06/07/2017 13:51:28

if we go towards the left the approaching peak rapidly becomes dominant, eventually becoming brighter than the central peak, while the same happens to the receding peak when we go towards the right. It is also apparent that the outflow peaks are detected at the same wavelength, that is, they do not exhibit projection effects. Both of these properties are characteristic of a conical jet-like outflow which is inclined from the line of sight. Since the gas travels in a straight line there will be no change in the relative orientation with respect to the observer, and therefore the velocity offset will not change. It bears mention that the apparent "approaching" and "receding" peaks actually are switched from the actual ones, that is, the peak that appears blue-shifted is actually red-shifted and vice-versa. This is because the peaks have jumped an order as described above, which makes them appear at the opposite side of the spectrum. Jet-like outflows are typical in AGN, so this also fits the identification.

6.3.2 Physical properties

We will calculate the relevant physical parameters in a similar manner as we did for the bubbles detected in the other galaxies, but some of the approximations are not valid any more. The expanding object is no longer sphere-like, but instead consists of two aligned cones of ejected material. The general form of the equation relating luminosity to density in H α is:

$$L_{H\alpha} = 4\pi V n_e^2 \alpha(H, T) h\nu \quad (6.1)$$

We used to approximate the volume of the shell V as $4\pi R^2 \Delta R$, the formula for the volume of cone is:

$$V = \frac{1}{3}\pi r^2 h \quad (6.2)$$

Where r is the radius of the circular base and h is the height. What we observe, however, is a projected cone and therefore these quantities cannot be measured directly. The base of the cone will become an ellipse upon projecting, from which we can obtain the value of r as it is equal to half the major axis of the ellipse. The height h is calculated from its projected value l , which depends on the inclination of the cone with respect to the line of sight as $l = h \cos\theta$, where θ is the inclination angle (at 0° l and h coincide). We obtained the projected shape of the cone by analysing the spatial distribution of the outflow peaks, we show the observed sides and major axis of the base in Figure 6.8.

The only parameter missing is the angle of the outflow with respect to the observer, but unfortunately we do not have any way of measuring its value. Because of this we have calculated all the physical properties for three representative angle values at 30°, 45° and 60°. We do not include 0° or 90° inclinations

Este documento incorpora firma electrónica, y es copia auténtica de un documento electrónico archivado por la ULL según la Ley 39/2015.
Su autenticidad puede ser contrastada en la siguiente dirección <https://sede.ull.es/validacion/>

Identificador del documento: 973636 Código de verificación: QpwS3TwF

Firmado por: ARTEMI CAMPS FARIÑA UNIVERSIDAD DE LA LAGUNA	Fecha: 30/06/2017 14:40:15
JOHN E. BECKMAN UNIVERSIDAD DE LA LAGUNA	30/06/2017 15:07:38
JOAN FONT SERRA UNIVERSIDAD DE LA LAGUNA	30/06/2017 15:10:02
ERNESTO PEREDA DE PABLO UNIVERSIDAD DE LA LAGUNA	06/07/2017 13:51:28

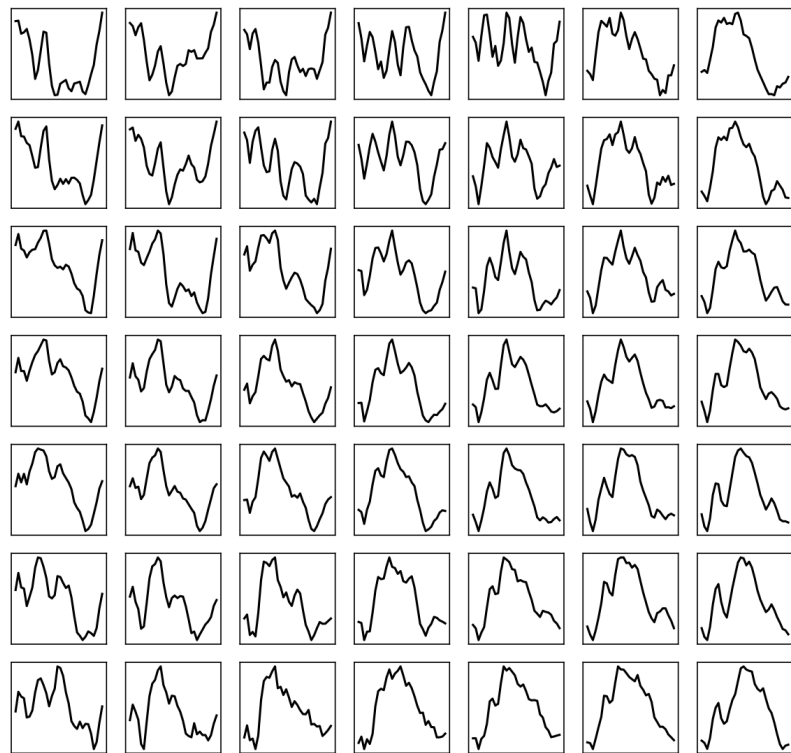


Figure 6.7: Figure showing the spatial distribution of the spectral emission from the CIGALE cube by plotting the individual spectra for each point at its spatial position.

Este documento incorpora firma electrónica, y es copia auténtica de un documento electrónico archivado por la ULL según la Ley 39/2015.
Su autenticidad puede ser contrastada en la siguiente dirección <https://sede.ull.es/validacion/>

Identificador del documento: 973636

Código de verificación: QpwS3TwF

Firmado por: ARTEMI CAMPS FARIÑA
UNIVERSIDAD DE LA LAGUNA

Fecha: 30/06/2017 14:40:15

JOHN E. BECKMAN
UNIVERSIDAD DE LA LAGUNA

30/06/2017 15:07:38

JOAN FONT SERRA
UNIVERSIDAD DE LA LAGUNA

30/06/2017 15:10:02

ERNESTO PEREDA DE PABLO
UNIVERSIDAD DE LA LAGUNA

06/07/2017 13:51:28

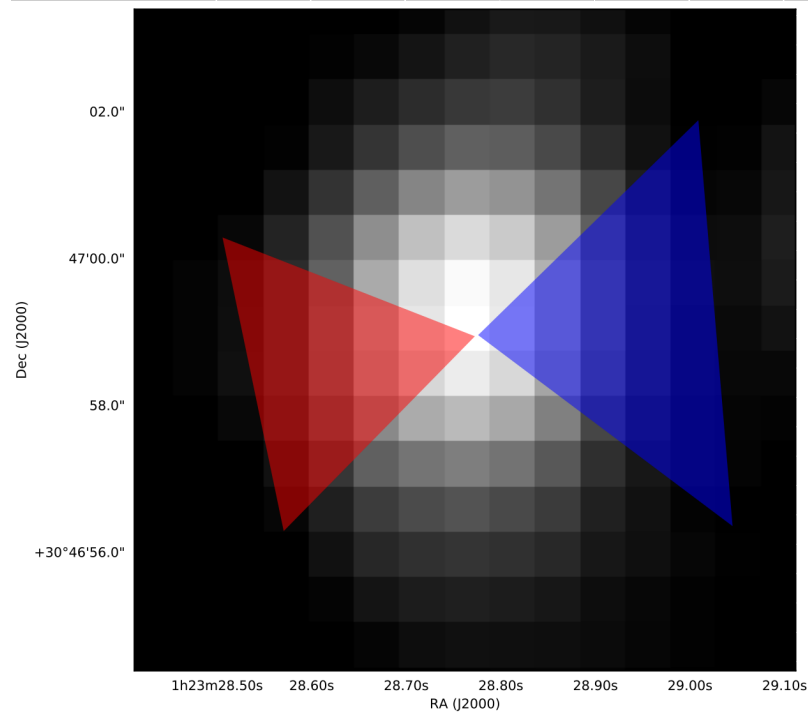


Figure 6.8: Figure showing the estimated cone shapes of the approaching and receding cones. The left cone corresponds to the receding part of the outflow and the right one the approaching part. This identification might seem at odds with Figure 6.7, where the outflow peaks suggest the opposite distribution of approaching and receding outflows, but they are actually switched as a result of the FSR jump described in the text.

Este documento incorpora firma electrónica, y es copia auténtica de un documento electrónico archivado por la ULL según la Ley 39/2015.
Su autenticidad puede ser contrastada en la siguiente dirección <https://sede.ull.es/validacion/>

Identificador del documento: 973636 Código de verificación: QpwS3TwF

Firmado por: ARTEMI CAMPS FARÍÑA UNIVERSIDAD DE LA LAGUNA	Fecha: 30/06/2017 14:40:15
JOHN E. BECKMAN UNIVERSIDAD DE LA LAGUNA	30/06/2017 15:07:38
JOAN FONT SERRA UNIVERSIDAD DE LA LAGUNA	30/06/2017 15:10:02
ERNESTO PEREDA DE PABLO UNIVERSIDAD DE LA LAGUNA	06/07/2017 13:51:28

because these cannot produce the observed distribution, for an outflow aligned with the line of sight we should always detect both the approaching and receding peak, and an outflow perpendicular to the line of sight would not produce expanding components at all. The change in orientation also changes the velocity of the outflow per projection effects, we show the physical properties depending on inclination in Table 6.2. Based on the fact that we do detect both the receding and approaching components in an area in the centre, we believe that the true orientation should be fairly well aligned with the line of sight, so the properties for an inclination of 60° are more plausible than the others.

Holincheck et al. (2016) obtained dynamical models for a sample of interacting galaxies, which includes Arp 70. In their best fitting model the time since the last approach between the pair of galaxies is 272 Myr, if we assume that the interaction induced the nuclear activity and that it started at this moment we can calculate the kinetic energy output of the AGN, which depending on the inclination of the outflow would vary between $1.9 \cdot 10^{41}$ erg s $^{-1}$ and $4.3 \cdot 10^{41}$ erg s $^{-1}$.

6.3.3 Superbubble associated with the HII region

The AGN described above is already enough to make this galaxy an object of interest regarding galactic evolution and feedback in extreme conditions, but it is not the only interesting case of an expanding structure that the galaxy offers.

In one of the arms of Arp70b, close to the centre of the galaxy itself, there is a giant HII region which dominates the emission in the H α line in the galaxy. In Figure 6.9 we show H α band images for this galaxy, with and without continuum subtraction, where this fact can be appreciated. The HII region has a luminosity of $(7.5 \pm 0.5) \cdot 10^{40}$ erg/s in H α , using the calibration from Kennicutt (1998):

$$\text{SFR}(M_\odot \text{yr}^{-1}) = 7.9 \cdot 10^{-42} L_{\text{H}\alpha} (\text{erg s}^{-1}) \quad (6.3)$$

we obtain a star formation rate of $0.59 \pm 0.04 M_\odot \text{ yr}^{-1}$.

It is in this region that BUBBLY detects the largest superbubble presented in this thesis, spanning about 5 kpc in diameter. In Figure 6.10 we show the expansion map and a profile corresponding to the superbubble.

We apply the usual method for calculating the physical properties described in Chapter 2, here's a brief reminder: The basic expression was already described in the previous subsection, equation 6.1. The difference is that the

Este documento incorpora firma electrónica, y es copia auténtica de un documento electrónico archivado por la ULL según la Ley 39/2015.
Su autenticidad puede ser contrastada en la siguiente dirección <https://sede.ull.es/validacion/>

Identificador del documento: 973636 Código de verificación: QpwS3TwF

Firmado por: ARTEMI CAMPS FARIÑA UNIVERSIDAD DE LA LAGUNA	Fecha: 30/06/2017 14:40:15
JOHN E. BECKMAN UNIVERSIDAD DE LA LAGUNA	30/06/2017 15:07:38
JOAN FONT SERRA UNIVERSIDAD DE LA LAGUNA	30/06/2017 15:10:02
ERNESTO PEREDA DE PABLO UNIVERSIDAD DE LA LAGUNA	06/07/2017 13:51:28

Table 6.2: Physical properties of the outflow depending on inclination with respect to the observer.

	30°		45°		60°	
	approaching	receding	approaching	receding	approaching	receding
v_{exp} (km/s)	977	1014	691	717	564	585
E_K (10^{56} erg)	32.3	4.5	17.9	2.5	14.2	2.0
L_{H_α} (10^{39} erg/s)	11.6	5.7	11.6	5.7	11.6	5.7
Mass ($10^6 M_\odot$)	340	44	377	48	448	57
n_e (cm $^{-3}$)	0.11	0.10	0.10	0.09	0.08	0.08

Notes. The table shows the physical properties for the approaching and receding cones of the outflow depending on their orientation with respect to the observer, which is the only quantity we cannot estimate from the data. The orientations are measured with so that an inclination of 90° would be parallel to the line of sight.

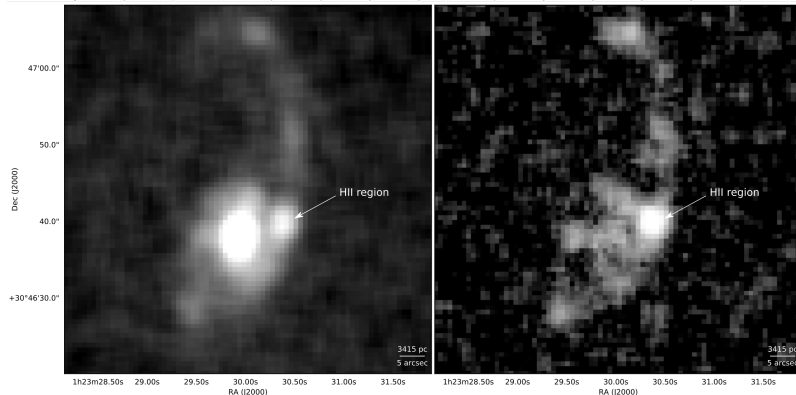


Figure 6.9: H α images of Arp 70b, on the left the zero moment of the CIGALE cube, obtained by summing over all the channels. On the right the continuum subtracted version of this image, where the emission comes only from the H α line itself. This image shows an extremely bright HII region next to the centre in one of the arms.

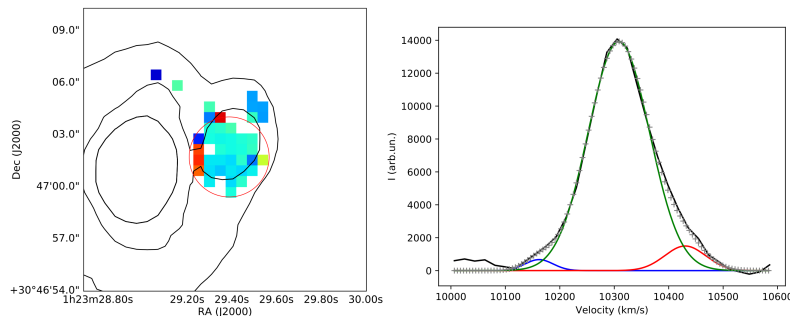


Figure 6.10: On the left we show the expansion map where we detect the superbubble, with a red circle indicating the estimated size of the bubble and black contours showing the H α band flux. The contours correspond to the image without continuum subtraction so that both the region and the centre of the galaxy can be distinguished. On the right we show a line profile of a pixel with detected expansion in the centre of the bubble, with the detected components in green (main peak), red and blue. In grey crosses we plot the resulting fitted profile.

Este documento incorpora firma electrónica, y es copia auténtica de un documento electrónico archivado por la ULL según la Ley 39/2015.
Su autenticidad puede ser contrastada en la siguiente dirección <https://sede.ull.es/validacion/>

Identificador del documento: 973636

Código de verificación: QpwS3TwF

Firmado por: ARTEMI CAMPS FARIÑA
UNIVERSIDAD DE LA LAGUNA

Fecha: 30/06/2017 14:40:15

JOHN E. BECKMAN
UNIVERSIDAD DE LA LAGUNA

30/06/2017 15:07:38

JOAN FONT SERRA
UNIVERSIDAD DE LA LAGUNA

30/06/2017 15:10:02

ERNESTO PEREDA DE PABLO
UNIVERSIDAD DE LA LAGUNA

06/07/2017 13:51:28

volume we use is that of a spherical shell:

$$V = 4\pi R^2 \Delta R \quad (6.4)$$

where R is the bubble radius and ΔR is the shell width. This last quantity cannot be observed with the data at our disposal, so we take the same canonical value of 15% we used in Chapter 5. Using the measured shell luminosity and radius we then obtain the electron density of the gas in the shell, which we use to calculate its mass, having already determined the shell's volume. The last observable is the expanding velocity of the bubble, which we use to calculate its kinetic energy. Finally, we estimate the age of the bubble from the radius and expansion velocity as $t = R/v$. This expression is merely an estimate of the value for the age, normally a lower limit. The evolution of such a large bubble is difficult to parametrize: in the initial stages, when the ambient density could be considered homogeneous, the bubble would decelerate as it swept the surrounding gas into the shell. In this regime the actual age can be calculated as $t = 0.6R/v$. As the bubble becomes larger, however, the decrease in density in the direction perpendicular to the disc comes into effect, and with a sustained power source the shell can actually accelerate. The bubble presented here has a radius of 2.5 kpc and should have a much larger extent in the direction perpendicular to the disc. Because of this we cannot assume a simple evolution model that would allow us to obtain a value for the age from the current radius and expansion velocity.

In Table 6.3 we present the physical properties for the superbubble we detected in Arp70b. As one would expect from such an extreme example of superbubble, the mass and kinetic energy are very large, with tens of millions of solar masses of swept-up gas and a current kinetic energy equivalent to thousands of supernovae explosions.

Table 6.3: Physical properties of the superbubble associated with the giant HII region

Radius	(pc)	2395 ± 239
v_{exp}	(km/s)	130 ± 13
E_K	(10^{51} erg)	6744 ± 1907
$L_{H\alpha}$	(10^{39} erg/s)	3.2 ± 0.2
Mass	($10^6 M_\odot$)	40 ± 8
n_e	(cm^{-3})	0.063 ± 0.007
Age	(Myr)	18 ± 2

Notes. Table showing the physical properties of the superbubble associated with the giant HII region located in the arm of the galaxy.

To our knowledge, this is the largest detected shell produced by an HII

Este documento incorpora firma electrónica, y es copia auténtica de un documento electrónico archivado por la ULL según la Ley 39/2015.
Su autenticidad puede ser contrastada en la siguiente dirección <https://sede.ull.es/validacion/>

Identificador del documento: 973636 Código de verificación: QpwS3TwF

Firmado por: ARTEMI CAMPS FARIÑA UNIVERSIDAD DE LA LAGUNA	Fecha: 30/06/2017 14:40:15
JOHN E. BECKMAN UNIVERSIDAD DE LA LAGUNA	30/06/2017 15:07:38
JOAN FONT SERRA UNIVERSIDAD DE LA LAGUNA	30/06/2017 15:10:02
ERNESTO PEREDA DE PABLO UNIVERSIDAD DE LA LAGUNA	06/07/2017 13:51:28

region. Considering its size, it should have several super star clusters (SSC) powering it and be the result of each SSC producing an expanding bubble, which then merged with those generated by the surrounding clusters to produce the global superbubble we observe.

The coincidence of these two large-scale outflows in such close proximity makes us wonder whether they are connected, the HII region and the centre are separated by about 6 kpc while the radius of the HII shell itself spans 2.5 kpc, about half of this distance. It is reasonable to assume that the AGN is capable of affecting a larger radius than the HII region so a connection between the two phenomena is definitely possible. In this case we would have an example of an AGN enhancing star formation in the surrounding area of the galaxy. Even though this is a plausible explanation for the presence of the giant HII region, we need to remember that correlation does not necessarily imply causality and that both phenomena could be caused simultaneously by the interaction with Arp 70a. If the AGN was responsible for enhancing star formation in the galaxy we would also need to explain why it manifests only on one side of the galaxy, instead of as a ring of induced star formation.

6.4 Summary and conclusions

- Arp 70b is an interacting galaxy where we have found two large-scale outflows currently taking place, one of them in the centre of the galaxy and the other associated with a giant HII region in the arm, close to the centre itself.
- We used the observed properties in a Fabry-Pérot cube and an SDSS spectrum to determine that the central outflow corresponds to an AGN, which is probably a LINER.
- We estimated the shape and extent of the outflow from the FP data, which allowed us to determine the physical parameters of the outflow. We obtain energies of order 10^{57} erg, and masses of around $4 \cdot 10^8 M_{\odot}$, with possible velocities ranging from $\sim 550 \text{ km s}^{-1}$ to $\sim 1000 \text{ km s}^{-1}$.
- There is a giant HII region in the arm where we detect a giant superbubble spanning about 5 kpc in diameter expanding at 130 km s^{-1} , the largest we have detected yet.
- Using BUBBLY we determined the physical parameters of the expanding superbubble, finding an energy of order 10^{54} erg and a mass of about $4 \cdot 10^7 M_{\odot}$.

Este documento incorpora firma electrónica, y es copia auténtica de un documento electrónico archivado por la ULL según la Ley 39/2015.
Su autenticidad puede ser contrastada en la siguiente dirección <https://sede.ull.es/validacion/>

Identificador del documento: 973636

Código de verificación: QpwS3TwF

Fecha: 30/06/2017 14:40:15

Firmado por: ARTEMI CAMPS FARIÑA
 UNIVERSIDAD DE LA LAGUNA

JOHN E. BECKMAN
 UNIVERSIDAD DE LA LAGUNA

JOAN FONT SERRA
 UNIVERSIDAD DE LA LAGUNA

ERNESTO PEREDA DE PABLO
 UNIVERSIDAD DE LA LAGUNA

30/06/2017 15:07:38

30/06/2017 15:10:02

06/07/2017 13:51:28

- It is likely that the presence of both of these outflows is connected in some way, either directly with the AGN enhancing star formation in the nearby HII region or indirectly with both being induced by the interaction with Arp 70a.

Este documento incorpora firma electrónica, y es copia auténtica de un documento electrónico archivado por la ULL según la Ley 39/2015.
Su autenticidad puede ser contrastada en la siguiente dirección <https://sede.ull.es/validacion/>

Identificador del documento: 973636 Código de verificación: QpwS3TwF

Firmado por: ARTEMI CAMPS FARIÑA UNIVERSIDAD DE LA LAGUNA	Fecha: 30/06/2017 14:40:15
JOHN E. BECKMAN UNIVERSIDAD DE LA LAGUNA	30/06/2017 15:07:38
JOAN FONT SERRA UNIVERSIDAD DE LA LAGUNA	30/06/2017 15:10:02
ERNESTO PEREDA DE PABLO UNIVERSIDAD DE LA LAGUNA	06/07/2017 13:51:28

Este documento incorpora firma electrónica, y es copia auténtica de un documento electrónico archivado por la ULL según la Ley 39/2015.
Su autenticidad puede ser contrastada en la siguiente dirección <https://sede.ull.es/validacion/>

Identificador del documento: 973636

Código de verificación: QpwS3TwF

Firmado por: ARTEMI CAMPS FARIÑA
UNIVERSIDAD DE LA LAGUNA

Fecha: 30/06/2017 14:40:15

JOHN E. BECKMAN
UNIVERSIDAD DE LA LAGUNA

30/06/2017 15:07:38

JOAN FONT SERRA
UNIVERSIDAD DE LA LAGUNA

30/06/2017 15:10:02

ERNESTO PEREDA DE PABLO
UNIVERSIDAD DE LA LAGUNA

06/07/2017 13:51:28

7

Conclusions

During the course of this thesis we sought to obtain a method powerful enough to separate the emission of expanding bubbles from the rest of the galaxy and reliable enough to be run easily on datasets without human supervision. We also wanted to use this method to analyse the effects of feedback in nearby galaxies. Here we present the main accomplishments and results obtained:

- An algorithm capable of detecting the presence of multiple peaks in an emission line profile was developed. This algorithm is based on the mathematical properties that the second derivative of a sum of Gaussians exhibits, namely the fact that the centre of each peak is located between two zeros of the second derivative of the profile. We are also able to obtain a good estimation of the fit parameters from the information that these zeros provide.
- The robustness of the fit obtained using the algorithm to detect and estimate the parameters of the peaks allowed us to completely automate the process, which we implemented to develop BUBBLY, a program which analyses data cubes containing Integral Field Unit (IFU) containing spectroscopy of a single emission line. BUBBLY finds and fits the components of the emission profile at each pixel and then matches these to find the presence of expansion, defined by two secondary peaks appearing at each side of the dominant peak, at similar velocity offsets.
- BUBBLY shows the information on expanding components by producing 'expansion maps', obtained by assigning to each pixel in the map the mean separation between the secondary peaks and the main one, for every pixel

where expansion is detected. These maps allow us to find bubbles, which appear as groups of pixels with spatially coherent expansion velocity values. We can measure the size, expansion velocity and flux of the bubbles with this method, from which we can estimate their density, mass, kinetic energy and age.

- After the first implementation of BUBBLY we found a flaw in the reduction pipeline that was commonly used in our data, consisting of an overestimation in the value of the continuum that was estimated by the pipeline. The overestimation was more important on brighter regions, impeding the detection of secondary components in the centre of bright HII regions. This flaw was countered to some extent by an erroneous calculation of the uncertainty in the data, which did not take into account Poisson statistics in the emission.
- Upon correcting the continuum estimation we found that the erroneous uncertainty calculation prevented BUBBLY from producing correct expansion maps. We attempted a number of methods to estimate the noise in the data but found no satisfactory option which worked in both the high and low-brightness regimes.
- In order to obtain the actual relation between intensity and noise we produced a mock galaxy and simulated the observing process with GH α FaS, our instrument. We then processed the simulated observations with our usual reduction procedures and compared the results with the mock galaxy, allowing us to directly measuring the uncertainty. We obtained noise behaviour for three cases: A minimally reduced cube, the result of the reduction pipeline and a simple Gaussian smoothing. We established that the case for Gaussian smoothing exhibited better statistics, which is the method used subsequently.
- The intensity-noise relation we calculated from the simulated observations allowed us to obtain correct expansion maps, solving the uncertainty problem. For the case of Gaussian smoothing we used approximations to derive a theoretical value depending on the smoothing kernel, which yielded an expansion map equivalent to that of the simulated relation.
- We observed a field on the southern arm of M33, finding one region which showed the simultaneous detection of three pairs of expanding components. We mapped the components and found that they appeared to be concentric and of a size comparable to the HII region itself, so we assumed

Este documento incorpora firma electrónica, y es copia auténtica de un documento electrónico archivado por la ULL según la Ley 39/2015.
Su autenticidad puede ser contrastada en la siguiente dirección <https://sede.ull.es/validacion/>

Identificador del documento: 973636

Código de verificación: QpwS3TwF

Fecha: 30/06/2017 14:40:15

Firmado por: ARTEMI CAMPS FARIÑA
 UNIVERSIDAD DE LA LAGUNA

JOHN E. BECKMAN
 UNIVERSIDAD DE LA LAGUNA

JOAN FONT SERRA
 UNIVERSIDAD DE LA LAGUNA

ERNESTO PEREDA DE PABLO
 UNIVERSIDAD DE LA LAGUNA

30/06/2017 15:07:38

30/06/2017 15:10:02

06/07/2017 13:51:28

them to be nested, originating in successive violent episodes within the parent star cluster.

- We obtained long-slit observations which allowed us to compute line ratios between the emission lines H α , [NII] and [SII] for the shells, finding that all three correspond to supernova remnants. Upon calculating the physical properties we found that the shells had amounts of mass that were too high for at least two of the remnants, as we would expect the first to sweep almost all the ambient gas and leave the others to expand in a rarefied medium. We obtained this result even when imposing extreme conditions on the shells that resulted in lower limits to their masses.
- The kinetic energy was also found to be about 1% of its initial value, suggesting that they had been in the radiative phase of their evolution for some time already. The low energies and expansion velocities were not consistent with the size and age of the remnants according to the evolution models for these objects.
- We showed that these inconsistencies could be solved by assuming that cold clouds had survived inside the HII region. These clouds' evaporation could provide the mass-loading observed in the remnants, and the interaction of these with cold clouds is capable of advancing their evolution into the radiative state, accounting for the premature energy loss. We supported this claim on existing literature with observational evidence for the presence of a giant HII cloud associated with the HII region as well as a radio detection of emission consistent with the presence of a recent supernova.
- We used observations with GH α FaS of the interacting pair of galaxies 'The Antennae' to detect 17 superbubbles associated with most of the brightest HII regions in the object and estimated their physical parameters. The bubbles range between \sim 150-500 pc in radius, with low shell densities and kinetic energy between a dozen and a few hundred supernovae. We compared the ages determined from the radius and expansion velocity to values for the underlying clusters obtained from the literature and found the to be reasonable matches.
- The expansion map showed not only the superbubbles but also extended detections which covered most of the galaxy but did not show enough spatial coherence to be identified as superbubbles. Nevertheless, given that their expansion velocities are generally on the low side they should not originate from noise, but rather from spatially unresolved clusters.

Este documento incorpora firma electrónica, y es copia auténtica de un documento electrónico archivado por la ULL según la Ley 39/2015.
Su autenticidad puede ser contrastada en la siguiente dirección <https://sede.ull.es/validacion/>

Identificador del documento: 973636

Código de verificación: QpwS3TwF

Fecha: 30/06/2017 14:40:15

Firmado por: ARTEMI CAMPS FARIÑA
 UNIVERSIDAD DE LA LAGUNA

JOHN E. BECKMAN
 UNIVERSIDAD DE LA LAGUNA

JOAN FONT SERRA
 UNIVERSIDAD DE LA LAGUNA

ERNESTO PEREDA DE PABLO
 UNIVERSIDAD DE LA LAGUNA

30/06/2017 15:07:38

30/06/2017 15:10:02

06/07/2017 13:51:28

We made an estimate of the kinetic energy contained in this unresolved expansion with several approximations and found that it is of the same order as the energy in the bubbles, meaning that the largest HII regions do not dominate the kinetic energy budget in this object.

- To assess the validity of our results and check for bias in the determination of the physical properties we used hydrodynamic simulations to reproduce one of the detected bubbles in the Antennae using the physical parameters as inputs. We managed to obtain a simulated bubble with similar observational properties. Projecting the simulation into a mock expansion map as our program would observe it shows a remarkably similar distribution of velocities due to projection effects, showing a slow decrease in observed expansion velocity before cutting off. This arises from the non-spherical shape of the bubble induced by the density profile of the disk.
- We also used the simulation to check for biases in the determination of the physical parameters, which could arise because we only probe the thinner, faster part of the shell which approaches us. We found that for superbubbles of these sizes the kinetic energy is overestimated by a factor 3 while the mass is underestimated by a factor 2.
- We also used long-slit observations of HII regions along the overlap zone to probe the ionization mechanisms in the expanding shells. A diagnostic on the ratio of forbidden lines $[\text{SII}]_{6716,6734}$ and $[\text{NII}]_{6584}$ to $\text{H}\alpha$ showed that photoionization dominates this process, though the forbidden line ratios are higher for the shells rather than the bulk of the HII region, showing that collisional excitation is more important in the shells.
- We used archive observations of Arp 70, an interacting pair of galaxies, taken with a different Fabry-Pérot instrument, where we have found two large-scale outflows currently taking place in one of the galaxies in the pair. One of these is located in the centre of the galaxy and the other associated with a giant HII region in the arm, close to the centre itself.
- The central outflow was determined to be originated by an AGN, which was identified using the properties of the emission lines measured in a fibre spectrum obtained from the SDSS archive. We estimated the shape and extent of the outflow from the FP data, which allowed us to determine the physical parameters of the outflow. We obtained energies of order 10^{57} erg, and masses of around $4 \cdot 10^8 M_\odot$, with possible velocities ranging from $\sim 550 \text{ km s}^{-1}$ to $\sim 1000 \text{ km s}^{-1}$.

Este documento incorpora firma electrónica, y es copia auténtica de un documento electrónico archivado por la ULL según la Ley 39/2015.
Su autenticidad puede ser contrastada en la siguiente dirección <https://sede.ull.es/validacion/>

Identificador del documento: 973636

Código de verificación: QpwS3TwF

Fecha: 30/06/2017 14:40:15

Firmado por: ARTEMI CAMPS FARIÑA
 UNIVERSIDAD DE LA LAGUNA

JOHN E. BECKMAN
 UNIVERSIDAD DE LA LAGUNA

JOAN FONT SERRA
 UNIVERSIDAD DE LA LAGUNA

ERNESTO PEREDA DE PABLO
 UNIVERSIDAD DE LA LAGUNA

30/06/2017 15:07:38

30/06/2017 15:10:02

06/07/2017 13:51:28

- The other outflow was found on a giant HII region in the arm of the galaxy, where we detect a giant superbubble spanning about 5 kpc in diameter expanding at 130 km s^{-1} , the largest we have detected yet. Using BUBBLY we determined the physical parameters of the expanding superbubble, finding an energy of order 10^{54} erg and a mass of about $4 \cdot 10^7 M_{\odot}$.
- It is likely that the presence of both of these outflows is connected in some way, either directly with the AGN enhancing star formation in the nearby HII region or indirectly with both being induced by the interaction with Arp 70a.
- The successful application of this method even on archival data proves that there is still a lot of information contained in IFU observations that can be obtained with a careful and detailed analysis.

7.1 Future work

The research described in this thesis corresponds to the initial stage of this project, where we have focused on developing the method to detect expansion and applying it to a number of objects. One of our main goals is to obtain results that help us to understand how stellar feedback affects the evolution of the galaxy, particularly how it relates to the accretion of gas from the halo and the dissemination of metals. We expect to use BUBBLY on a growing sample of galaxies, which will provide an important body on information for our studies. We are especially interested in obtaining detailed results in M33, whose proximity allows us to probe the feedback in great detail. Another angle we want to pursue is complementing observations with hydrodynamic simulations. A first step will be to obtain a set of simulations for a variety of environments and input energies which allow us to derive more precise relations between our observables and the properties of the cluster. After this we want to study the effects of the feedback on the environment so we can check the predictions of the model against observations.

Este documento incorpora firma electrónica, y es copia auténtica de un documento electrónico archivado por la ULL según la Ley 39/2015.
Su autenticidad puede ser contrastada en la siguiente dirección <https://sede.ull.es/validacion/>

Identificador del documento: 973636 Código de verificación: QpwS3TwF

Firmado por: ARTEMI CAMPS FARIÑA UNIVERSIDAD DE LA LAGUNA	Fecha: 30/06/2017 14:40:15
JOHN E. BECKMAN UNIVERSIDAD DE LA LAGUNA	30/06/2017 15:07:38
JOAN FONT SERRA UNIVERSIDAD DE LA LAGUNA	30/06/2017 15:10:02
ERNESTO PEREDA DE PABLO UNIVERSIDAD DE LA LAGUNA	06/07/2017 13:51:28

Este documento incorpora firma electrónica, y es copia auténtica de un documento electrónico archivado por la ULL según la Ley 39/2015.
Su autenticidad puede ser contrastada en la siguiente dirección <https://sede.ull.es/validacion/>

Identificador del documento: 973636

Código de verificación: QpwS3TwF

Firmado por: ARTEMI CAMPS FARIÑA
UNIVERSIDAD DE LA LAGUNA

Fecha: 30/06/2017 14:40:15

JOHN E. BECKMAN
UNIVERSIDAD DE LA LAGUNA

30/06/2017 15:07:38

JOAN FONT SERRA
UNIVERSIDAD DE LA LAGUNA

30/06/2017 15:10:02

ERNESTO PEREDA DE PABLO
UNIVERSIDAD DE LA LAGUNA

06/07/2017 13:51:28

Bibliography

- Ambrocio-Cruz, P., Le Coarer, E., Rosado, M., et al. 2016, MNRAS, 457, 2048
- Antonucci, R. 1993, ARA&A, 31, 473
- Arsenault, R., & Roy, J.-R. 1986, AJ, 92, 567
- Audouze, J., & Tinsley, B. M. 1976, ARA&A, 14, 43
- Baade, W. 1943, ApJ, 97, 119
- Baldwin, J. A., Phillips, M. M., & Terlevich, R. 1981, PASP, 93, 5
- Bally, J., & Lada, C. J. 1983, ApJ, 265, 824
- Bastian, N., Emsellem, E., Kissler-Patig, M., & Maraston, C. 2006, A&A, 445, 471
- Berger, M. J., & Colella, P. 1989, Journal of Computational Physics, 82, 64
- Bik, A., Puga, E., Waters, L. B. F. M., et al. 2010, ApJ, 713, 883
- Binney, J., Dehnen, W., & Bertelli, G. 2000, MNRAS, 318, 658
- Binney, J., Nipoti, C., & Fraternali, F. 2009, MNRAS, 397, 1804
- Bland, J., & Tully, B. 1988, Nature, 334, 43
- Blasco-Herrera, J. 2012
- Blasco-Herrera, J., Fathi, K., Beckman, J., et al. 2010, MNRAS, 407, 2519
- Blitz, L., & Stark, A. A. 1986, ApJ, 300, L89
- Bok, B. J., & Reilly, E. F. 1947, ApJ, 105, 255

123

Este documento incorpora firma electrónica, y es copia auténtica de un documento electrónico archivado por la ULL según la Ley 39/2015.
Su autenticidad puede ser contrastada en la siguiente dirección <https://sede.ull.es/validacion/>

Identificador del documento: 973636 Código de verificación: QpwS3TwF

Firmado por: ARTEMI CAMPS FARIÑA UNIVERSIDAD DE LA LAGUNA	Fecha: 30/06/2017 14:40:15
JOHN E. BECKMAN UNIVERSIDAD DE LA LAGUNA	30/06/2017 15:07:38
JOAN FONT SERRA UNIVERSIDAD DE LA LAGUNA	30/06/2017 15:10:02
ERNESTO PEREDA DE PABLO UNIVERSIDAD DE LA LAGUNA	06/07/2017 13:51:28

- Boulesteix, J., Courtes, G., Laval, A., Monnet, G., & Petit, H. 1974, A&A, 37, 33
- Brinks, E., & Bajaja, E. 1986, A&A, 169, 14
- Cantó, J., Raga, A. C., & Rodríguez, L. F. 2000, ApJ, 536, 896
- Cappellari, M. 2017, MNRAS, 466, 798
- Cappellari, M., & Emsellem, E. 2004, PASP, 116, 138
- Castor, J., McCray, R., & Weaver, R. 1975, ApJ, 200, L107
- Casuso, E., & Beckman, J. E. 2001, ApJ, 557, 681
- . 2004, A&A, 419, 181
- Chakrabarti, S., & Ray, A. 2011, ApJ, 728, 24
- Chevalier, R. A. 1974, ApJ, 188, 501
- Chevalier, R. A., & Clegg, A. W. 1985, Nature, 317, 44
- Chiappini, C., Matteucci, F., & Romano, D. 2001, ApJ, 554, 1044
- Choudhury, R., Mookerjea, B., & Bhatt, H. C. 2010, ApJ, 717, 1067
- Chu, Y.-H., & Kennicutt, Jr., R. C. 1994, ApJ, 425, 720
- Cox, D. P. 1972, ApJ, 178, 159
- Cox, D. P., & Reynolds, R. J. 1987, ARA&A, 25, 303
- Daigle, O., Carignan, C., Hernandez, O., Chemin, L., & Amram, P. 2006, MNRAS, 368, 1016
- Dale, J. E., Ngoumou, J., Ercolano, B., & Bonnell, I. A. 2014, MNRAS, 442, 694
- Dekel, A., & Silk, J. 1986, ApJ, 303, 39
- Deul, E. R., & den Hartog, R. H. 1990, A&A, 229, 362
- Donner, K. J., & Thomasson, M. 1994, A&A, 290, 785
- Dubinski, J., & Carlberg, R. G. 1991, ApJ, 378, 496
- Dyson, J. E., & de Vries, J. 1972, A&A, 20, 223

Este documento incorpora firma electrónica, y es copia auténtica de un documento electrónico archivado por la ULL según la Ley 39/2015.
Su autenticidad puede ser contrastada en la siguiente dirección <https://sede.ull.es/validacion/>

Identificador del documento:	973636	Código de verificación:	QpwS3TwF
Firmado por:	ARTEMI CAMPS FARÍÑA UNIVERSIDAD DE LA LAGUNA	Fecha:	30/06/2017 14:40:15
	JOHN E. BECKMAN UNIVERSIDAD DE LA LAGUNA		30/06/2017 15:07:38
	JOAN FONT SERRA UNIVERSIDAD DE LA LAGUNA		30/06/2017 15:10:02
	ERNESTO PEREDA DE PABLO UNIVERSIDAD DE LA LAGUNA		06/07/2017 13:51:28

- Elmegreen, B. G., & Lada, C. J. 1977, ApJ, 214, 725
- Fabian, A. C. 2012, ARA&A, 50, 455
- Fall, S. M., & Efstathiou, G. 1980, MNRAS, 193, 189
- Fathi, K., Beckman, J. E., Lundgren, A. A., et al. 2008, ApJ, 675, L17
- Ferrara, A., & Tolstoy, E. 2000, MNRAS, 313, 291
- Franco, J., Shore, S. N., & Tenorio-Tagle, G. 1994, ApJ, 436, 795
- Frernali, F., & Binney, J. J. 2008, MNRAS, 386, 935
- Freyer, T., Hensler, G., & Yorke, H. W. 2006, ApJ, 638, 262
- Fritze-v. Alvensleben, U. 1999, A&A, 342, L25
- Fukugita, M., Hogan, C. J., & Peebles, P. J. E. 1998, ApJ, 503, 518
- Fukugita, M., & Peebles, P. J. E. 2006, ApJ, 639, 590
- Gao, Y., Lo, K. Y., Lee, S.-W., & Lee, T.-H. 2001, ApJ, 548, 172
- Garcia, D. 2010, Computational Statistics & Data Analysis, 54, 1167
- Garcia Lario, P., Manchado, A., Riera, A., Mampaso, A., & Pottasch, S. R. 1991, A&A, 249, 223
- Genova, R., Beckman, J. E., Molaro, P., & Vladilo, G. 1990, ApJ, 355, 150
- Gerola, H., & Seiden, P. E. 1978, ApJ, 223, 129
- Gerritsen, J. P. E., & Icke, V. 1997, A&A, 325, 972
- Giammanco, C., Beckman, J. E., Zurita, A., & Relaño, M. 2004, A&A, 424, 877
- Gilbert, A. M., & Graham, J. R. 2007, ApJ, 668, 168
- Gingold, R. A., & Monaghan, J. J. 1977, MNRAS, 181, 375
- Gnedin, O. Y., & Zhao, H. 2002, MNRAS, 333, 299
- Gordon, S. M., Duric, N., Kirshner, R. P., Goss, W. M., & Viallefond, F. 1999, ApJS, 120, 247

Este documento incorpora firma electrónica, y es copia auténtica de un documento electrónico archivado por la ULL según la Ley 39/2015.
Su autenticidad puede ser contrastada en la siguiente dirección <https://sede.ull.es/validacion/>

Identificador del documento: 973636 Código de verificación: QpwS3TwF

Firmado por: ARTEMI CAMPS FARÍÑA UNIVERSIDAD DE LA LAGUNA	Fecha: 30/06/2017 14:40:15
JOHN E. BECKMAN UNIVERSIDAD DE LA LAGUNA	30/06/2017 15:07:38
JOAN FONT SERRA UNIVERSIDAD DE LA LAGUNA	30/06/2017 15:10:02
ERNESTO PEREDA DE PABLO UNIVERSIDAD DE LA LAGUNA	06/07/2017 13:51:28

- Goshtasby, A., & O'Neill, W. 1994, CVGIP: Graphical Models and Image Processing, 56, 281
- Guntherdt, G. I., Díaz, R. J., & Agüero, M. P. 2016, AJ, 152, 150
- Hanbury Brown, R., & Hazard, C. 1952, Nature, 170, 364
- Heckman, T. M., Armus, L., & Miley, G. K. 1990, ApJS, 74, 833
- Heckman, T. M., Lehnert, M. D., Strickland, D. K., & Armus, L. 2000, ApJS, 129, 493
- Hennebelle, P., & Ifrig, O. 2014, A&A, 570, A81
- Hernandez, O., Fathi, K., Carignan, C., et al. 2008, PASP, 120, 665
- Hester, J. J., Scowen, P. A., Sankrit, R., et al. 1996, AJ, 111, 2349
- Hnatyk, B., Petruk, O., & Telezhyns'Kyi, I. 2007, Kinematics and Physics of Celestial Bodies, 23, 137
- Hodge, P. W., Skelton, B. P., & Ashizawa, J. 2002, Astrophysics and Space Science Library, Vol. 221, An Atlas of Local Group Galaxies
- Holincheck, A. J., Wallin, J. F., Borne, K., et al. 2016, MNRAS, 459, 720
- Holt, S. S., Neff, S. G., & Urry, C. M. 1992, 254
- Hopkins, P. F., & Elvis, M. 2010, MNRAS, 401, 7
- Hopkins, P. F., Quataert, E., & Murray, N. 2011, MNRAS, 417, 950
- Indebetouw, R., Brogan, C., Chen, C.-H. R., et al. 2013, ApJ, 774, 73
- Jorgenson, R. A., Wolfe, A. M., Prochaska, J. X., & Carswell, R. F. 2009, ApJ, 704, 247
- Joung, M. R., Bryan, G. L., & Putman, M. E. 2012, ApJ, 745, 148
- Kalberla, P. M. W., Burton, W. B., Hartmann, D., et al. 2005, A&A, 440, 775
- Kamphuis, J., Sancisi, R., & van der Hulst, T. 1991, A&A, 244, L29
- Katz, N. 1992, ApJ, 391, 502
- Kennel, C. F., & Coroniti, F. V. 1984, ApJ, 283, 694

Este documento incorpora firma electrónica, y es copia auténtica de un documento electrónico archivado por la ULL según la Ley 39/2015.
Su autenticidad puede ser contrastada en la siguiente dirección <https://sede.ull.es/validacion/>

Identificador del documento:	973636	Código de verificación:	QpwS3TwF
Firmado por:	ARTEMI CAMPS FARÍÑA UNIVERSIDAD DE LA LAGUNA		Fecha: 30/06/2017 14:40:15
	JOHN E. BECKMAN UNIVERSIDAD DE LA LAGUNA		30/06/2017 15:07:38
	JOAN FONT SERRA UNIVERSIDAD DE LA LAGUNA		30/06/2017 15:10:02
	ERNESTO PEREDA DE PABLO UNIVERSIDAD DE LA LAGUNA		06/07/2017 13:51:28

- Kennicutt, Jr., R. C. 1983, ApJ, 272, 54
- . 1998, ARA&A, 36, 189
- Kim, C.-G., Kim, W.-T., & Ostriker, E. C. 2011, ApJ, 743, 25
- Kim, S., Dopita, M. A., Staveley-Smith, L., & Bessell, M. S. 1999, AJ, 118, 2797
- Kirby, E. N., Martin, C. L., & Finlator, K. 2011, ApJ, 742, L25
- Klein, R. I., McKee, C. F., & Colella, P. 1994, ApJ, 420, 213
- Klypin, A., Kravtsov, A. V., Valenzuela, O., & Prada, F. 1999, ApJ, 522, 82
- Kormendy, J., & Ho, L. C. 2013, ARA&A, 51, 511
- Lada, C. J. 1985, ARA&A, 23, 267
- Lah, P., Chengalur, J. N., Briggs, F. H., et al. 2007, MNRAS, 376, 1357
- Lampland, C. O. 1921, PASP, 33, 79
- Laurikainen, E., & Salo, H. 2000, A&AS, 141, 103
- . 2001, MNRAS, 324, 685
- Laurikainen, E., Salo, H., & Aparicio, A. 1998, A&AS, 129, 517
- Le Coarer, E., Rosado, M., Georgelin, Y., Viale, A., & Goldes, G. 1993, A&A, 280, 365
- Lehnert, M. D., Heckman, T. M., & Weaver, K. A. 1999, ApJ, 523, 575
- Lin, C. C., & Shu, F. H. 1964, ApJ, 140, 646
- Lozinskaya, T. A. 1992
- Lucy, L. B. 1977, AJ, 82, 1013
- Mac Low, M.-M., & McCray, R. 1988, ApJ, 324, 776
- Mac Low, M.-M., McCray, R., & Norman, M. L. 1989, ApJ, 337, 141
- MacArthur, L. A., Courteau, S., Bell, E., & Holtzman, J. A. 2004, ApJS, 152, 175
- Marasco, A., Fraternali, F., & Binney, J. J. 2012, MNRAS, 419, 1107

Este documento incorpora firma electrónica, y es copia auténtica de un documento electrónico archivado por la ULL según la Ley 39/2015.
Su autenticidad puede ser contrastada en la siguiente dirección <https://sede.ull.es/validacion/>

Identificador del documento: 973636 Código de verificación: QpwS3TwF

Firmado por: ARTEMI CAMPS FARÍÑA UNIVERSIDAD DE LA LAGUNA	Fecha: 30/06/2017 14:40:15
JOHN E. BECKMAN UNIVERSIDAD DE LA LAGUNA	30/06/2017 15:07:38
JOAN FONT SERRA UNIVERSIDAD DE LA LAGUNA	30/06/2017 15:10:02
ERNESTO PEREDA DE PABLO UNIVERSIDAD DE LA LAGUNA	06/07/2017 13:51:28

- Marinacci, F., Binney, J., Fraternali, F., et al. 2010, MNRAS, 404, 1464
- Marinacci, F., Pakmor, R., & Springel, V. 2014, MNRAS, 437, 1750
- Martin, C. L. 1996, ApJ, 465, 680
- Martizzi, D., Faucher-Giguère, C.-A., & Quataert, E. 2015, MNRAS, 450, 504
- Matteucci, F. 2003
- Mayall, N. U. 1939, Leaflet of the Astronomical Society of the Pacific, 3, 145
- McClure-Griffiths, N. M., Dickey, J. M., Gaensler, B. M., & Green, A. J. 2002, ApJ, 578, 176
- McCray, R., & Kafatos, M. 1987, ApJ, 317, 190
- McKee, C. F., & Ostriker, J. P. 1977, ApJ, 218, 148
- Meaburn, J. 1980, MNRAS, 192, 365
- . 1984, MNRAS, 211, 521
- Mengel, J. G., Demarque, P., Sweigart, A. V., & Gross, P. G. 1979, ApJS, 40, 733
- Mengel, S., Lehnert, M. D., Thatte, N., & Genzel, R. 2002, A&A, 383, 137
- . 2005, A&A, 443, 41
- Mihos, J. C., & Hernquist, L. 1994, ApJ, 437, 611
- Miura, R. E., Kohno, K., Tosaki, T., et al. 2012, ApJ, 761, 37
- Moore, B., Ghigna, S., Governato, F., et al. 1999, ApJ, 524, L19
- Mueller, M. W., & Arnett, W. D. 1976, ApJ, 210, 670
- Navarro, J. F., & Benz, W. 1991, ApJ, 380, 320
- Navarro, J. F., Eke, V. R., & Frenk, C. S. 1996a, MNRAS, 283, L72
- Navarro, J. F., Frenk, C. S., & White, S. D. M. 1996b, ApJ, 462, 563
- Navarro, J. F., & White, S. D. M. 1993, MNRAS, 265, 271
- Nikola, T., Genzel, R., Herrmann, F., et al. 1998, ApJ, 504, 749

Este documento incorpora firma electrónica, y es copia auténtica de un documento electrónico archivado por la ULL según la Ley 39/2015.
Su autenticidad puede ser contrastada en la siguiente dirección <https://sede.ull.es/validacion/>

Identificador del documento:	973636	Código de verificación:	QpwS3TwF
Firmado por:	ARTEMI CAMPS FARÍÑA UNIVERSIDAD DE LA LAGUNA	Fecha:	30/06/2017 14:40:15
	JOHN E. BECKMAN UNIVERSIDAD DE LA LAGUNA		30/06/2017 15:07:38
	JOAN FONT SERRA UNIVERSIDAD DE LA LAGUNA		30/06/2017 15:10:02
	ERNESTO PEREDA DE PABLO UNIVERSIDAD DE LA LAGUNA		06/07/2017 13:51:28

- Norman, M. L., & Winkler, K.-H. A. 1986, 188, 187
- Oey, M. S. 1996, ApJ, 467, 666
- Osterbrock, D., & Flather, E. 1959, ApJ, 129, 26
- Osterbrock, D. E. 1989
- Pagel, B. E. J., & Patchett, B. E. 1975, MNRAS, 172, 13
- Palous, J., Tenorio-Tagle, G., & Franco, J. 1994, MNRAS, 270, doi:10.1093/mnras/270.1.75
- Persic, M., & Salucci, P. 1992, MNRAS, 258, 14P
- Pittard, J. M. 2007, Astrophysics and Space Science Proceedings, 1, 245
- Pontzen, A., & Governato, F. 2012, MNRAS, 421, 3464
- Puche, D., Westpfahl, D., Brinks, E., & Roy, J.-R. 1992, AJ, 103, 1841
- Raga, A. C., de Gouveia Dal Pino, E. M., Noriega-Crespo, A., Mininni, P. D., & Velázquez, P. F. 2002, A&A, 392, 267
- Raga, A. C., Navarro-González, R., & Villagrán-Muniz, M. 2000, Revista Mexicana de Astronomía y Astrofísica, 36, 67
- Rampazzo, R., Plana, H., Amram, P., et al. 2005, MNRAS, 356, 1177
- Relaño, M., & Beckman, J. E. 2005, A&A, 430, 911
- Reyes-Iturbide, J., Rosado, M., Rodríguez-González, A., et al. 2014, AJ, 148, 102
- Rodríguez-González, A., Esquivel, A., Velázquez, P. F., Raga, A. C., & Melo, V. 2008, ApJ, 689, 153
- Rodríguez-Martínez, M., Velázquez, P. F., Binette, L., & Raga, A. C. 2006, A&A, 448, 15
- Rogers, H., & Pittard, J. M. 2013, MNRAS, 431, 1337
- Rosado, M. 1986, A&A, 160, 211
- Sabaddin, F., Minello, S., & Bianchini, A. 1977, A&A, 60, 147
- Salo, H., & Laurikainen, E. 1993, ApJ, 410, 586

Este documento incorpora firma electrónica, y es copia auténtica de un documento electrónico archivado por la ULL según la Ley 39/2015.
Su autenticidad puede ser contrastada en la siguiente dirección <https://sede.ull.es/validacion/>

Identificador del documento: 973636 Código de verificación: QpwS3TwF

Firmado por: ARTEMI CAMPS FARÍÑA UNIVERSIDAD DE LA LAGUNA	Fecha: 30/06/2017 14:40:15
JOHN E. BECKMAN UNIVERSIDAD DE LA LAGUNA	30/06/2017 15:07:38
JOAN FONT SERRA UNIVERSIDAD DE LA LAGUNA	30/06/2017 15:10:02
ERNESTO PEREDA DE PABLO UNIVERSIDAD DE LA LAGUNA	06/07/2017 13:51:28

- Sancisi, R., Fraternali, F., Oosterloo, T., & van der Hulst, T. 2008, A&A Rev., 15, 189
- Schmidt, M. 1963, ApJ, 137, 758
- Searle, L., & Sargent, W. L. W. 1972, ApJ, 173, 25
- Sedov, L. I. 1959
- Silk, J. 2005, MNRAS, 364, 1337
- Snider, K. D., Hester, J. J., Desch, S. J., Healy, K. R., & Bally, J. 2009, ApJ, 700, 506
- Spitoni, E., Matteucci, F., Recchi, S., Cescutti, G., & Pipino, A. 2009, A&A, 504, 87
- Springel, V., & Hernquist, L. 2003, MNRAS, 339, 289
- Staveley-Smith, L., Sault, R. J., Hatzidimitriou, D., Kesteven, M. J., & McConnell, D. 1997, MNRAS, 289, 225
- Stevens, I. R., & Hartwell, J. M. 2003, MNRAS, 339, 280
- Storrie-Lombardi, L. J., McMahon, R. G., & Irwin, M. J. 1996, MNRAS, 283, L79
- Strickland, D. K., Heckman, T. M., Weaver, K. A., Hoopes, C. G., & Dahlem, M. 2002, ApJ, 568, 689
- Stutzki, J., & Guesten, R. 1990, ApJ, 356, 513
- Talbot, Jr., R. J., & Arnett, W. D. 1971, ApJ, 170, 409
- Tasker, E. J., Brunino, R., Mitchell, N. L., et al. 2008, MNRAS, 390, 1267
- Taylor, G. 1950, Proceedings of the Royal Society of London Series A, 201, 159
- Tenorio-Tagle, G., Muñoz-Tuñón, C., Pérez, E., Silich, S., & Telles, E. 2006, ApJ, 643, 186
- Teyssier, R. 2015, ARA&A, 53, 325
- Thacker, R. J., & Couchman, H. M. P. 2000, ApJ, 545, 728
- Thornton, K., Gaudlitz, M., Janka, H.-T., & Steinmetz, M. 1998, ApJ, 500, 95

Este documento incorpora firma electrónica, y es copia auténtica de un documento electrónico archivado por la ULL según la Ley 39/2015.
Su autenticidad puede ser contrastada en la siguiente dirección <https://sede.ull.es/validacion/>

Identificador del documento:	973636	Código de verificación:	QpwS3TwF
Firmado por:	ARTEMI CAMPS FARÍÑA UNIVERSIDAD DE LA LAGUNA	Fecha:	30/06/2017 14:40:15
	JOHN E. BECKMAN UNIVERSIDAD DE LA LAGUNA		30/06/2017 15:07:38
	JOAN FONT SERRA UNIVERSIDAD DE LA LAGUNA		30/06/2017 15:10:02
	ERNESTO PEREDA DE PABLO UNIVERSIDAD DE LA LAGUNA		06/07/2017 13:51:28

- Tinsley, B. M. 1974, ApJ, 192, 629
- . 1981, ApJ, 250, 758
- Torres-Papaqui, J. P., Coziol, R., Ortega-Minakata, R. A., & Neri-Larios, D. M. 2012, ApJ, 754, 144
- Tremonti, C. A., Moustakas, J., & Diamond-Stanic, A. M. 2007, ApJ, 663, L77
- Tremonti, C. A., Heckman, T. M., Kauffmann, G., et al. 2004, ApJ, 613, 898
- Twarog, B. A. 1980, ApJ, 242, 242
- Urry, C. M., & Padovani, P. 1995, PASP, 107, 803
- Valdes, F., Gupta, R., Rose, J. A., Singh, H. P., & Bell, D. J. 2004, ApJS, 152, 251
- Valdez-Gutiérrez, M., Rosado, M., Georgiev, L., Borissova, J., & Kurtev, R. 2001, A&A, 366, 35
- Veilleux, S., Cecil, G., Bland-Hawthorn, J., et al. 1994, ApJ, 433, 48
- Weaver, R., McCray, R., Castor, J., Shapiro, P., & Moore, R. 1977, ApJ, 218, 377
- White, S. D. M., & Rees, M. J. 1978, MNRAS, 183, 341
- Whitmore, B. C., & Zhang, Q. 2002, AJ, 124, 1418
- Whitmore, B. C., Zhang, Q., Leitherer, C., et al. 1999, AJ, 118, 1551
- Whitmore, B. C., Gilmore, D., Leitherer, C., et al. 2005, AJ, 130, 2104
- Whitmore, B. C., Chandar, R., Schweizer, F., et al. 2010, AJ, 140, 75
- Wiersma, R. P. C., Schaye, J., Dalla Vecchia, C., et al. 2010, MNRAS, 409, 132
- Wilcots, E. M., & Miller, B. W. 1998, AJ, 116, 2363
- Wilson, C. D., Scoville, N., Madden, S. C., & Charmandaris, V. 2000, ApJ, 542, 120
- . 2003, ApJ, 599, 1049
- Yang, H., Chu, Y.-H., Skillman, E. D., & Terlevich, R. 1996, AJ, 112, 146

Este documento incorpora firma electrónica, y es copia auténtica de un documento electrónico archivado por la ULL según la Ley 39/2015.
Su autenticidad puede ser contrastada en la siguiente dirección <https://sede.ull.es/validacion/>

Identificador del documento: 973636 Código de verificación: QpwS3TwF

Firmado por: ARTEMI CAMPS FARÍÑA UNIVERSIDAD DE LA LAGUNA	Fecha: 30/06/2017 14:40:15
JOHN E. BECKMAN UNIVERSIDAD DE LA LAGUNA	30/06/2017 15:07:38
JOAN FONT SERRA UNIVERSIDAD DE LA LAGUNA	30/06/2017 15:10:02
ERNESTO PEREDA DE PABLO UNIVERSIDAD DE LA LAGUNA	06/07/2017 13:51:28

- Yepes, G., Kates, R., Khokhlov, A., & Klypin, A. 1997, MNRAS, 284, 235
- Yin, J., Matteucci, F., & Vladilo, G. 2011, A&A, 531, A136
- Zaninetti, L. 2004, PASJ, 56, 1067
- Zanstra, H. 1955, Vistas in Astronomy, 1, 256
- Zaragoza-Cardiel, J., Font, J., Beckman, J. E., et al. 2014, MNRAS, 445, 1412
- Zaragoza-Cardiel, J., Beckman, J. E., Font, J., et al. 2015, MNRAS, 451, 1307
- Zhang, Q., & Fall, S. M. 1999, ApJ, 527, L81
- Zhu, M., Seaquist, E. R., & Kuno, N. 2003, ApJ, 588, 243
- Zubovas, K., & Bourne, M. A. 2017, MNRAS, 468, 4956
- Zubovas, K., & King, A. 2012, ApJ, 745, L34
- Zwaan, M. A., van der Hulst, J. M., Briggs, F. H., Verheijen, M. A. W., & Ryan-Weber, E. V. 2005, MNRAS, 364, 1467

Este documento incorpora firma electrónica, y es copia auténtica de un documento electrónico archivado por la ULL según la Ley 39/2015.
Su autenticidad puede ser contrastada en la siguiente dirección <https://sede.ull.es/validacion/>

Identificador del documento: 973636 Código de verificación: QpwS3TwF

Firmado por: ARTEMI CAMPS FARÍÑA UNIVERSIDAD DE LA LAGUNA	Fecha: 30/06/2017 14:40:15
JOHN E. BECKMAN UNIVERSIDAD DE LA LAGUNA	30/06/2017 15:07:38
JOAN FONT SERRA UNIVERSIDAD DE LA LAGUNA	30/06/2017 15:10:02
ERNESTO PEREDA DE PABLO UNIVERSIDAD DE LA LAGUNA	06/07/2017 13:51:28